Dye-Doped Polymeric Lasers for Sensing Applications

Zur Erlangung des akademischen Grades eines
DOKTORS DER NATURWISSENSCHAFTEN
von der Fakultät für Physik
des Karlsruher Instituts für Technologie (KIT)

genehmigte

DISSERTATION

von

Dipl.-Phys. Sarah Manuela Milena Krämmer, geb. Wiegele
aus Rastatt

Tag der mündlichen Prüfung : 21.10.2016
Referent : Prof. Dr. Heinz Kalt
Korreferent : Priv.-Doz. Dr.-Ing. Timo Mappes

Prüfungskomission:

Prof. Dr. H. Kalt
Priv.-Doz. Dr. T. Mappes
Prof. Dr. W. Wernsdorfer
Prof. Dr. C. Rockstuhl
Prof. Dr. A.-S. Müller

Karlsruhe Institute of Technology (KIT)
Institute of Applied Physics
Wolfgang-Gaede-Straße 1
76131 Karlsruhe
Germany
AG Kalt: http://www.aph.kit.edu/kalt

Sarah Manuela Milena Krämmer
sarah.kraemmer@kit.edu kraemmer.sarah@gmail.com

This work has been supported financially by the Center for Functional Nanostructures, the Carl-Zeiss-Foundation and the Karlsruhe School of Optics and Photonics.

http://www.cfn.kit.edu

http://www.carl-zeiss-stiftung.de

http://www.ksop.de

Contents

1 Introduction **1**

2 Fundamentals of Sensors **5**
2.1 Performance Criteria of Sensors 5
2.2 State of the Art Concepts of Optical Sensors for Molecule Detection . 7
2.3 Summary and Conclusions 14

3 Dye-Doped Polymeric Microlasers **17**
3.1 Polymeric Microresonators 17
3.1.1 Optical Properties of Microcavities 17
3.1.2 Whispering Gallery Mode Resonators 20
3.1.3 Ring Resonators 23
3.2 Laser Dyes as Active Material 25
3.2.1 Electronic Structure of Laser Dyes 25
3.2.2 Properties of Pyrromethene 597 29
3.3 Optical Setups Used for Investigating Dye-Doped Microcavities . . . 30
3.3.1 Micro-Photoluminescence Spectroscopy Setup 31
3.3.2 Fiber Excitation Setup 32
3.4 Summary and Conclusions 32

4 Polymeric Whispering Gallery Mode Lasers as Sensors **35**
4.1 Sensing with Whispering Gallery Mode Cavities 35
4.1.1 Reactive Sensing Principle 36
4.1.2 Implementations of WGM Sensors in Literature 37
4.2 Fabrication of Dye-Doped Polymeric Disc- or Goblet-Shaped Cavities 39
4.3 Fluorol-doped WGM Cavities 40
4.4 All-Polymeric Resonator Sensor Chips 44
4.5 Summary and Conclusions 47

5 Whispering Gallery Mode Lasers with Enhanced Sensitivity **51**
5.1 Detection Limit of WGM Lasers 51

5.2 Resonators with High Refractive Index Coating Layer 59
5.2.1 Finite Element Simulations of WGMs 59
5.2.2 Optimization of the Layer Thickness 60
5.3 Resonators of Varying Size and Geometry 64
5.3.1 Disc Resonators of Varying Radii 65
5.3.2 Disc Resonators of Varying Thicknesses 71
5.3.3 Goblet Resonators of Optimized Size 74
5.3.4 Comparison of the Different Approaches 75
5.4 Summary and Conclusions 78

6 Lasing Emission from Random Resonators in Electrospun Dye-Doped Polymer Fiber Networks 81
6.1 Electrospun Polymer Fiber Networks 81
6.1.1 Principle of Electrospinning 82
6.1.2 Structure and Alignment of Electrospun Fibers 83
6.2 Lasing emission: Observations 84
6.2.1 Typical Photoluminescence Spectra 85
6.2.2 Lasing Thresholds 85
6.3 Lasing Mechanism of Fiber Resonators 87
6.3.1 Spatially Resolved Spectroscopy 89
6.3.2 Geometry of Random Resonators 90
6.3.3 Simulations of the Coupling Region 93
6.4 Summary and Conclusions 94

7 Optical Sensing with Polymer Fiber Networks 97
7.1 Sensing of Different Vapors 98
7.1.1 Mechanism of Vapor Sensing 98
7.1.2 Temperature Dependence and Operational Lifetime of Dye-Doped Polymer Fibers 103
7.1.3 Detection of Water Vapor 106
7.1.4 Detection of Light Alcohol Vapors 108
7.2 Sensing in Aqueous Environment 113
7.2.1 Lasing Performance of the Fiber Networks in Aqueous Environment 115
7.2.2 Bulk Refractive Index Sensing 117
7.3 Summary and Conclusions 119

8 Conclusions and Outlook 121

A Vapor Mixing System 125

B Samples Investigated in This Work **127**

List of Publications **131**

References **137**

Closing Words **159**

Chapter 1

Introduction

Throughout history mankind has experienced dangers which are not subject to human perception before they have severe effects. An early detection of such hazards to prevent negative consequences was the basic motivation for the development of sensor technology.

An early example of a sensor is the canary bird which was taken to coal mines to detect the odorless and colorless carbon monoxide before its concentration reaches values fatal to humans. Another example for an animal sensor still in use nowadays are trained shepherds for the detection of explosives or drugs.

With technological progress the focus was also set on developing artificial sensors for a manifold of applications in, e.g., clinical diagnostics, detection of explosives, and surveillance of air quality. The current challenge is the miniaturization of the sensor systems since this would further pave the way for portable systems which could be used everywhere around the world. One prospect under intensive development are so-called lab-on-a-chip (LoC) systems for which all components necessary for analysis are united on a single chip [1].

In the field of medicine such LoC systems could be used for point-of-care diagnostics allowing to perform, e.g., blood analysis directly at the patient yielding immediate results. When LoC systems are realized at low costs health care especially in developing countries and early diagnostics of diseases could be improved drastically [2,3].

Among the different sensor types optical microsensors are particularly promising since they can be integrated into microchips, fabricated at low costs and furthermore, allow multiplexed detection within a single device [4–6]. Different transduction pathways have been implemented in the field of optical sensing including plasmonic resonances, interferometers, photonic crystals and optical microresonators [7].

In optical microcavities light can be confined to a small volume for comparably long times [8] leading to enhanced interaction of the light with the analyte which is under investigation. This yields extremely high sensitivities – with silica toroids and spheres even the detection of single molecules was demonstrated [9, 10].

However, fabrication of silica cavities requires serial treatment of each resonator with a CO_2 laser making large-scale fabrication challenging. Additionally, for the read-out of the sensor signal a tapered fiber needs to be approached to the resonator. A tapered fiber is a fragile object which degrades within hours and its alignment requires sophisticated equipment to move the fiber with a precision of a few tens of nanometers. Thus, sensing with this kind of cavities outside a laboratory environment is difficult to imagine.

Polymeric cavities are able to overcome these drawbacks since parallel fabrication is feasible and the integration of optically active materials into the polymer host matrix is simple. With this approach microlasers are feasible which can be excited and read-out with free-space optics facilitating operability. In previous work of this research group polymeric goblet-shaped low-threshold microlasers were developed and their basic sensing ability was demonstrated [11].

One objective of this work was the enhancement of the sensitivity of WGM lasers with the intention to keep the fabrication process simple and suitable for large-scale production. Different strategies were pursued: One approach was to use a high-refractive coating layer which was deposited onto the cavities. Another method focussed on the optimization of the dimensions of the cavities. The different samples were characterized regarding their lasing thresholds, quality factors, and sensitivities and finally the different approaches were compared to each other and to previous results.

The second aim was to investigate a different sensing system based on dye-doped electrospun polymer fiber networks. Therefore, first the origin of the lasing emission of these polymer fiber networks was identified by using spatially resolved spectroscopy. Furthermore, the successful implementation of the polymer fiber network lasers as sensors for different vapors was demonstrated. The vapor sensing mechanism, which is based on the swelling of the fibers once opposed to the analyte, was analyzed in detail. It was shown that a differentiation of ethanol and methanol vapor is possible when time-resolved sensing measurements are conducted. Furthermore, the sensing ability of the polymer fiber network lasers in aqueous environment was successfully demonstrated via the detection of bulk refractive index changes.

Structure of this work

This thesis is divided into eight chapters. In chapter 2 an introduction to optical sensor principles is given and central figures of merit are presented. Furthermore, the working principle of different state of the art optical sensors and their advantages and drawbacks are discussed.

Chapter 3 focusses on dye-doped polymeric microlasers as these types of optical sensors were investigated in this work. First, the optical properties of microcavities are discussed in general before the light propagation in WGM cavities and ring resonators is described. Afterwards, the mechanism how laser dyes act as gain medium is explained and the properties of the laser dye Pyrromethene 597, which was mainly used in this work, are presented. At the end of this chapter the micro-photoluminescence setup and the fiber-coupling setup used for the optical characterization of the cavities are presented.

Chapter 4 gives an overview on different implementations of passive cavities in literature and compares them to active WGM resonators with lasing emission. Afterwards, the fabrication process of the polymeric microlasers used in this work is presented. One advantage of polymeric cavities is that various optical gain media can be easily integrated, which will be demonstrated by the integration of the dye Fluorol 7GA, which can be excited with a blue laser diode. Furthermore, a modified fabrication process for all-polymeric resonators was developed and these resonators were successfully integrated into a polymeric chip with an integrated fluidic chamber.

Sensitivity is one important figure of merit of sensors. In this work different concepts for the improvement of the sensitivity were successfully realized and are presented in chapter 5. The first concept is the deposition of a high-refractive index coating layer leading to an enhanced mode overlap with the surrounding and hence an increased sensitivity. The second concept is the variation of the dimensions and geometry of the cavity. Both, the radius and the thickness of the cavity were varied to optimize the sensing performance. A comparison of the different concepts on sensitivity enhancement – also including previous work – ends this chapter and also the part on WGM resonators.

Chapter 6 focusses on the lasing mechanism in randomly oriented dye-doped electrospun polymer fiber networks which represent a promising new type of optical sensor. At the beginning the concept of electrospinning is presented. Afterwards the emission spectra of the fiber networks are analyzed. During this work spatially resolved microscopy was used to identify random fiber loops as the origin of the lasing emission. The results on these measurements as well as the theory of a directional coupler which was used to describe the formation of closed optical paths in

the fiber networks are presented at the end of this chapter.

Electrospun polymer fiber networks are promising candidates for sensing applications due to their high surface to volume ratio and their simple fabrication process. In this work the fiber networks were investigated regarding their sensing abilities. In chapter 7, the results on the detection of different vapors, which is based on the diffusion of the vapors into the fibers, are presented. It will be shown that the analysis of the time-resolved signal even allows to discriminate different alcohol vapors. Furthermore, the successful implementation of the electrospun polymer fiber networks as sensors in aqueous environment was demonstrated by proof-of-principle experiments. The results and a comparison to expectations from simulations are presented in the last part of this chapter.

In the last chapter the main results of this work are summarized and conclusions are drawn. Furthermore, a brief outlook on possible future work is given.

Chapter 2

Fundamentals of Sensors

The purpose of this chapter is to give a brief introduction into sensing where the focus lies on detection of biomolecules (proteins, DNA, viruses, etc.) and gases or vapors. At the beginning the general operation principle of a sensor is explained and different performance criteria of sensors are presented. Since the sensors investigated in this work are based on optical resonators the second part of this chapter will concentrate on optical sensor concepts. Different sensing principles will be introduced and compared with respect to the criteria given in the first part.

2.1 Performance Criteria of Sensors

In general, a sensor can be described as a device which provides a measurable signal as a result of changes in its environment. Although the variety of sensors is tremendous certain figures of merit can be found according to which the sensors can be assessed. Once the general operation principle of sensors has been explained performance criteria are presented focussing on criteria relevant for detection of biomolecules and gases or vapors.

Operation Principle of a Sensor
As mentioned before the task of a sensor is to transfer the reaction of the system to an external stimulus into a measurable signal. Normally a sensor consists of a sensing element reacting to the stimulus and a transducer which converts this reaction into an externally measurable signal, e.g., a mechanical, electrical or optical signal [12]. One can distinguish between binary sensors, simply giving a "yes" or "no" response depending on whether target molecules are present or not and sensors also delivering

quantitative information on the target molecule concentration.

Sensitivity and Detection Limit

The sensitivity connects the output signal of the sensor with the amount of target molecules being present [12]. If the output signal depends linearly on the target molecule concentration the sensitivity is the slope of the calibration curve [13].

Another figure of merit is the detection limit which gives the minimum amount of target substance or change in the environment which can be detected by the sensor [14,15], e.g., a concentration of target molecules, a refractive index change or a temperature change. The detection limit DL is given by the ratio of the resolution R to the sensitivity S [16]:

$$DL = \frac{R}{S}. \tag{2.1}$$

The resolution describes the smallest resolvable signal thus depending on the total noise in the signal σ. Usually the resolution is given as $R = 3\sigma$. Obviously the detection limit can be lowered by either minimizing the noise or by increasing the sensitivity of the sensor.

Selectivity Towards Analytes

Selectivity is defined as the ability of a sensor to distinguish between different species of target molecules. Ideally, a sensor would respond exclusively to one species present in the sample and there would be no interference from other species when present simultaneously [17]. The most popular method to obtain a high selectivity is to use a selective material as reactive sensor element which specifically interacts with the target molecules. In gas sensing this is feasible since different material–target molecule combinations show different adsorption and reaction properties [18]. For sensing of biomolecules different combinations of receptors and target molecules showing selective binding are used [17], e.g., complementary DNA strands or protein–enzyme pairs. Furthermore, changes in the environment such as temperature fluctuations may influence the sensor signal. To eliminate these effects the sensor has to be designed in a way that it is either insensitive to environmental influences or suitable referencing techniques have to be employed [4].

Applicability for On-Chip Systems

Since sensors on the micrometer scale offer multiple advantages such as low analyte consumption, fast response time, simple operation and low costs miniaturization of sensors has become an emerging field of interest [1,2,19].

For the realization of miniaturized sensors it is necessary that the sensor components or at least the sensing element and the transducer element have dimensions in the order of micrometers and that it can be fabricated on-chip. To enable low-cost production scalable fabrication techniques are desirable right from the beginning.

2.2 State of the Art Concepts of Optical Sensors for Molecule Detection

In this section state of the art optical sensor concepts, which have application potential in the detection of biomolecules and gases or vapors, are introduced. A change in intensity, phase, wavelength or polarization of the incident light, which is induced by target molecules, serves as signal. Optical sensors show immunity against electronic disturbances, can be operated at high speed, allow remote sensing and multiplexing and can be fabricated at low costs [4, 6].

Concerning the detection of biomolecules two different techniques are distinguished: label-based and label-free sensing [4]. For label-based sensing the target molecules themselves or molecules specifically binding to them are labeled with fluorescent markers. The fluorescence intensity provides information on the presence of target molecules. Single molecule detection has been demonstrated with this technique [20], however, the labeling procedure is time- and cost-consuming and determination of the target molecule concentration is impeded since control over the number of bound fluorescence label is not given [21]. These inherent disadvantages of label-based sensing easily demonstrate that label-free detection is desirable. This is why this work focuses on optical resonators belonging to the category of label-free sensors.

In the following, an overview on label-free sensor concepts will be given, where two kinds of techniques can be distinguished: On the one hand there are techniques which rely on characteristic transitions of molecules serving as fingerprint such as absorption or Raman spectroscopy. On the other hand there are techniques based on the detection of relative changes in the refractive index, e.g., surface plasmon resonances or optical resonators [4]. The presented sensing mechanisms can be applied for biomolecules and gases or vapors. The list of the following examples of label-free concepts raises no claims to be complete but serves as basic overview since the field of research is too large to give an entire perspective.

Absorption Spectroscopy
In absorption spectroscopy light of a broadband source (UV, visible, IR) is incident on the sample cell containing the analyte (Fig. 2.1 (a)). Depending on the molecular

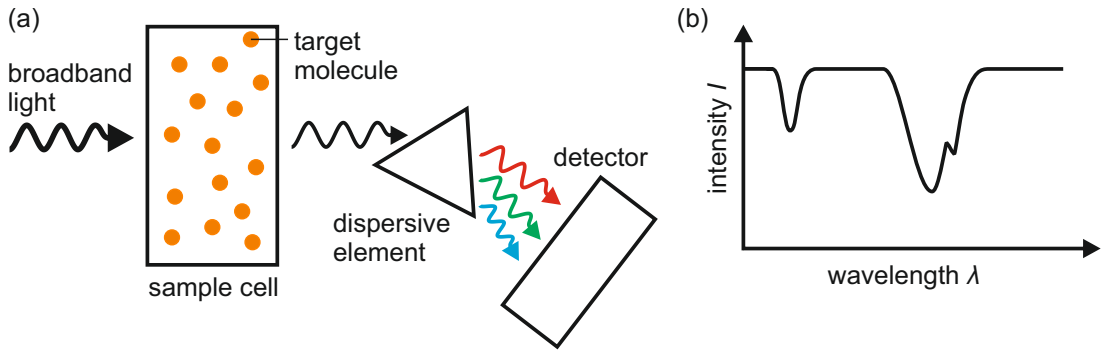

Figure 2.1: Principle of absorption spectroscopy. (a) Schematic of an example absorption spectroscopy setup. Light of a broadband source is guided through a sample cell containing the target molecules. The transmitted light is spectrally resolved and detected. (b) Example of a transmission spectrum. Dips in the transmission spectrum represent absorption of the sample.

structure of the target molecules different wavelengths are absorbed. By measuring the wavelength-dependent attenuation of the transmitted light (Fig. 2.1 (b)) conclusions on the analyte and on the concentration of target molecules can be drawn [22]. The ratio of incident intensity $I_0(\lambda)$ to transmitted intensity $I(\lambda)$ is given by the Beer-Lambert law

$$\frac{I(\lambda)}{I_0(\lambda)} = \mathrm{e}^{-\epsilon(\lambda)\cdot c\cdot L}, \tag{2.2}$$

where $\epsilon(\lambda)$ is the target molecule specific extinction coefficient, c is the concentration of target molecules and L is the length of the cell containing the sample. Due to the exponential dependence of the transmitted intensity on the sample length miniaturization is challenging – especially for detection of low concentrations and target molecules with small extinction coefficient. In cavity enhanced absorption spectroscopy (CEAS) the use of optical cavities allows size reduction while maintaining long interaction lengths [23, 24].

Raman Spectroscopy

The Raman spectrum of a molecule contains information on its vibrational energy levels and thus serves as a fingerprint for molecule identification. A monochromatic light source is used for excitation and the scattered light is analyzed with a spectrometer. Besides the Rayleigh peak resulting from elastically scattered photons a Stokes and an Anti-Stokes peak due to inelastic (Raman) scattering are observed in the spectrum. In quantum theory these scattering processes are described by the excitation to a virtual energy level followed by relaxation to different vibrational

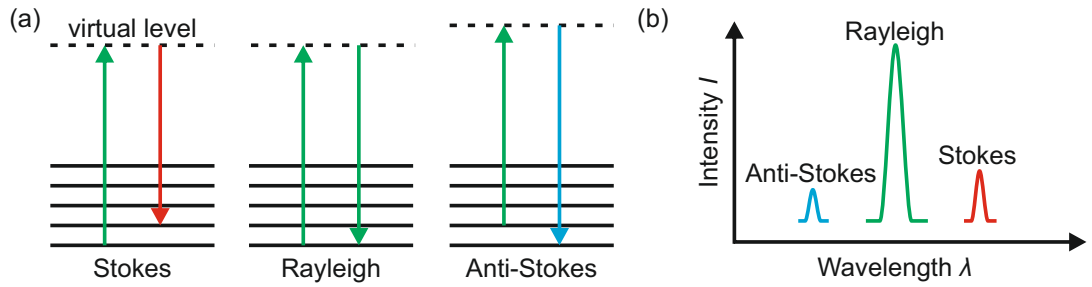

Figure 2.2: Principle of Raman spectroscopy. (a) Illustration of the different scattering processes occurring in Raman spectroscopy. For Rayleigh scattering initial and final vibrational energy states are identical while for Stokes (Anti-Stokes) Raman scattering the final energy state is higher (lower) than the initial one. (b) Visualization of a Raman spectrum which can be used for molecule identification. The height of the peaks is not to scale. Adapted from [25].

states of the molecule along with the emission of a photon. The different processes are illustrated in Fig. 2.2. For Rayleigh scattering initial and final vibrational level are identical. In case of Stokes Raman (Anti-Stokes Raman) scattering the final vibrational level is energetically higher (lower) than the initial one, resulting in a red-shift (blue-shift) of the peak compared to the Rayleigh peak. At room temperature usually most molecules are in the vibrational ground state. Therefore the probability for Stokes Raman is higher than for Anti-Stokes Raman [25].

Drawbacks of Raman spectroscopy are the small spectral distance between the Stokes and Anti-Stokes peaks and the Rayleigh peak and the fact that the intensities of the Stokes and Anti-Stokes peak are several orders of magnitude smaller than the intensity of the Rayleigh peak [26, 27]. Several techniques have been developed to enhance the weak Raman signal, the most prominent one being surface enhanced Raman spectroscopy (SERS). With SERS the signal is amplified by several orders of magnitudes due to field enhancement on rough metallic surfaces or metallic nanoparticles [28–30]. Recently progress towards on-chip SERS has been reported [31].

Surface Plasmon Resonances

A surface plasmon resonance (SPR) is an oscillation of charge density which occurs at an interface between two media with dielectric constants of opposite signs, e.g., a metal and a dielectric [32]. The SPR exhibits an evanescent field in the surrounding medium and is thus sensitive to refractive index changes. There are different tech-

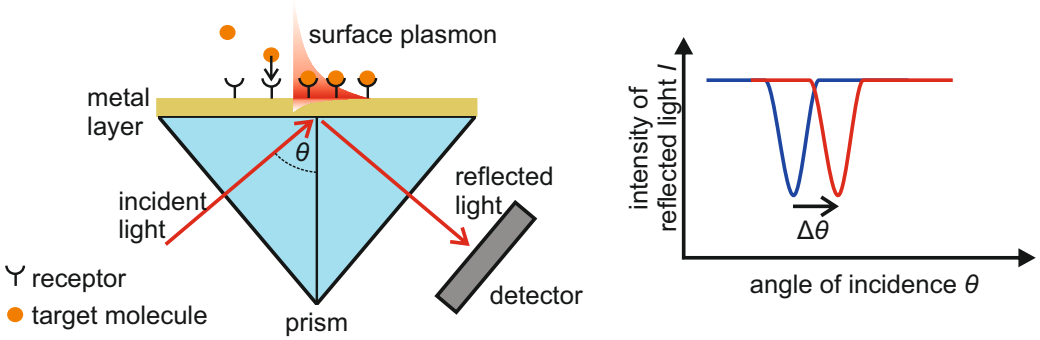

Figure 2.3: Schematic of a surface plasmon sensor. The plasmon resonance is determined by, e.g., scanning the angle of the incident light θ and measuring the reflected intensity. When target molecules attach to the receptor molecules on the metal surface the refractive index of the surrounding changes and thus the plasmon resonance shifts to a different angle. Adapted from [52].

niques to excite SPRs [4,33]. One method is the use of a prism as shown in Fig. 2.3. The incident light experiences total internal reflection at the prism–metal interface and an evanescent wave penetrates in the metal. When its propagation constant $k_{||}$ matches the propagation constant β_{sp} of the plasmon

$$k_{||} = \frac{2\pi}{\lambda} \sin\theta = \beta_{\mathrm{sp}}(n_{\mathrm{sur}}) \tag{2.3}$$

the incident wave can couple to the surface plasmon and the intensity of the reflected light decreases [4,34]. When target molecules attach to the metal surface the refractive index of the surrounding n_{sur} changes and the plasmon resonance shifts [35]. To monitor shifts of the SPR the angle of incidence or the wavelength of the incoming light is scanned [33,36,37] or the intensity change for fixed angle and wavelength is measured [34].

The sensing applications of SPRs have been intensively investigated and developed resulting in the successful detection of bulk refractive index changes [36, 38], proteins [39,40], DNA [41,42], bacteria [43] and gases [35,44–46]. SPRs exhibit a high sensitivity [33] and also detection of single molecules has been demonstrated by the use of single gold nanorods [47, 48]. For laboratory use commercial products for immune-sensing and DNA hybridization are already available [49]. Concerning miniaturization different approaches combining SPR sensor elements with microfluidics on-chip have been presented [50, 51].

Photonic Crystals

Photonic crystals are dielectric structures with a periodic variation of the refractive index in one, two or three dimensions [53]. The periodicity in the order of the wavelength creates a photonic bandgap (also called stop-band). Light of frequencies matching this gap cannot propagate in the photonic crystal analogously to a semiconductor which has no allowed electron states in the band gap. For sensing photonic crystals are used in different modes: Either the spectral position of the entire stop-band is monitored [54] or the photonic crystal is modified as described in the following. A so-called photonic defect is created when a local disturbance of the periodicity of the photonic crystal is introduced. This results in a defect mode which can propagate through the crystal within the bandgap [4]. This defect mode is then observed as a peak in the transmission spectrum. In Fig. 2.4 a 2D photonic crystal with a point defect is illustrated. The spectral position of the defect mode is sensitive to changes of the refractive index in its surrounding and serves as sensor signal [4, 7]. Also other configurations of photonic crystal sensors such as waveguide-based sensors [55] or photonic crystal fiber sensors [56] have been implemented.

Photonic crystals exhibit strong light confinement resulting in small sensing areas. Thus, only low analyte consumption is required [4] and a dense integration of multiple sensors on one chip is possible [57, 58]. Furthermore, the sensitivity of photonic crystal sensors is high [59] allowing detection of bulk refractive index changes [57], proteins [59, 60], bacteria [61], viruses [62], DNA [63] and gases [64] at low concentrations. The on-chip integration of photonic crystals is feasible and Liang *et al.* [65] demonstrated fabrication via UV-lithography which paves the way for low-cost large-scale fabrication.

Interferometers

The operation principle of an interferometer-based sensor is illustrated in Fig. 2.5. Monochromatic laser light is coupled into a waveguide, split up into two paths with a Y-junction and joined after a fixed distance. While the reference arm is surrounded by cladding material the evanescent field in the sensing arm interacts with the analyte. Changes of the refractive index in the sensing area, e.g., caused by target molecules binding to receptors, induce a change of the optical path length. The resulting phase shift causes a change in transmitted intensity at the output of the interferometer due to interference [4, 66].

Besides the Mach-Zehnder configuration shown in Fig. 2.5 and described previously so-called Young interferometers have been realized where the two arms are not merged but changes in the interference pattern are monitored on a detector ar-

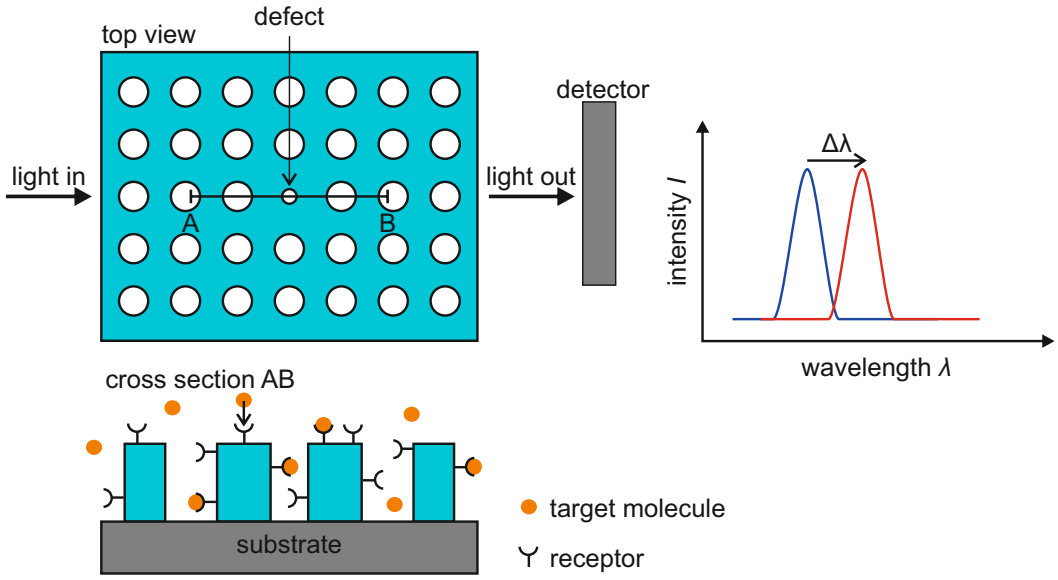

Figure 2.4: Illustration of the sensing principle of a photonic crystal. Light of a broadband source is incident on the photonic crystal. The transmitted intensity is recorded. Only the defect mode can propagate in the photonic bandgap. The defect mode has its highest field intensity around the defect making this area highly sensitive to refractive index changes. Binding of target molecules to receptors or refractive index changes induced by gas molecules will result in a spectral shift of the defect mode. Partly adapted from [58].

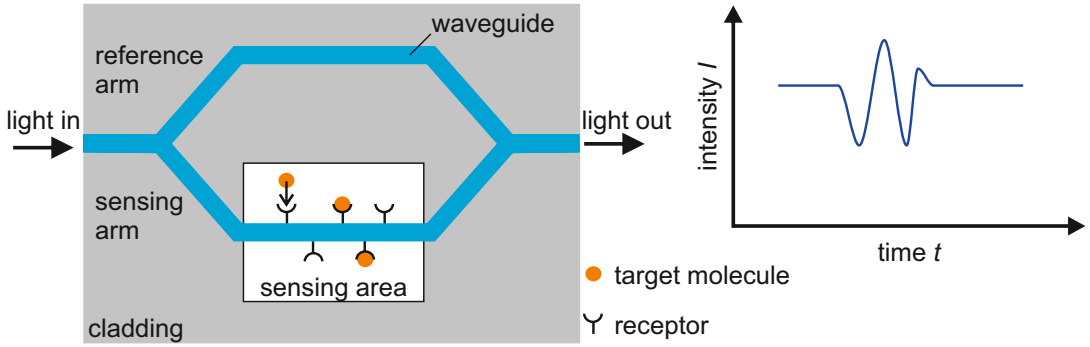

Figure 2.5: Illustration of the sensing principle of a Mach-Zehnder interferometer. Light is coupled to a waveguide, split with a beamsplitter and merged after a fixed distance. While the reference arm is covered with cladding material the sensing arm interacts with the analyte. Changes of the refractive index induce a phase change resulting in intensity changes at the output due to interference. Adapted from [4].

ray [4]. Interferometric sensors exhibit a high sensitivity and good requirements for on-chip integration [67]. Detection of bulk refractive index changes [68, 69], proteins [70], viruses [71, 72], DNA [67] and gases [73] as well as the integration with microfluidic channels has been successfully demonstrated [74]. Furthermore Ymeti *et al.* [71] developed a design with four interferometer arms even capable of multiplexing. A benchtop model of an interferometer-based sensor (*Ana*Light®, *Farfield Sensors Ltd.*, Salford, UK) allowing refractive index and thickness determination of a protein layer is commercially available [75]. However, drawbacks of interferometer-based sensors are nonlinearities in sensor response, in particular the cosine-dependence of the signal on the target molecule concentration and the fact that the sensitivity increases with larger interaction length resulting in interferometer dimensions of several mm or cm [4]. To overcome the latter a meandering pattern of the waveguides could be used.

High-Q Resonators

An optical resonator is created by confining light to a dielectric medium by using a refractive index contrast. Light propagates along a closed-loop optical path and certain wavelengths interfere constructively after one roundtrip forming a resonator mode. Simply speaking the quality factor (Q-factor) is a measure how often modes circulate in the cavity. In a high-Q resonator the light interacts multiple times with its surrounding yielding a high effective interaction length while dimensions of the resonator are in the orders of micrometers [5, 7]. Prominent examples for high-Q

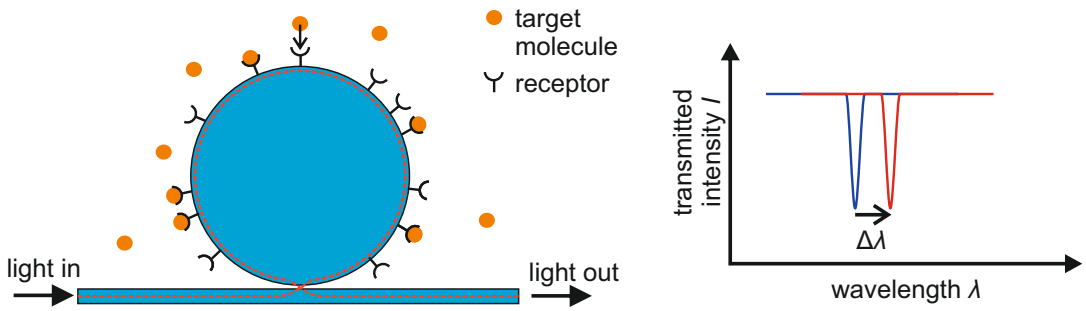

Figure 2.6: Illustration of the sensing principle of an optical resonator. A waveguide is used to couple light into the cavity. Usually a tunable laser is used for excitation and the transmission is recorded. Target molecules attaching to the resonator surface or other changes of the refractive index cause a shift of the resonator mode. Adapted from [84].

cavities with rotational symmetry are so called whispering gallery mode resonators where light is confined in a dielectric due to multiple total internal reflection. A more detailed discussion on high-Q resonators is given in section 3.1.

In Fig. 2.6 the operation principle of an optical resonator with rotational symmetry as sensor is illustrated. A waveguide is used to couple light into the cavity – typically a tunable laser is used as light source. In the transmitted intensity signal cavity modes are observed as narrow resonances since light couples to the resonator when the wavelength fulfills the resonance condition. The resonator modes exhibit an evanescent field outside the cavity interacting with the surrounding. When the refractive index of the surrounding changes a spectral shift of the resonator mode is induced [7]. Up to now high-Q resonators have been used for the detection of bulk refractive index changes [76], proteins [77], viruses [78], bacteria [79], DNA [80] and vapors [81]. Optical resonators exhibit a high sensitivity and even single molecule detection has been demonstrated successfully [10]. Additionally, on-chip integration, combination with microfluidics [82] and multiplexing is feasible [80, 83].

2.3 Summary and Conclusions

In recent years, optical sensing gained a lot of attention and a variety of sensor concepts has been developed. Concerning label-free sensors one can distinguish techniques based on optical transitions being specific to the target molecules such as absorption or Raman spectroscopy and techniques detecting refractive index changes such as SPRs, photonic crystals, interferometers and resonators. It is difficult to compare the individual sensor concepts regarding sensitivity since for each tech-

nique a variety of implementations and improvements can be found in literature. However, one can state that optical sensors can reach high sensitivities when designed appropriately. When, e.g., sensitivity towards bulk refractive index changes is considered the sensitivity of interferometers scales with the size of the sensor while for SPRs and optical resonators the sensitivity scales with the inverse size meaning that the sensitivity of optical resonators is enhanced with decreasing dimensions [5].

Concerning selectivity absorption and Raman spectroscopy identify molecules directly by characteristic optical transitions revealing energetic or vibrational energy levels. In contrast to that for refractive index based techniques receptor molecules showing specific binding to the target molecules need to be immobilized on the sensor surface. For many target molecules corresponding receptor molecules are known and different methods have been proposed how these can be immobilized on the sensor surface [7].

Since one prominent suggested application of optical sensors are disposable lab-on-chip systems besides sensor performance also on-chip integration, multiplexing, simple operation and low-cost fabrication are an issue. Currently a lot of effort in research is expended in finding and improving systems fulfilling these criteria while maintaining good sensor performance.

In this work, microlasers based on dye-doped polymers have been investigated and improved regarding their sensing properties. As the term microlaser suggests the dimensions are in the micrometer range enabling miniaturization. Furthermore, large-scale fabrication at low costs is feasible and excitation and read-out of these structures via free space optics is possible facilitating on-chip applications. In the following chapter the operation principle of these dye-lasers as well as the resonator geometries used in this work will be discussed.

Chapter 3

Dye-Doped Polymeric Microlasers

To build a laser usually a resonator, a gain medium and a pump source are required. At the beginning of this chapter important optical quantities of microresonators are discussed and the resonator types investigated in this work are introduced. Then the principle how laser dyes act as gain medium is explained. At the end of this chapter the micro-photoluminescence setup and the fiber excitation setup used for optical characterization of the resonators are presented.

3.1 Polymeric Microresonators

In this work poly(methyl methacrylate) (PMMA) has been used as resonator material. Since PMMA has low absorption losses in the visible wavelength region [85] cavities with high quality factors are feasible. Furthermore, PMMA is available as photoresist which can be patterned with either electron beam or deep-UV lithography, the latter allowing large-scale fabrication. Besides, PMMA is also suited as material for optical polymeric fibers with high transmission in the visible wavelength range [85]. After a brief discussion on the optical properties of microcavities the resonator geometries investigated in this work will be introduced – so-called whispering gallery mode resonators and ring-type resonators formed by polymeric fibers.

3.1.1 Optical Properties of Microcavities

In an optical resonator light can be confined spatially and temporally. In the following important figures of merit describing the confinement of light will be discussed.

Quality Factor

The quality factor (Q-factor) describes the temporal confinement of energy inside a cavity. The Q-factor is defined as 2π times the ratio of energy stored in the cavity U to the dissipated energy per electric field oscillation and can be expressed in dependence of the resonance frequency ω_0 and the photon lifetime τ [86]:

$$Q = \omega_0 \frac{\text{stored energy}}{\text{dissipated power}} = \omega_0 \frac{U}{-dU/dt} = \omega_0 \tau. \tag{3.1}$$

The time-dependence of the stored energy in the cavity $U(t)$ is thus given by [86]

$$U(t) = U_0 \mathrm{e}^{-\omega_0 t/Q}. \tag{3.2}$$

As can be seen by this equation a direct measurement of the Q-factor is possible with cavity-ring down spectroscopy where the temporal decay of the energy is measured [87]. Since these measurements are challenging it will be shown in the following that the Q-factor can also be determined using the spectral linewidth of the resonant mode.

Starting from Eq. 3.2 we obtain the time-dependence of the electric field via the relation $U \propto E^2$:

$$E(t) = E_0 \mathrm{e}^{-\omega_0 t/2Q} \mathrm{e}^{-i(\omega_0 + \Delta\omega)t}. \tag{3.3}$$

Here, damping is considered leading to contributions of other frequencies than ω_0 to the oscillation [86]. Applying a Fourier transformation to Eq. 3.3 yields the frequency distribution of the intensity:

$$I(\omega) = |E(\omega)|^2 \propto \frac{1}{(\omega - \omega_0)^2 + (\omega_0/2Q)^2}. \tag{3.4}$$

This represents a Lorentzian line shape with a full width at half maximum (FWHM) equal to $\delta\omega = \omega_0/Q$. Hence, the Q-factor is given by

$$Q = \frac{\omega_0}{\delta\omega} \approx \frac{\lambda_0}{\delta\lambda} \tag{3.5}$$

and can be determined from the linewidth of the resonance. Actually the Q-factor is a property of cavity modes but it is often used to describe the resonator.

Loss Mechanisms in Optical Microcavities

Several loss mechanisms limit the Q-factor of optical microcavities. Absorption, radiation and scattering are contributing loss mechanisms [88]. In contrast to these internal losses Q_{int}, external losses arise from coupling to an external coupler such as a waveguide, a tapered fiber or a prism. The reciprocal Q-factor can be decomposed

into the reciprocal sum of the individual contributions and can be expressed as [89, 90]:

$$Q^{-1} = Q_{\text{int}}^{-1} + Q_{\text{ext}}^{-1} = Q_{\text{abs}}^{-1} + Q_{\text{rad}}^{-1} + Q_{\text{sca}}^{-1} + Q_{\text{ext}}^{-1}. \tag{3.6}$$

In the following the origin of the different intrinsic loss mechanisms will be discussed and correlations to the resonator material and size will be revealed.

Absorption Losses

Absorption losses depend on the optical properties of the resonator material. The corresponding Q-factor can be approximated by [88]

$$Q_{\text{abs}} \approx \frac{2\pi n}{\alpha\lambda}, \tag{3.7}$$

where n is the real part of the refractive index of the cavity material and α is its attenuation coefficient.

In this work PMMA has been used as resonator material. The absorption losses at wavelengths in the visible spectral regime at which the cavities are operated in this work are low and by taking values from literature [91] the absorption limited Q-factor can be estimated as $Q_{\text{abs}} \approx 10^8$ for wavelengths around 600 nm.

Radiation Losses

When a cavity has curved boundaries light is not perfectly confined, meaning that part of it leaves the cavity as so-called radiation losses. In the particle picture radiation losses can be described as the tunneling of photons through the well of an effective potential [92, 93]. The height of the potential well and hence the tunneling rate depend on both the curvature of the cavity geometry and the refractive index contrast between cavity and surrounding [94]. Smaller radii of curvature and smaller refractive index contrasts increase radiation losses and lower the Q-factor. For PMMA cavities with goblet-shape and a diameter of 40 µm the radiation limited Q-factor in air is $Q_{\text{rad}} \approx 10^{16}$ for resonance wavelengths around 600 nm [11]. In water the potential barrier is lowered and the radiation limited Q-factor is $Q_{\text{rad}} \approx 10^8$ for the same cavity and wavelength [95].

Scattering Losses

Usually the surface of a cavity is not perfectly smooth but exhibits imperfections such as surface roughness acting as scattering centers [96]. These imperfections can originate from the manufacturing process but also dust deposited on the resonator surface contributes to scattering. In [89] an analytical model for the determination of Q_{sca} is presented stating that Q_{sca} depends linearly on the radius R of the cavity.

This can be attributed to a higher mode overlap with the outer cavity boundary for smaller radii. In section 3.1.2 and 4.2 a method how the surface roughness in whispering gallery mode resonators can be reduced will be presented.

Mode Volume
The mode volume V_{M} describes the spatial confinement of a mode inside and outside a cavity. The definitions vary slightly depending on the scope of application. A common definition is the ratio of the stored energy to the maximum energy density [97]

$$V_{\mathrm{M}} = \frac{\int \epsilon(\mathbf{r}) \left|\mathbf{E}(\mathbf{r})\right|^2 \mathrm{d}V}{\max\{\epsilon(\mathbf{r}) \left|\mathbf{E}(\mathbf{r})\right|^2\}}, \tag{3.8}$$

with $\epsilon(\mathbf{r})$ being the dielectric function. Depending on the spatial coordinate $\mathbf{r}$ the dielectric function of the cavity material or the surrounding is used. Usually the mode volume is given in $\mu\mathrm{m}^3$ or in units of $(\lambda/n)^3$.

Free Spectral Range
The free spectral range FSR of a cavity is the spectral distance between two consecutive longitudinal modes, i.e. between two fundamental modes with N_ϕ and $N_\phi + 1$ multiples of the wavelength λ_0 along the optical path length $L \cdot n_{\mathrm{eff}}$ of the cavity. The FSR is given by

$$FSR = \frac{\lambda_0^2}{L \cdot n_{\mathrm{eff}} + \lambda_0} \overset{\lambda_0 \ll L}{\approx} \frac{\lambda_0^2}{L \cdot n_{\mathrm{eff}}}, \tag{3.9}$$

where L is the length of the cavity. The effective refractive index of the mode n_{eff} is given by a weighted average of the refractive indices of the cavity material and the surrounding where the weights depend on the spatial distribution of the electric field.

3.1.2 Whispering Gallery Mode Resonators

So-called whispering gallery mode (WGM) resonators represent one type of optical cavities with promising applications in sensing [6], cavity quantum electrodynamics [98], optical communication [99, 100] and non-linear optics [101, 102]. The name originates from acoustic whispering galleries such as the dome of St. Paul's Cathedral in London. A person standing on one side of the dome can clearly hear the whisper of another person standing on the opposite side. Lord Rayleigh explained this phenomenon with repeated lossless reflections of the sound wave at the wall of

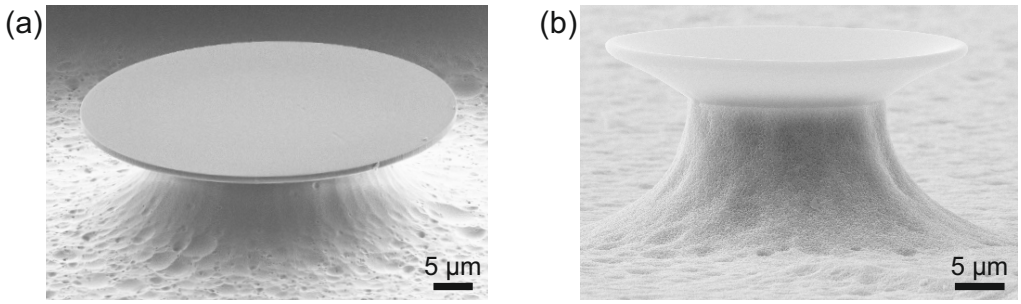

Figure 3.1: Scanning electron microscopy (SEM) images of PMMA microresonators in disc and goblet shape on silicon pedestals. (b) taken from [109].

the dome [103]. In the optical domain WGMs can exist in curved cavities due to repeated total internal reflection of the light along the cavity boundary. The waves which interfere constructively after one roundtrip are called WGM resonances. Usually WGM resonators exhibit rotational symmetry and have been realized as, e.g., spheres [76–78, 104], discs [105], toroids [87, 106] and goblets [107]. The resonance condition for cavities with rotational symmetry is given by

$$2\pi R n_{\text{eff}} = N_\phi \lambda_0, \tag{3.10}$$

where R is the cavity radius, n_{eff} is the effective refractive index of the resonant mode and λ_0 is the resonance wavelength in vacuum. The integer N_ϕ is called azimuthal mode number and states how many wavelengths fit on the circumference of the cavity.

The field distribution of the WGMs can be obtained by solving Maxwell's equations. For highly symmetric geometries such as spheres or cylinders an analytical solution of the problem is possible. In this work disc- and goblet-shaped resonators as shown in Fig. 3.1 were investigated. Borselli *et al.* developed an analytic approximation to calculate the field distribution of microdiscs [89] by using cylindrical coordinates and separation of variables. For the z-component the same results as for a slab waveguide are obtained [108], the solutions for the azimuthal part are given by $\Phi(\phi) = \mathrm{e}^{\pm i N_\phi \phi}$. The radial solutions are given by Bessel functions inside the disc and by Hankel functions outside the disc, which can be approximated by a decaying exponential with the decay constant $l = k_0 \sqrt{n_{\text{eff}}^2 - n_{\text{sur}}^2}$ with the vacuum wave number k_0 and the refractive index of the surrounding n_{sur}.

Besides analytical approximations numerical calculations can be used to determine the field distribution of more complex cavity geometries. WGM modes are classified according to three mode numbers, N_ϕ, N_ρ and N_{z}, where N_ρ and N_{z} denote the number of energy density maxima minus one in ρ- and z-direction, respectively.

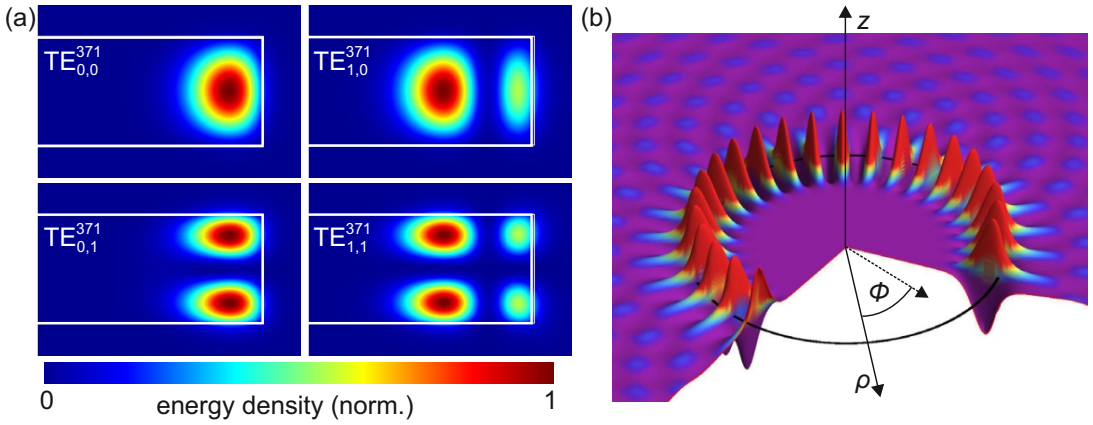

Figure 3.2: Simulated energy density and electric field distribution in PMMA disc cavities. (a) Energy density distribution for different TE modes with $N_\phi = 371$ of a disc resonator with a radius of 25 µm obtained with finite element simulations performed with JCMSuite from *JCMwave*. The energy density distribution in the ρ-z-plane close to the rim of the cavity is plotted. Modes with only one field maximum along ρ- and z-direction are named fundamental modes. (b) Electric field distribution of a fundamental mode with $N_\phi = 30$. The exponentially decaying evanescent field outside the cavity is clearly visible. Adapted from [109].

Furthermore, two polarization states, transverse electric (TE) and transverse magnetic (TM) are distinguished, where for TE (TM) modes the electric (magnetic) field lies in the resonator plane. In Fig. 3.2 the simulated energy density close to the rim of a PMMA disc resonator with a radius of 25 µm is depicted for different modes. Furthermore, the three-dimensional field distribution of a fundamental mode ($N_\Phi = 0$, $N_\rho = 0$) is illustrated. One can clearly recognize the exponentially decaying evanescent field outside the cavity which is crucial for sensing.

With WGM resonators high Q-factors can be achieved, e.g., for fused-silica microspheres Q-factors close to the limit given by bulk absorption have been measured (8×10^9 at 633 nm) [110]. For on-chip resonators the use of surface-tension induced reflow processes such as heating silica cavities with a CO_2 laser above their glass transition temperature allows efficient surface smoothening going along with Q-factor enhancement [87, 107].

3.1.3 Ring Resonators

In ring resonators light is usually guided in an optical waveguide which is looped back on itself [111]. Arbitrary geometries are feasible as long as a closed optical path is formed. For example ring resonators, racetrack rings and folded spiral rings have been realized [111]. The condition for constructive interference is the same as for WGM resonators (see Eq. 3.10) except that $2\pi R$ is replaced by the length of the ring resonator L.

As waveguide structure planar optical waveguides such as slab waveguides or rectangular waveguides are applicable but also optical fibers can be used to form ring resonators. In the following, waveguiding in circular step-index fibers will be explained since the PMMA fibers used in this work belong to that category.

The diameter of the PMMA fibers is of the same order of magnitude as the wavelength of the propagating light meaning that the wave nature of light needs to be considered. An optical fiber usually consists of a core with refractive index n_{core} and a surrounding cladding with refractive index n_{clad} where the mode is guided by the core due to $n_{\text{core}} > n_{\text{clad}}$ (see Fig. 3.3). In our case bare core fibers are used so that n_{clad} is equal to the refractive index of the surrounding n_{sur}. To obtain the field distribution and the propagation constants of the modes (modes propagate along z-direction) Maxwell's equations are solved for the given refractive index distribution. Since a detailed derivation of the solutions can be found in many textbooks [112–114], only the solutions will be discussed briefly.

Three types of modes can be distinguished: hybrid modes, transverse electric (TE) and transverse magnetic (TM) modes. While for hybrid modes all six components of the electric and magnetic field are nonzero, for TE (TM) modes $E_z = E_\rho = H_\phi = 0$ ($H_z = H_\rho = E_\phi = 0$) applies (see Fig. 3.3 (a) for coordinate system). The z-component of the electric (magnetic) field is given by zero order Bessel functions of the first kind for the core region and modified zero order Bessel functions of the second kind for the cladding. The remaining field components are then determined via Maxwell's equations and are also given by Bessel functions of the first kind or modified Bessel functions of the second kind. For hybrid modes, solutions are bulkier but again contain the above-mentioned Bessel functions.

Since for both WGM resonators and circular step-index fibers the geometry of the dielectric is a cylinder it is no surprise that the solutions for Maxwell's equations are Bessel functions in both cases. However, differences are the dimensions of the dielectric and the propagation direction resulting in different kind of modes. For WGM resonators the modes propagate along the rim of the disc while for fibers the modes propagate along the direction perpendicular to the disc plane. In Fig. 3.3 (b)

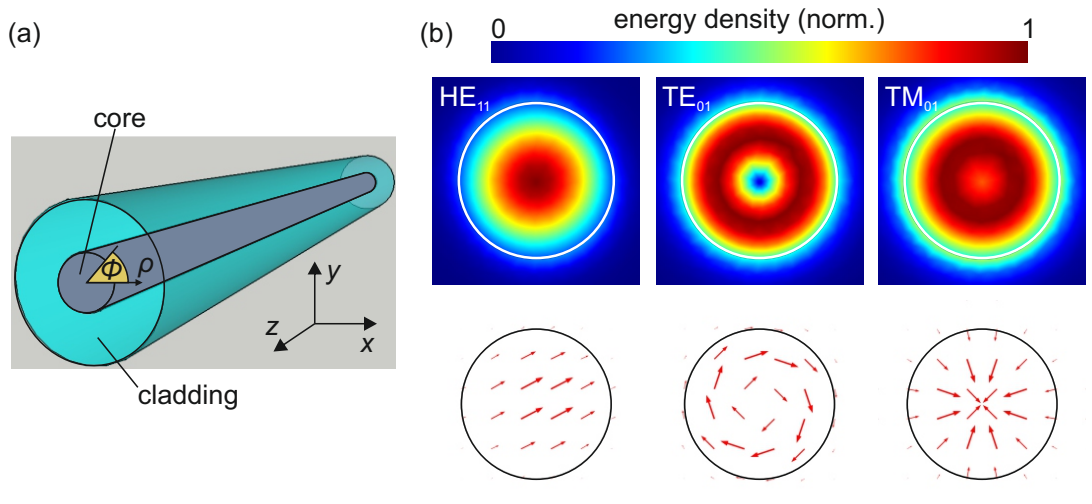

Figure 3.3: Optical modes in cylindrical fibers. (a) Schematic of an optical cylindrical fiber with core and cladding. The modes propagate along z-direction. (b) Electric field density distribution for different modes (top) and electric field distribution in the x-y-plane (bottom) for a PMMA fiber with a diameter of 1 µm calculated with COMSOL.

the electric energy density and the electric field in the x-y-plane for the fundamental mode (HE_{11}) and the TE_{01} and TM_{01} mode of a PMMA fiber are depicted. The first index denotes the order of the Bessel function and the second index denotes the number of radial roots.

For every fiber the normalized frequency V, which depends on the fiber diameter d, the wavelength λ_0, and the refractive indices of core n_{core} and cladding n_{clad}, is determined by

$$V = \frac{\pi d}{\lambda_0}\sqrt{n_{\text{core}}^2 - n_{\text{clad}}^2}. \tag{3.11}$$

When $V < 2.405$ only the fundamental mode (HE_{11}) is allowed and the fiber becomes single-mode.

Very often the so-called weakly guiding approximation is used to describe the mode propagation in fibers. This approximation is valid when the refractive index contrast between core and cladding is small ($\Delta n \approx 1\,\%$). For PMMA fibers the refractive index contrast Δn between core (PMMA) and "cladding" (air, water) is 0.49 or 0.16, meaning that the weakly guiding approximation cannot be applied [112] which is why this approximation is not discussed here.

The Q-factors reported for ring resonators (e.g., $Q = 1.4 \times 10^5$ at 1550 nm [115]) are several orders of magnitude lower than for WGM cavities. This is mainly due to

the different fabrication processes – for ring resonators no surface-smoothing reflow steps are used to reduce losses due to surface scattering. However, for sensing other figures of merit besides the Q-factor are important which is why successful sensing experiments have also been demonstrated with ring resonators [116].

3.2 Laser Dyes as Active Material

The gain medium of a laser strongly influences its performance. In order to obtain low lasing thresholds an efficient active material with high amplification needs to be integrated into the resonator without deteriorating the cavity properties. Furthermore, the optical transitions of the active material define the spectral region of lasing emission. In case of polymeric cavities organic lasing dyes can easily be integrated into the host matrix. Laser dyes are available with different emission wavelengths ranging from near-ultraviolet to near-infrared [117]. At the beginning of this section the electronic structure of laser dyes is discussed and the conditions required for lasing are summarized. Afterwards the optical properties of the laser dye Pyrromethene 597 (PM597), which is mainly used in this work, are presented in detail.

3.2.1 Electronic Structure of Laser Dyes

In [117] the term "dye" is used in a sense that it comprises all substances exhibiting conjugated double bonds since these bonds are crucial for optical transitions. Molecules without double bonds absorb photons with wavelengths smaller than 160 nm corresponding to an energy which is sufficient to dissociate most chemical bonds. Thus, double or triplet bonds containing delocalized π-electrons are required to enable light absorption at wavelengths larger than 200 nm [117]. The π-electrons form an electron cloud which extends over the conjugated bonds.

Electron in a Box Approximation
In a simple picture absorption in dyes can be understood by describing the conjugated double bond chain as an infinite potential well. The energy E_n of the nth eigenstate of an electron in this potential is given by

$$E_n = \frac{h^2 n^2}{8mL^2}, \tag{3.12}$$

where h denotes Planck's constant, n denotes the number of antinodes of the eigenfunction along the chain, m the electron mass and L the length of the conjugated

chain [117]. Each energy level can be occupied by two electrons due to Pauli's principle so that for N electrons $n = N/2$ states will be occupied (usually N is an even number). Absorption of a photon induces an electronic transition from the highest occupied state to the lowest unoccupied state with the transition energy

$$\Delta E_{\min} = E_{N+1} - E_N = \frac{h^2}{8mL^2}(N+1), \tag{3.13}$$

which can be translated into the wavelength of the incoming photon via $\lambda = hc_0/\Delta E$. This approximation predicts the absorption bands of molecules with long conjugated chains adequately, however, for small molecules repulsion between π electrons needs to be considered leading to more complex formulas [117].

Transitions in Dye Molecules

The electronic energy levels in dye molecules are superimposed by a manifold of vibrational energy levels which arise from the high number of atoms. The usually broad absorption spectra (several tens of nanometers) of laser dyes originate from these vibrational energy levels [117]. The energy levels of dye molecules are illustrated in Fig. 3.4 (a): The singlet ground state, first and second electronic singlet state as well as the first and second triplet state. For each electronic energy level several vibrational states, denoted with ν in the following, exist. At room temperature absorption usually occurs from the ground state $S_{0,\nu=0}$ since thermal energy ($\approx 25\,\mathrm{meV}$) is not sufficient for a significant population of excited vibrational states which are separated by an energetic distance of approximately 190 meV [118].

Absorption of a photon excites the molecule into a higher electronic level but also changes its vibrational state. In Fig. 3.4 (b) the Franck-Condon principle which explains this behaviour is illustrated. The electronic transition occurs on a time scale of femtoseconds, a time during which the nuclei do not change their distance significantly [118]. The probability for a transition is proportional to the overlap integral of the wave functions of the nuclei of initial and final state. Since the overlap between the wave functions of the ground state $S_{0,\nu=0}$ and higher vibrational levels of the excited state $S_{1,\nu\neq0}$ is higher than the overlap of the wave functions from the ground state $S_{0,\nu=0}$ and the excited state $S_{1,\nu=0}$, the transition from S_0 to S_1 goes along with a vibrational excitation. From there the molecule rapidly relaxes ($t_{\mathrm{IC}} \approx 10^{-12}\,\mathrm{s}$) into the lowest vibrational state of S_1; this process is called internal conversion (IC) [118]. Starting from this state different processes can occur: A transition to the ground state under the emission of a photon (fluorescence) or a non-radiative transition to the ground state via internal conversion. Furthermore, a non-radiative transition to the first triplet state (intersystem crossing) can occur. It should be noted that the radiative transition to the ground state again ends at

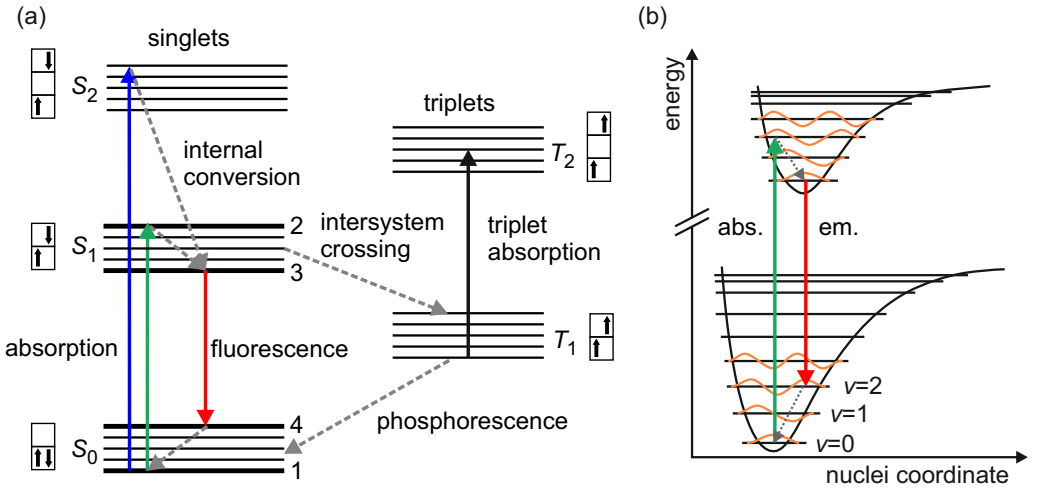

Figure 3.4: Energy levels and transitions in dye molecules. (a) Jablonski-diagram with singlet and triplet states. Absorption (green or blue) induces a transition from the ground state to a higher vibrational level of the first or second excited state. The molecule relaxes to the vibrational ground state of S_1 via internal conversion (grey dotted arrows). Fluorescence (red) occurs to a higher vibrational state of S_0 followed by internal conversion to $S_{0,\nu=0}$. The levels relevant for lasing are numbered with 1,2,3 and 4. (b) Diagram illustrating the potential and wave functions (orange) of the nuclei to visualize the Franck-Condon principle. The transition probability is proportional to the overlap integral of the wave functions. Adapted from [119] and [120].

a higher vibrational level followed by internal conversion to $S_{0,\nu=0}$. Due to the Franck-Condon principle the emission spectra of dyes are red-shifted compared to their absorption spectra – this effect is called Stokes shift. The transition from the triplet state T_1 to the ground state under the emission of a photon is referred to as phosphorescence. Since spin conversion is required the lifetime of the T_1 state is several orders of magnitude larger than the lifetime of the S_1 state [118].

Conditions for Lasing

In order to obtain lasing population inversion of the energy levels responsible for lasing emission is required, i.e., the number of molecules in the higher energetic state must exceed the number of molecules in the lower energetic state. With a two-level system population inversion is impossible so for lasing emission at least a three-level system is required [119]. Dye molecules provide four-level systems due to their vibrational states as indicated in Fig. 3.4 (a). Through absorption the dye

molecule is excited from level 1 to level 2, followed by a fast relaxation ($\sim 10^{-12}\,\mathrm{s}$) to level 3. Since the timescale for radiative relaxation is in the order of nanoseconds (compared to $t_{\mathrm{IC}} \approx 10^{-12}\,\mathrm{s}$) molecules accumulate in level 3 while also level 4 is quickly depleted. Thus, population inversion is build up between level 3 and 4 and consequently, lasing occurs from this transition [117]. Note that level 3 and 4 can be any of the excited vibrational states of S_0 and S_1.

For optical feedback the dye molecules are embedded in a cavity. To achieve lasing operation the optical gain per roundtrip needs to overcome the roundtrip losses at the lasing wavelength [121]:

$$n_1\sigma_{\mathrm{e}}(\lambda) \geq \frac{2\pi n}{\lambda Q} + n_0\sigma_{\mathrm{a}}(\lambda). \tag{3.14}$$

Here, $\sigma_{\mathrm{e}}(\lambda)$ and $\sigma_{\mathrm{a}}(\lambda)$ are the cross-sections of stimulated emission and absorption, respectively, n_1 is the number density (per unit volume) of dye molecules in the first excited singlet state, n_0 is the number density of dye molecules in the ground state, n is the refractive index and Q the quality factor. The stimulated emission cross section, which is required to determine the lasing threshold, can be calculated by [117]:

$$\sigma_{\mathrm{e}}(\lambda) = \frac{\lambda^4 f(\lambda)\Phi_{\mathrm{f}}}{8\pi c_0 n^2 \tau}. \tag{3.15}$$

The normalized photoluminescence spectrum is denoted $f(\lambda)$, Φ_{f} is the fluorescence quantum yield, c_0 the vacuum speed of light, n the refractive index and τ the fluorescence lifetime. Typical emission cross sections for dye molecules are in the order of $10^{-16}\,\mathrm{cm}^2$ [119], which is several orders of magnitude larger than those of lanthanides which are often used in solid state lasers as gain medium [122, 123].

To fulfil Eq. 3.14 a minimum fraction of molecules $\gamma = n_1/n_{\mathrm{t}}$ must be excited, with n_{t} denoting the total number density of dye molecules. Eq. 3.14 can then be rewritten as follows [124]:

$$\gamma(\lambda) \geq \frac{2\pi n/(\lambda Q n_{\mathrm{t}}) + \sigma_{\mathrm{a}}(\lambda)}{\sigma_{\mathrm{a}}(\lambda) + \sigma_{\mathrm{e}}(\lambda)}. \tag{3.16}$$

The lasing threshold, i.e., the minimum excitation power fluence required to achieve lasing is proportional to γ, so one can clearly see from Eq. 3.16 that the lasing threshold mainly depends on the Q-factor and the number density of dyes in the cavity. However, simply increasing the dye concentration will not automatically lower the lasing threshold as for high dye concentrations formation of dimers and higher aggregates might occur leading to fluorescence quenching [125]. Furthermore, the aggregates exhibit a red-shifted absorption band compared to single dyes going along with a reduced Q-factor at the lasing wavelength [117].

Influence of Triplet States on Lasing Performance and Photobleaching
As mentioned in the previous paragraph excited dye molecules can undergo a non-radiative transition to the first excited triplet state T_1 via intersystem crossing from S_1. This transition can be induced, e.g., by spin–orbit coupling or due to collisions with molecules in the solvent [117]. A population of the first triplet state has negative impact on the lasing performance since it reduces the fluorescence quantum yield Φ_f significantly below unity. For one thing it reduces the population of S_1 and hence the amplification, for another thing it increases triplet–triplet absorption losses [117]. Additionally dye molecules in the triplet state are chemically more reactive. Hence, population of the triplet state might lead to enhanced photobleaching due to reactions of dye molecules with oxygen [126].

The population of triplet states can be avoided if the rise time of the pump pulses until they overcome the lasing threshold is short compared to typical transition times for intersystem crossing which are in the order of $\tau_\mathrm{ISC} \approx 100\,\mathrm{ns}$ [117, 127].

3.2.2 Properties of Pyrromethene 597

The emission of laser dyes belonging to the pyrromethene family (4,4-difluoro-3a,4a-diaza-4-bora-s-indacene dyes) lies in the green-yellow to red spectral region [128]. Fig. 3.5 shows the chemical structure and both the absorption and stimulated emission cross section of the gain material used in this work, Pyrromethene 597 (PM597). To determine the absorption and stimulated emission cross section of PM597 in PMMA the transmission and absorption spectrum were measured for a PM597-doped PMMA film spin-coated on a glass slide. The concentration of PM597 was the same as used in the cavities (25 µmol/g PMMA) to ensure comparability. The transmission spectrum is used to derive the absorbance $A(\lambda)$ which is used to determine the extinction coefficient $\epsilon(\lambda)$ via Beer-Lambert law

$$A(\lambda) = -\log\left(\frac{I_\mathrm{T}}{I_0}\right) = c \cdot l \cdot \epsilon(\lambda), \tag{3.17}$$

where c is the dye concentration and l the film thickness. The absorption cross section can then be calculated with the following formula [117]

$$\sigma_\mathrm{a}(\lambda) = 0.385 \cdot 10^{-20} \epsilon(\lambda), \tag{3.18}$$

where $\epsilon(\lambda)$ needs to be in liter/(mol · cm). The emission cross section was calculated from the emission spectrum by using Eq. 3.15. The fluorescence quantum yield was measured by Andrey Turshatov from the Institute of Microstructure Technology (IMT, KIT) to be $\Phi = 0.63$ for PM597 embedded in PMMA excited with light of

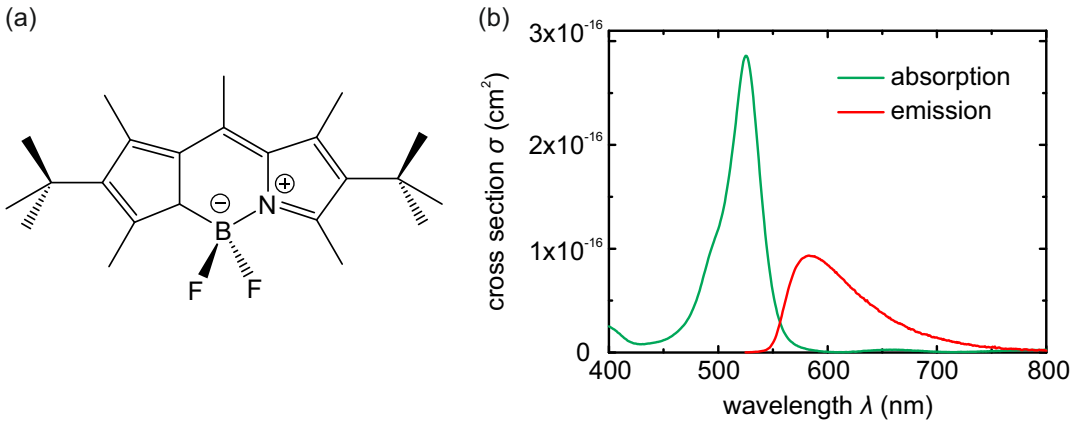

Figure 3.5: Properties of the laser dye Pyrromethene 597 (PM597). (a) Chemical structure of the laser dye PM597. Taken from [131]. (b) Absorption and stimulated emission cross section of PM597 embedded in PMMA. Both the absorption and emission cross section were calculated from transmission and emission spectra with the formulas and parameters given in the text.

$\lambda = 532\,\mathrm{nm}$ which is typically also used in this work. For the fluorescence lifetime the value of $\tau = 6.22\,\mathrm{ns}$ was also determined by A. Turshatov and is comparable to values in literature [129]. Pyrromethene dyes are highly efficient and photostable laser dyes [128] which show good solubility in many solvents [130] and can easily be embedded in polymer matrices such as PMMA. The good laser performance arises from the low intersystem crossing rate and low triplet–triplet absorption [130]. For PM597-doped WGM resonators with goblet shape lasing thresholds as low as $0.5\,\mathrm{nJ}$ per pulse and stable lasing emission for more than 2×10^6 pulses has been demonstrated in previous research done in our group [11].

3.3 Optical Setups Used for Investigating Dye-Doped Microcavities

During this work two different optical setups where used to characterize the polymeric cavities: A micro-photoluminescence spectroscopy setup for excitation of the lasing modes via free-space optics and a fiber-coupling setup to investigate the passive Q-factors of the cavities.

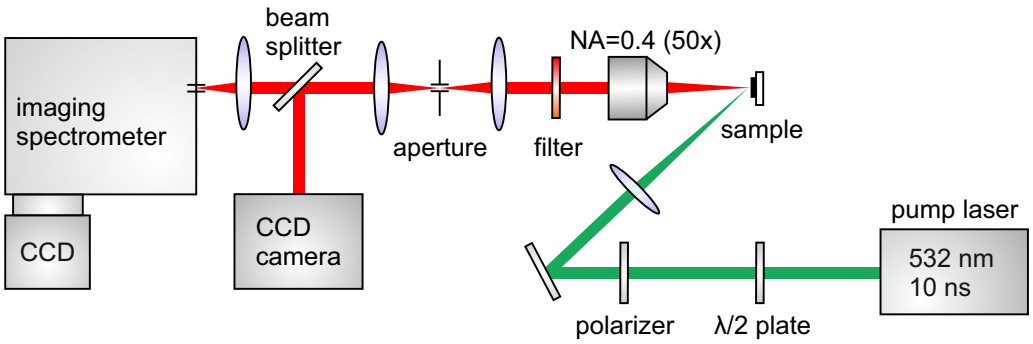

Figure 3.6: Micro-photoluminescence setup. Laser light of 532 nm is focused onto the sample to excite the dye molecules in the cavities. A microscope objective collects the emission light which is guided to a CCD camera to obtain an image of the sample and to a second CCD camera coupled to a spectrometer for spectral analysis. Based on [132].

3.3.1 Micro-Photoluminescence Spectroscopy Setup

A schematic of the micro-photluminescence (µ-PL) spectroscopy setup used in this work is shown in Fig. 3.6. A frequency-doubled Nd:YVO_4 laser emitting pulses of approximately 10 ns at 532 nm matching the absorption spectrum of PM597 serves as pump source. As mentioned before, the short pulse duration prevents a detrimental population of triplet states. The excitation energy can be controlled by a half-wave plate followed by a variable linear polarizer. The light is loosely focused on the sample with a lens under an angle of approximately 45°.

A microscope objective with 50-fold magnification and a numerical aperture of 0.42 is used to collect the emitted light. Since the detection beam path is perpendicular to the resonator plane the observable lasing emission from the sample results from scattering processes at resonator surface imperfections. A long-pass filter in the detection beam path filters light of the excitation wavelength. In order to obtain an image of the sample and an emission spectrum simultaneously a beam splitter divides the emission light into two parts. 30 % of the light are focussed directly onto a charged coupled device (CCD) camera while the remaining 70 % are focussed on the entrance slit of the spectrometer (f = 50 cm) having a CCD camera (256 × 1024 pixel) attached. The spectrometer is equipped with three gratings with 150 lines/mm, 1200 lines/mm or 2400 lines/mm, resulting in spectral resolutions of approximately 700 pm, 70 pm and 35 pm, respectively, at wavelengths around 600 nm when the entrance slit set to 30 µm.

3.3.2 Fiber Excitation Setup

One method to excite WGMs also in cavities without active components is to use tapered fibers which are approached closely to the rim of the resonator. With this method the Q-factor of a cavity can be determined by measuring the spectral width of the resonant modes.

Single mode fibers consist of a core surrounded by a cladding. Due to the small refractive index contrast between core and cladding a high fraction of the fiber mode propagates inside the cladding. In order to access the evanescent field of a fiber mode the cladding needs to be removed and a tapered fiber where the evanescent field propagates in air needs to be fabricated. Usually the so-called flame brushing technique is used to fabricate single-mode tapered fibers. A small region of the fiber is heated with a flame and pulled apart with motorized stages [133]. During the pulling process multiple modes can propagate through the fiber. When the tapered region is thin enough the fiber becomes single-mode again and hence the pulling process is stopped. More details on the fabrication of tapered fibers can be found in [134].

A schematic of the setup for fiber coupling is depicted in Fig. 3.7. The light of a tunable laser with a linewidth of $\delta\omega < 300\,\mathrm{kHz}$ and a sweep range from 632.5 nm to 637 nm is coupled into a single-mode tapered fiber. In order to align the fiber precisely with respect to the resonator the fiber is mounted onto a five-axis positioning stage which can be moved with a precision of 10 nm. The wavelength of the tunable laser is swept continuously and the transmission is monitored with a photodiode. When the fiber is close enough to the cavity so that the light from the fiber evanescently couples to the cavity, the modes are observed as Lorentzian-shaped dips in the transmission spectrum. In order to conduct measurements in aqueous environment a sample chamber with two open sides is used. The open sides ensure that the tapered fiber can be approached to the resonator. A microscope cover slip is used to cover the chamber and the water is kept inside by capillary forces.

3.4 Summary and Conclusions

In this chapter the components required for a microlaser have been presented. First, figures of merit for cavities such as Q-factor, mode volume and free spectral range have been discussed before the resonator types of this work have been introduced. For both types, the WGM resonators and the cylindrical fibers, Bessel functions solve Maxwell's equations since the WGM cavities and the fibers exhibit similar

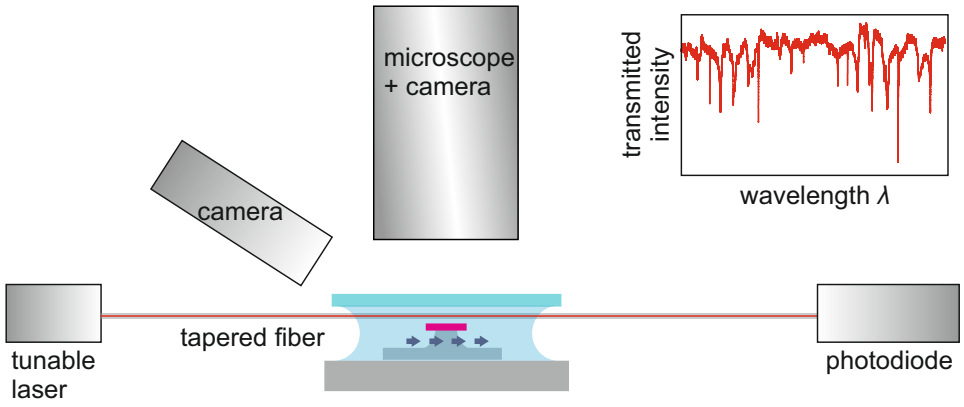

Figure 3.7: Tapered-fiber setup to excite the cavity modes and to measure Q-factors. The light of a tunable laser is coupled into a single-mode tapered fiber. The fiber is approached to the resonator and the transmission spectrum is recorded with a photodiode. Cavity modes appear as Lorentzian dips in the transmission spectrum. Adapted from [134].

geometries. However, typical dimensions and mode propagation are different for the two resonator types. In WGM cavities modes propagate along the rim of the cavity which is a disc or a goblet in our case. For ring resonators a fiber or waveguide is used for mode-guiding and a closed-loop optical path is formed. The geometry of the fiber resonators used in this work will be discussed in detail in chapter 6. Q-factors of WGM cavities exceed those of ring resonators by orders of magnitude but both cavity types have been successfully implemented for sensing [6, 116].

Dye molecules represent an efficient gain medium as they exhibit high cross sections for stimulated emission and the four-level system allows for an easy build-up of population inversion [119]. The electronic structure and transitions relevant for lasing performance have been discussed. The laser dye Pyrromethene 597 can easily be integrated into a PMMA matrix and exhibits a high quantum yield. Furthermore, previous results on WGM cavities doped with PM597 have shown that these cavities exhibit low lasing thresholds and long lifetimes of the lasing emission [11]. The good lasing performance of PM597 can be attributed to its low intersystem crossing rate and low triplet–triplet absorption.

At the end of this chapter the µ-PL setup has been presented representing a simple excitation and read-out scheme for dye-doped cavities. Also the fiber excitation setup for determining the passive Q-factors of the cavities was introduced. In the following modifications of dye-doped polymeric cavities will be presented and techniques on improving the sensitivity of PM597-doped WGM resonators will be demonstrated. Furthermore, resonators based on dye-doped electrospun fibers and their applications in sensing will presented.

Chapter 4

Polymeric Whispering Gallery Mode Lasers as Sensors

This chapter focusses on WGM resonators and their applications in sensing. First it will be explained how WGM cavities work as sensors and which quantities influence the sensor signal. Then an overview on different implementations of WGM resonators in their use as sensors in literature is given. Afterwards advantages of polymeric WGM lasers and the standard fabrication process used in this work is presented. The fact that the resonators are made of polymeric materials allows for the incorporation of different gain materials such as laser dyes or quantum dots. In this chapter the results obtained with the laser dye Fluorol 7GA are shown which can be optically pumped even with a low-cost laser diode. Furthermore, a modified fabrication process was developed which allows fabrication of the resonators on arbitrary substrates and their implementation in an all-polymeric sensor chip.

4.1 Sensing with Whispering Gallery Mode Cavities

Since whispering gallery modes exhibit an evanescent field outside the cavity they are able to interact with their surrounding. Changes in the surrounding, e.g., caused by biomolecules or bulk changes cause a spectral shift of the resonant mode which serves as sensor signal. In the following the so-called reactive sensing principle is introduced which gives a quantitative description of the expected shift upon the attachment of molecules to the resonator.

4.1.1 Reactive Sensing Principle

From the resonance condition given in Eq. 3.10 it is evident that the resonant wavelength is sensitive to the optical path length of the resonator. This results in the following formula describing the relative wavelength shift $\Delta\lambda_0/\lambda_0$ upon changes of the radius R or the effective refractive index n_{eff} [84]:

$$\frac{\Delta\lambda_0}{\lambda_0} = \frac{\Delta R}{R} + \frac{\Delta n_{\text{eff}}}{n_{\text{eff}}}. \tag{4.1}$$

In a simplified picture one can consider a monolayer of biomolecules, which have the same refractive index as the cavity, attaching to the resonator surface as an increase in radius. The resonant modes will "see" a cavity with larger radius and the resonant wavelengths will increase as the azimuthal mode number remains constant. The effective refractive index of the resonant modes depends on the field distribution of the WGMs and on the refractive indices of the cavity and its surrounding. Hence, changes of the refractive index of the surrounding will also cause a spectral shift of the resonant modes.

Usually, biomolecules do not form a complete monolayer but attach to the resonator one by one and cover only parts of the rim. Arnold *et al.* [135] used first order perturbation theory to determine the wavelength shift caused by single or multiple molecules. When a molecule attaches to the resonator surface it is polarized by the evanescent field of the WGM. A dipole moment $\delta\boldsymbol{p}_{\text{i}} = \alpha \cdot \boldsymbol{E}_0(\boldsymbol{r}_{\text{i}})$, which depends on the polarizability α of the molecule, is induced. The shift of the resonant mode is given by the ratio of the energy required for inducing the dipole to the total energy of the mode [135]:

$$\left(\frac{\Delta\lambda_0}{\lambda_0}\right) = -\left(\frac{\Delta\omega_0}{\omega_0}\right) \approx \frac{\alpha\left|\boldsymbol{E}_0(\boldsymbol{r}_{\text{i}})\right|^2}{2\int \epsilon(\boldsymbol{r})\left|\boldsymbol{E}_0(\boldsymbol{r})\right|^2 \mathrm{d}V}. \tag{4.2}$$

Here, $\epsilon(\boldsymbol{r})$ denotes the dielectric fundtion. The resonance shift caused by a molecule is proportional to its polarizibility α and the square of the electric field at the position where the molecule attaches $\left|\boldsymbol{E}_0(\boldsymbol{r}_{\text{i}})\right|^2$. In [135] the transition from single to multiple molecules is considered and the electric fields at the resonator surface are evaluated for a spherical resonator. By using approximations for the integral in the denominator the following simple formula for the relative wavelength shift is obtained:

$$\frac{\Delta\lambda_0}{\lambda_0} = \frac{\alpha\sigma}{\epsilon_0(n_{\text{res}}^2 - n_{\text{sur}}^2)R}. \tag{4.3}$$

Here, σ is the surface density of the molecules, ϵ_0 is the vacuum permittivity and n_{res} and n_{sur} are the refractive indices of the resonator and the surrounding.

One method to evaluate the performance of a cavity as sensor is the measurement of the so-called bulk refractive index sensitivity (BRIS). It describes how sensitive the cavity is towards changes of the refractive index of the surrounding. More details on the BRIS and its measurement will be given in section 5.1. Zhu *et al.* derived that the shift caused by attaching molecules is proportional to the BRIS S_{BRIS} and is given by [136] :

$$\frac{\Delta\lambda_0}{\lambda_0} = \sigma\alpha\frac{2\pi\sqrt{n_{\mathrm{res}}^2 - n_{\mathrm{sur}}^2}}{\epsilon_0\lambda^2}\frac{n_{\mathrm{res}}}{n_{\mathrm{sur}}^2}S_{\mathrm{BRIS}}. \tag{4.4}$$

This equation shows that the BRIS can be used to quantify the sensing ability of WGM resonators.

In order to realize WGM sensors which selectively detect certain molecules, e.g., a particular protein, the surface of the resonators has to be functionalized. So-called receptor molecules showing specific binding to the target molecules are immobilized on the cavities. Since functionalization is beyond the scope of this work the reader is referred to the review articles [5, 6] for further information.

4.1.2 Implementations of WGM Sensors in Literature

WGM resonators have attracted a lot of interest in recent years and many implementations as sensors have been realized. Different geometries of WGM resonators include, e.g., spheres [77], toroids [87], discs [137], goblets [107] and microbubbles [138]. Furthermore, a broad variety of materials has been used to fabricate WGM cavities with quartz glass (silica, SiO_2) being the most prominent one [84, 139]. But also other materials, such as titanium dioxide (TiO_2) [140], silicon carbide (SiC) [141], silicon nitride (Si_2N_3) [142], polymethylsiloxane (PDMS) [143] and magnesium fluoride (MgF_2) [144] have been used as cavity material. The following section will give a brief overview on different sensing techniques. For more detailed information the reader is referred to the extensive review article of Foreman, Swaim and Vollmer [6].

Usually tapered optical fibers or prisms are used for evanescent excitation of the WGMs. In Fig. 3.7 a schematic of the most common setup is depicted. A tunable laser with narrow linewidth is coupled into a tapered fiber and the transmission spectrum at the end of the fiber is detected with a photodiode. Different methods have been implemented in order to track the resonant mode. The simplest and most common principle is to measure the transmission spectrum and then apply post-processing procedures to extract the resonance position. Usually a Lorentzian is fitted to the data and the center wavelength is monitored. The spectral resolution depends on the frequency accuracy and amplitude noise of the tunable laser and time resolution depends on the actuator used for detuning of the laser.

In general one can say that the detection limit is given by the ratio of the resolution of the system to the sensitivity of the transducer. In order to obtain a low detection limit either the noise has to be reduced or the shift caused by target molecules has to be increased. Several techniques have been realized for both approaches almost all of them working with passive WGM cavities. In the following different approaches from literature are presented. A detailed discussion how the detection limit can be improved for the WGM lasers used in this work is given in the chapter 5.

Frequency Locking

In order to suppress frequency fluctuations of the emission wavelength of the tunable laser its frequency is locked to the resonance frequency of the WGM cavity. This allows real-time measurement of the resonator mode and yields a high time-resolution which is desirable when single molecule binding events are to be monitored. When the frequency locking is done with the Paul-Drever-Hall method the created error signal and thus the locking method is insensitive to amplitude noise of the laser [145, 146]. Swaim *et al.* applied this technique first to WGM resonators and could demonstrate the detection of single gold nanorods with a size of 39 nm $\times$ 10 nm [147]. Recently, Su *et al.* further improved this method, applied computational filtering to the data and were able to detect single nanoparticles of 2.5 nm radius, molecules of 15.5 kDa and even single exosomes [9, 148].

Mode-Splitting and Linewidth Broadening

In an ideal WGM resonator with rotational symmetry the WGMs are two-fold degenerate. Tiny imperfections or attaching nanoparticles introduce coupling of the two counterpropagating modes via backscattering and lift the degeneracy yielding resonances splitted into doublets [149]. Furthermore, each particle attaching to the cavity surface can introduce additional scattering and absorption losses broadening the resonance linewidth [6, 150].

Both linewidth broadening and the strength of mode-splitting can be used as signals for sensing. The mode-splitting can be resolved when the splitting exceeds the linewidth of the individual modes – a condition which strongly depends on the Q-factor of the cavity [151, 152]. Both detection schemes are less sensitive to environmental noise induced by temperature changes or frequency drifts of the tunable laser than the method where the spectral position of the lasing peak is tracked [151]. In [152] the detection of single polystyrene particles and of single viruses has been demonstrated by using the linewidth broadening as sensor signal. By extracting the splitting and the linewidth broadening from a single measurement Zhu *et al.* were able to detect and to size individual nanoparticles down to a diameter of 60 nm [151]. Furthermore, He *et al.* incorporated Er^{3+} ions into toroidal silica resonators to ob-

tain WGM lasers with continuous wave emission [153]. In this case the size of the mode-splitting can be accessed via the frequency of the resulting beat note signal. Single viruses and nanoparticles have successfully been detected with this method [106].

Plasmonic Enhancement
The shift of a WGM upon binding of particles or biomolecules depends on the electric field strength at the binding position as can be seen from Eq. 4.2. Hence, a local field enhancement at the binding site will increase the sensitivity of the cavity and yield higher shifts [154,155]. By attaching gold nanoshells to WGM spheres made of silica Dantham *et al.* were able to detect single viruses as the shift upon attachment was increased by a factor of 70 compared to a bare WGM sphere [139]. In 2013, the same group succeeded in detecting single cancer markers and proteins with masses as low as 1 ag or 0.11 ag, respectively [10]. Again they used hybrid gold nanoshell-WGM resonators and they explained the high amplification factors with small bumps on the gold nanoshells causing additional field enhancement [10]. In 2014, Baaske *et al.* studied single nucleic interaction kinetics for matched and mismatched DNA strands by binding gold nanorods to silica WGM cavities for amplification [156].

As pointed out in this subsection a lot of effort has been invested to boost the detection limit down to single molecules or even single nucleic interactions. However, excitation and read-out of the WGMs has been realized by using tapered fiber coupling or coupling to a prism. Both techniques require sophisticated alignment procedures and are thus limited to research laboratories up to now. Tapered fibers additionally are fragile and degrade within hours to days. For these reasons in this work WGM lasers have been used which can be excited and read out via free-space optics.

4.2 Fabrication of Dye-Doped Polymeric Disc- or Goblet-Shaped Cavities

As mentioned in chapter 3 the WGM cavities investigated in this work are made of dye-doped PMMA. In this section the fabrication process of the microresonators is explained and illustrated in Fig. 4.1. Detailed fabrication parameters can be found in [107, 157].

In the first step the laser dye PM597 is added at a concentration of 25 µmol/g PMMA to PMMA 950k which is dissolved in anisol. The solution is stirred for at least one day in order to ensure that the dye is dissolved properly. Then the

PMMA-dye solution is spin-coated on a silicon wafer, the standard layer thickness is approximately 1 µm. The sample is baked on a hot plate at 110 °C to ensure evaporation of remaining solvent. Afterwards electron beam (e-beam) or deep-UV lithography is used to pattern discs which will become the resonators [1]. As PMMA is a positive resist the area which will be removed later on is exposed to the e-beam or UV light (see Fig. 4.1 (a)). Subsequent development removes the exposed photoresist and yields discs lying on the silicon substrate (Fig. 4.1 (b)). As silicon has a higher refractive index than PMMA, the silicon beneath the PMMA discs has to be removed to obtain a light-guiding cavity. This is done by isotropic etching of silicon with XeF_2. A detailed description of the etching procedure can be found in [109]. After the etching step discs with free-standing rims are obtained which already exhibit Q-factors above 5×10^4 (see Fig. 4.1 (c)) [107]. The last step in the fabrication is an optional thermal reflow. The sample is placed on a hot plate for 30 s at a temperature of 125 °C. Since this temperature is above the glass transition temperature of PMMA (T_g = 105 °C) the surface of the PMMA is smoothened. Furthermore, stress, which has been induced between PMMA and silicon during the baking step after spin-coating, is released and the resonators obtain a goblet-like shape as illustrated in Fig. 4.1 (d). The resulting Q-factors of the goblet-cavities are one to two orders of magnitude higher than those of the disc resonators due to reduced scattering losses [107].

Compared to other types of resonators reported in literature the Q-factors of the polymeric goblets are approximately three orders of magnitude lower than those of silica spheres [110], but comparable to Q-factors achieved with replica-molded polymeric microtoroids [158]. However, either for silica resonators or replica-molded polymeric cavities a serial reflow step with a CO_2 laser is required (in the latter case for fabrication of the mold). In contrast to that the use of a hot plate is simpler and does not require focussing of the CO_2 laser onto each resonator. In conclusion, the presented fabrication process for polymeric resonators allows parallel fabrication and up-scaling.

4.3 Fluorol-doped WGM Cavities

An array of microgoblet resonators each functionalized with a different receptor is one way to realize a multiplexed sensor [83]. One method to distinguish between the signals originating from different resonators is the use of different laser dyes exhibiting different emission spectra. Since low-cost high-power laser diodes in the blue

[1] As long as not stated otherwise e-beam lithography was used in this work.

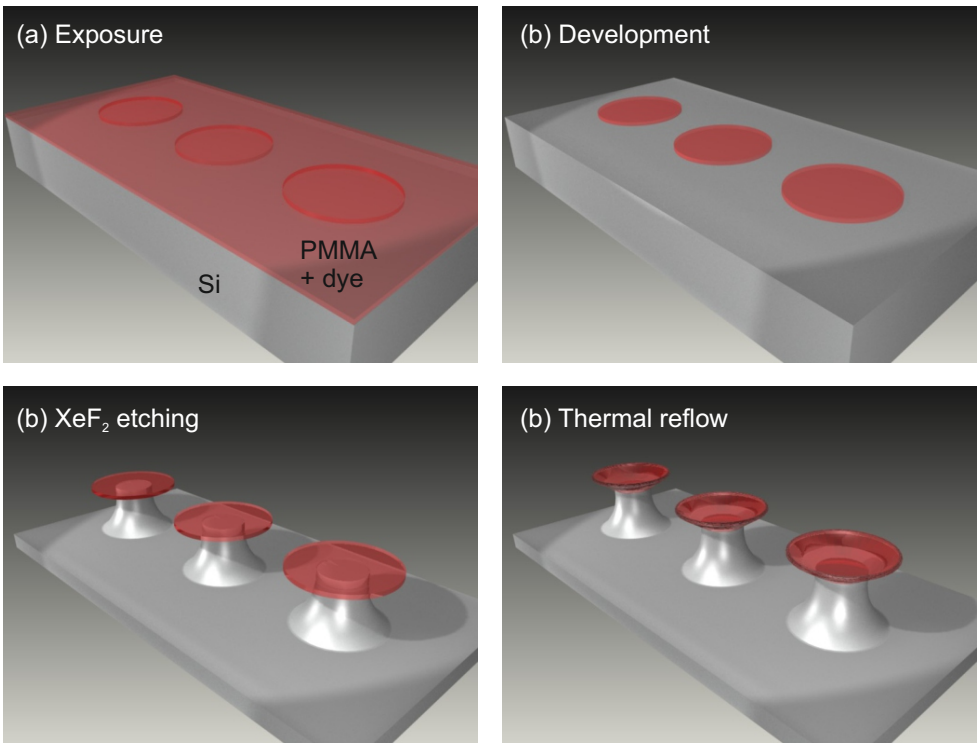

Figure 4.1: Fabrication of dye-doped polymeric cavities on silicon substrates. (a) Dye-doped PMMA is spin-coated on a silicon wafer and structured with e-beam lithography. (b) Development after exposure results in PMMA discs on silicon. (c) The silicon beneath the rim of the disc is removed by isotropic etching with XeF_2 resulting in disc resonators standing on silicon pedestals. (d) In a reflow step the sample is heated above the glass transition temperature of PMMA in order to smoothen the cavity surface. As stress is released the cavities transform into goblets. Adapted from [107].

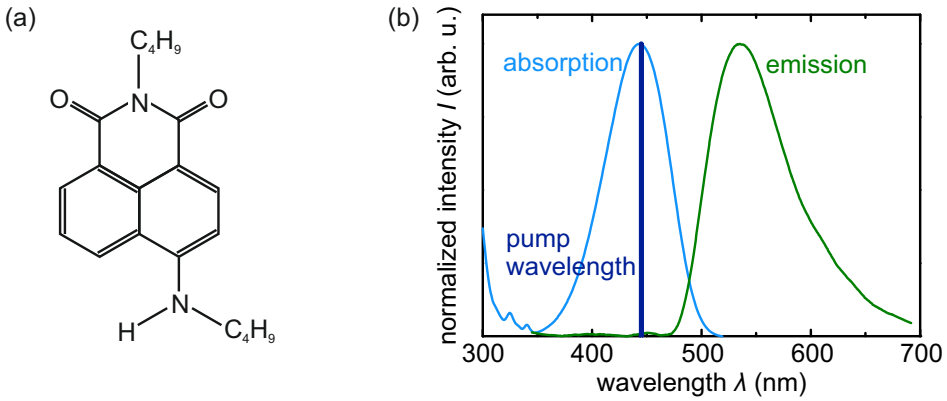

Figure 4.2: (a) Chemical structure of Fluorol 7GA adapted from [161]. (b) Absorption and emission spectra of Fluorol 7GA embedded into a PMMA matrix. The dye exhibits a Stokes shift of almost 100 nm preventing re-absorption of emitted photons. Adapted from [162].

wavelength regime are available the laser dye Fluorol 7GA, which has high absorption in this wavelength region, was chosen as an alternative emitter to PM597. In Fig. 4.2 the absorption and emission spectrum of Fluorol 7GA embedded in PMMA is shown. As pump source a laser diode with an emission wavelength of 445 nm can be used as it fits well to the absorption maximum of Fluorol 7GA. Fluorol 7GA exhibits a Stokes shift of almost 100 nm ensuring a low re-absorption of emitted photons. Furthermore, the dye exhibits a high photostability and a high quantum yield of $\Phi_f = 0.88 \pm 0.03$ in PMMA [159, 160].

First experiments on Fluorol 7GA-doped cavities were performed during the Diploma thesis of Jan Fischer [162] and a more detailed study was done in the Bachelor's thesis of Raphael Schmager [163].

In order to investigate the suitability of Fluorol 7GA-doped cavities as sensors resonators with different dye concentrations were fabricated according to the method presented in section 4.2. Besides PMMA 950k also the copolymer PMMA/MA 33% (AR-P 617, *Allresist*) was tested as cavity material. The copolymer is composed of methyl methacrylate and methacrylic acid and exhibtits a higher thermal stability than PMMA. The Fluorol 7GA-doped cavities were characterized regarding their lasing threshold in air and in water, their photostability of the lasing emission and their BRIS. As the absorption cross section of Fluorol 7GA is lower than for PM597 higher dye concentrations (35-250 µmol/g polymer) have been selected for Fluorol 7GA than for PM597 (25 µmol/g polymer). In Fig. 4.3 (a) an input-output curve is shown where the integrated intensity of the lasing mode appearing at the

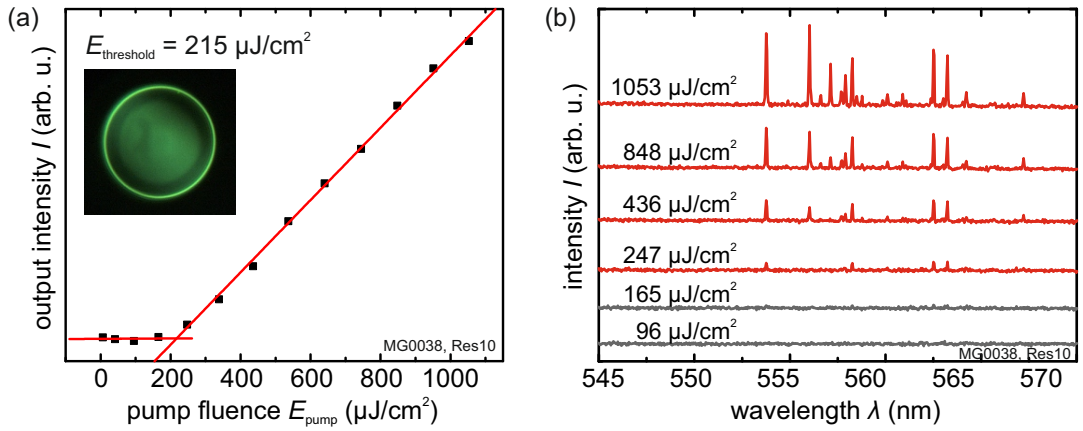

Figure 4.3: Lasing threshold of a Fluorol 7GA-doped polymeric microgoblet. (a) Input-output curve exhibiting a superlinear increase for a pump fluence exceeding 215 µJ/cm^2 per pulse. The low threshold allows optical pumping with a laser diode. (b) Emission spectra for different pump energies. Lasing peaks emerge when the threshold is overcome. Adapted from [163].

lowest energy is plotted versus the excitation energy for a copolymer resonator with a dye concentration of 40 µmol/g polymer. The kink in the curve marks the onset of lasing and the threshold is determined as the intersection of the two lines to be 215 µJ/cm^2 per pulse. The spectra taken at different pulse energies depicted in Fig. 4.3 (b) visualize the emerging lasing peaks. Samples with higher dye concentrations exhibit slightly higher thresholds [163]. This might be due to the formation of aggregates and quenching going along with it. PMMA resonators doped with comparable dye concentrations also exhibit higher thresholds. One explanation could be that the dye molecules are better integrated in the copolymer due to its different chemical structure. Compared to PM597-doped resonators the lasing threshold of Fluorol 7GA-doped cavities are approximately 5 times higher but still low enough that lasing modes can be excited with a simple laser diode.

As sensors often operate in aqueous environment the lasing threshold was also measured in water. There a pump fluence of 660 µJ/cm^2 was required to obtain lasing emission. The higher threshold in water compared to air is attributed to increased radiation losses in the cavity originating from the lower refractive index contrast between PMMA and water compared to air. Also for PM597-doped microgoblets the threshold in water is three times larger than in air [11].

To analyze the sensor performance the BRIS of Fluorol 7GA-doped cavities was measured. Therefore, the cavity was immersed in water–glycerol mixtures with different refractive indices and the shift of the lasing peaks $\Delta\lambda_0$ was measured in dependence

of the refractive index change of the surrounding Δn_{sur}. The slope of the curve represents the BRIS which is usually given in units of nm/RIU (refractive index units). Fig. 4.4 (a) shows two spectra taken during a BRIS measurement at different refractive indices clearly illustrating the shift of the lasing modes. In Fig. 4.4 (b) the shift $\Delta\lambda_0$ is plotted versus the refractive index change of the surrounding Δn_{sur} and the BRIS is determined to be 8 nm/RIU. This result is in the same order of magnitude as the BRIS of silica microspheres where a value of $S_{\mathrm{BRIS}} = 30\,\mathrm{nm/RIU}$ can be found in literature [76]. For PM597-doped microgoblets made of PMMA BRIS values between 16 and 23 nm/RIU [11, 164] have been measured. The lower wavelength of the lasing modes of the Fluorol 7GA-doped resonators compared to PM597-doped cavities directly leads to a lower BRIS (see Eq. 4.1) but it also influences the field distribution. For smaller wavelength the overlap of the modes with the surrounding decreases further lowering the BIRS. Additionally, the shape of the goblet cannot be precisely controlled so a slightly different geometery can also contribute to a lower BRIS value.

The lasing emission of Fluorol 7GA-doped cavities in aqueous environment is stable for approximately 5×10^5 pulses. This corresponds to a measurement time of 40 minutes when a pump rate of 20 Hz is used. For comparison the stability of PM597-doped cavities is higher, even after 2×10^6 pump pulses lasing modes are observed [11]. Still, a lifetime of 40 minutes is sufficient to perform sensing experiments.

To conclude, Fluorol 7GA-doped cavities show low lasing thresholds in air and in aqueous environment enabling excitation with a low-cost laser diode. These cavities are suitable as sensors as they react to changes in the environment and their lasing emission is stable for 40 minutes.

4.4 All-Polymeric Resonator Sensor Chips

For lab-on-a-chip applications disposable sensors are desirable to prevent, e.g., contamination or elaborated cleaning procedures. Hence, material and fabrication costs of the sensor should be low. For this reason a modified fabrication process for all-polymeric resonators was developed in close collaboration with the Institute of Microstructure Technology (IMT, KIT). The results presented in this section were published in [82]. By introducing an additional polymer layer between substrate and PMMA later serving as pedestal material, fabrication of all-polymeric resonators on different substrates than silicon is possible.

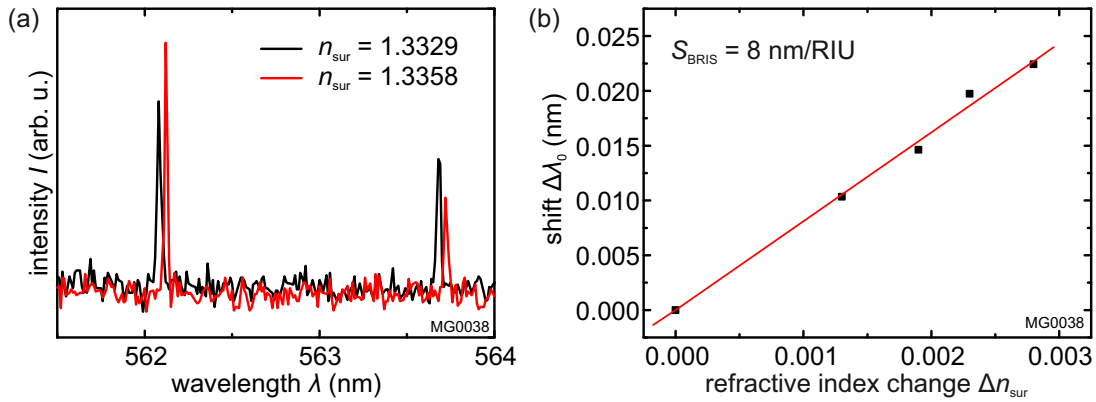

Figure 4.4: Bulk refractive index sensitivity of Fluorol 7GA-doped resonators. (a) The lasing peaks experience a shift when the refractive index of the surrounding medium is changed. (b) The shift of the lasing modes $\Delta\lambda_0$ is measured for different water–glycerol mixtures and plotted over the refractive index change Δn_{sur}. The slope of this curve represents the bulk refractive index sensitivity S_{BRIS}.

We have chosen a lift-off resist (LOR) as pedestal material since it allows selective removal of the PMMA and is thermally stable during the thermal reflow. The fabrication process is schematically depicted in Fig. 4.5. First, LOR is spin-coated on the substrate with an approximate thickness of 5 µm. Then a 1.2 µm thick dye-doped PMMA layer is spin-coated on top and the sample is baked on a hot-plate to remove residual solvents. The detailed fabrication parameters can be found in [82, 165]. Patterning of the PMMA is done with a mask aligner via deep-UV lithography. After development of the PMMA layer wet etching is used to remove the LOR beneath the rim of the PMMA in order to obtain light-guiding discs. Finally a thermal reflow at 130 °C to 135 °C is performed to smoothen the resonator surface. During this step the discs are converted into goblets. Compared to the standard fabrication process presented in section 4.2 the use of a variety of substrates is possible with the modified process since no selective isotropic etching of the substrate is required. The use of deep-UV lithography enables parallel fabrication and does not require electrically conductive substrates. Furthermore, no vacuum based dry etching with toxic XeF_2 is required.

We have chosen polysulfone (PSU) as polymeric substrate since its glass transition temperature of $T_g = 195\,°C$ provides thermal stability during the thermal reflow. In cooperation with the company *Microfluidic ChipShop GmbH* (Jena, Germany) resonator fields of 10×10 resonators have been integrated into a polymeric microfluidic chip with the size of standard microscope slides and integrated inlet and outlet ports for simple injection of fluids. The high transparency of the chip enables free-space

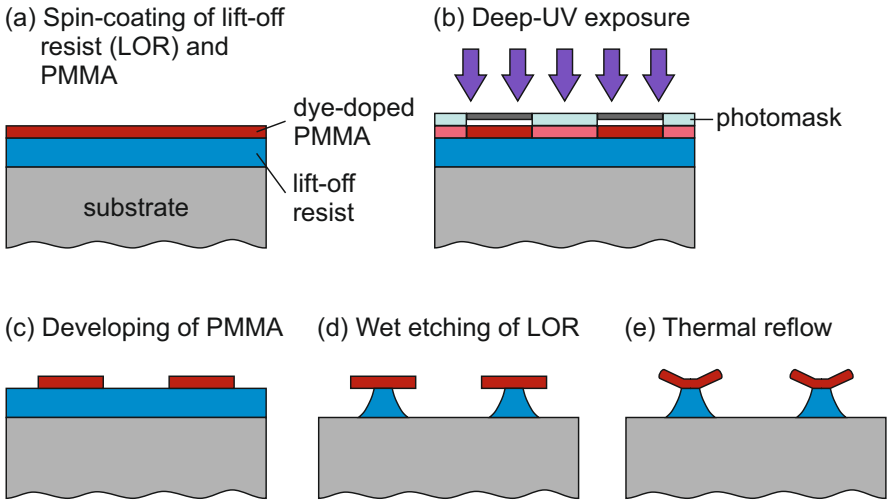

Figure 4.5: Fabrication of dye-doped polymeric cavities with polymeric pedestal. (a) The lift-off resist (LOR) and dye-doped PMMA are spin-coated on a substrate. (b) A photomask and deep-UV lithography are used to pattern the structures. (c) Developing of the PMMA and (d) isotropic wet etching of the LOR results in disc cavities. (e) A thermal reflow is applied to smoothen the cavity surface. As stress is released the cavity discs transform into goblets. Adapted from [82].

excitation and read-out. In Fig. 4.6 an image of the resonators integrated into the chip as well as SEM images of a resonator field and a single resonator are shown.

For optical characterization of the all-polymeric resonators we performed measurements of Q-factors and lasing thresholds. Q-factors were investigated for resonators on silicon substrates structured with e-beam and deep-UV lithography and for resonators on PSU substrates structured with deep-UV lithography. For all resonator types comparable Q-factors in the order of 10^5 were measured. We conclude that deep-UV lithography works as good as e-beam lithography when considering the Q-factors of the resonators. Measurements of the lasing thresholds were conducted with the setup presented in section 4.2 where the pump laser has been replaced by a laser diode emitting pulses of approximately 25 ns at 520 nm. In Fig. 4.7 a typical threshold curve for an on-chip resonator in air is depicted. The threshold is as low as 45 µJ/cm^2 per pulse which corresponds to 0.5 nJ per pulse and resonator and is in good agreement with values of resonators fabricated on silicon pedestals [11]. In water lasing thresholds increased due to higher radiation losses but usually stayed below 240 µJ/cm^2 per pulse, enabling optical pumping with the laser diode also during sensing experiments. In order to demonstrate the suitability of the all-polymeric resonator chips for sensing experiments BRIS measurements have been performed.

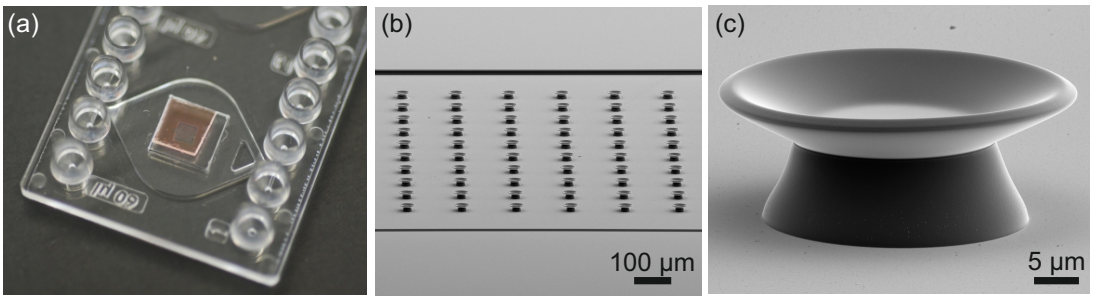

Figure 4.6: (a) Photograph of an array of all-polymeric resonators integrated in a polymer microfluidic chip. (b) and (c) SEM images of an array of 100 resonators and a single resonator with polymeric pedestal. Adapted from [82].

A peristaltic pump was used to fill the fluidic chamber around the resonators with solutions of different refractive indices. The spectral positions of the lasing peaks were tracked over time. Plotting the resulting shifts over the change in refractive index yields BRIS values of $S_{\mathrm{BRIS}} \approx 11\,\mathrm{nm/RIU}$ for all-polymeric resonators (compare Fig. 4.7).

In summary, fabrication of all-polymeric resonators via deep-UV lithography allows the use of different substrates and parallel fabrication while maintaining high Q-factors and low lasing thresholds. The dye-doped microgoblets can be integrated into fluidic chips and their sensing ability was demonstrated with BRIS measurements.

4.5 Summary and Conclusions

In this chapter the sensing properties and different implementations of WGM cavities have been discussed. In literature silica spheres and toroids are frequently studied. Much effort has been spent in improving the detection limit of WGM cavities. This was done by either improving the resolution, i.e., by lowering the noise level or by increasing the sensitivity, i.e., magnifying the shift caused by molecules. Frequency-locking, measurements on mode-splitting or linewidth-broadening are examples for the first method while enhancing the electric field by deposition of plasmonic nanoparticles is an example for the latter. Successful detection of single exosomes, viruses and even proteins has been demonstrated [9, 10, 139, 148]. However, fragile tapered fibers are commonly used to excite the modes in the cavities requiring sophisticated equipment for alignment. Concerning applications outside the laboratory environment realization of these approaches is difficult.

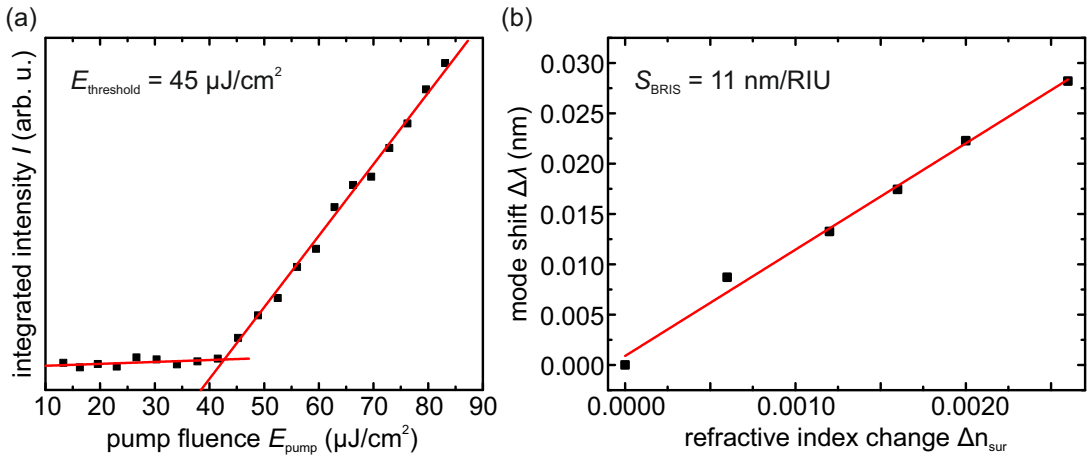

Figure 4.7: (a) Input-output curve of a resonator with polymer pedestal on a PSU substrate. The low lasing threshold enables pumping with a laser diode. (b) Resulting shifts $\Delta\lambda$ of the lasing modes when the cavity was immersed in solutions with different refractive indices plotted versus the change in refractive index Δn_{sur}. The slope of the curve yields a BRIS of $S_{\mathrm{BRIS}} = 11\,\mathrm{nm/RIU}$. Adapted from [82].

Therefore, in this work polymeric microlasers which can be excited and read out via free-space optics were investigated, making tapered fibers redundant. Furthermore, parallel and thus scalable fabrication of dye-doped polymeric microdiscs or -goblets is possible in contrast to fabrication of silica resonators where the reflow process is serial.

The use of a polymeric host material offers the possibility to integrate different gain materials so the optical properties such as the pump and emission wavelength can be tuned. During this work the laser dye Fluorol 7GA has been successfully integrated into WGM cavities. A characterization regarding lasing threshold, BRIS and operational lifetime shows that these cavities are suitable as sensors which can be pumped with a low-cost laser diode, although their performance is not as good as for PM597-doped cavities.

Furthermore, in collaboration with the IMT, we developed a modified fabrication process for resonators with polymeric pedestals which can be fabricated on a variety of substrates. Resonators on polymeric substrates (PSU) exhibit low lasing thresholds comparable to the ones of their counterparts on silicon. In cooperation with the industrial company *Microfluidic ChipShop* an all-polymeric chip with an array of 100 resonators integrated into a fluidic chamber was fabricated and BRIS measurements were conducted to demonstrate the sensing ability.

The presented results show that the use of cavities with lasing emission simplifies operability and that polymeric resonators are flexible regarding emitter and substrate. As the detection limit is an important figure of merit for sensors different methods on enhancing the sensitivity of WGM microlasers will be presented in the next chapter.

Chapter 5

Whispering Gallery Mode Lasers with Enhanced Sensitivity

As already discussed previously the detection limit of a sensor is an important figure of merit. At the beginning of this chapter influences on the detection limit of WGM lasers will be discussed. Afterwards different methods to improve the detection limit will be presented: Resonators which have been coated with a high-refractive index layer and resonators of varying radii and thicknesses. In the end the different concepts implemented to enhance the sensitivity are compared.

5.1 Detection Limit of WGM Lasers

The detection limit DL represents the lowest amount (protein concentration, mass density on a surface, change of refractive index,...) of change in the surrounding which can reliably be detected with a sensor. It can be calculated as the ratio of the resolution of the system R to the sensitivity towards the occurring change S. In the following the dependence of the resolution of WGM cavities on the used measurement technique is discussed and the sensitivity used to characterize the cavities is introduced.

Resolution
The resolution R denotes the minimum resolvable shift and is commonly defined as $R = 3\sigma$, where σ describes the total noise variance. Three main contributions to the total noise can be distinguished: amplitude noise, thermal noise and the spectral resolution of the system [16].

Thermal noise influences the spectral position of the resonant mode and mainly depends on the properties of the cavity material. The thermo-optic coefficient $\kappa = dn/dT$ and the expansion coefficient α change the optical path length of the cavity upon temperature changes. By using a temperature stabilization thermal noise can be minimized.

The spectral resolution depends on how precisely the spectral position of the resonant mode can be determined. Hence, the complete system which is used to acquire the data has to be considered. For passive cavities the linewidth of the tunable laser may limit the spectral resolution but as the linewidth is usually in the range of few femtometers or less this is negligible compared to amplitude noise or thermal noise. In contrast to that, for the read-out of WGM lasers usually a spectrometer with a limited resolution is used, and this often represents the bottleneck in the total resolution.

Amplitude noise refers to fluctuations which are added to the amplitude of the signal. Sources for this are, e.g., shot noise and thermal noise of the photodetector or amplitude fluctuations of the laser [16]. By using Monte Carlo simulations White *et al.* showed that amplitude noise is proportional to the linewidth of the resonant mode [16]. In their calculation they assumed that the resonant modes are excited with a tunable laser which is guided through a tapered fiber and the detection of the transmitted light is done with a photodiode.

Since for WGM lasers free-space excitation and detection with a spectrometer is used the acquired data differs from data obtained with fiber excitation. The main differences are the lower sampling rate regarding the wavelength and the fact that amplitude noise of the excitation laser only plays a minor role. To obtain information on the noise caused by the limited resolution of the spectrometer and by amplitude noise of the system, the Monte Carlo simulations proposed by White *et al.* were adapted to the WGM lasers and the setup used in this work. In the following, the procedure of the Monte Carlo simulations is presented. The parameters were adapted to the setup described in section 3.3.1 when the 2400 lines/mm grating was used.

For data analysis the spectral position of the lasing modes is extracted from the spectrum by fitting a peak function to the data (see Fig. 5.1). Both, a Lorentzian and a Gaussian function can be used to determine the peak position and both yield comparable results. However, especially when the peak height is small the Gaussian function represents the data points better, so as long as not mentioned otherwise a Gaussian function is used. For Monte Carlo simulations spectra with a Gaussian

Table 5.1: Parameters for the Monte Carlo simulation to obtain a value of the noise from the limited spectral resolution of the spectrometer in combination with amplitude noise.

Parameter	value
spectral distance between consecutive data points	0.01 nm
noise amplitude of amplitude noise in spectrum	11 counts
number of data points	30
number of runs	100000

peak were generated with MATLAB from *MathWorks*®:

$$I(\lambda) = h \cdot \exp\left(-\frac{(\lambda - \lambda_0)^2}{2\sigma^2_{\text{Gauss}}}\right). \tag{5.1}$$

Here, h represents the height of the peak above background, λ_0 is the wavelength of the resonant mode and σ_{Gauss} is the width of the peak. In the following the full width at half maximum $\delta\lambda_{\text{Gauss}} = 2\sqrt{2\ln 2}\sigma_{\text{Gauss}}$ of the peak is used and referred to as linewidth of the Gaussian peak. The spectral distance between two consecutive data points was adapted to be the same as in the experiments. Amplitude noise with a Gaussian distribution was added to the ideal generated Gaussian peak, the noise amplitude was determined from a measured spectrum. Afterwards the noisy data was fitted with a Gaussian function and the center wavelength of the peak was extracted. Repeating this procedure multiple times yields the standard deviation of the center wavelength σ_{λ_0} which corresponds to the noise of the system.

The simulation was performed for different linewidths of the generated Gaussian peak $\delta\lambda_{\text{Gauss}}$ and for different peak heights h. Other fixed parameters of the simulation are listed in Table 5.1. The simulation results depicted in Fig. 5.1 clearly show that the standard deviation of the center wavelength σ_{λ_0} decreases with decreasing linewidth of the generated Gaussian peak $\delta\lambda_{\text{Gauss}}$. Also an increasing peak height which corresponds to an improved signal to noise ratio improves the precision. The results are in good agreement with the results obtained by White *et al* [16]. Fig. 5.1 (c) shows the resulting standard deviation of the center wavelength for a linewidth of the generated Gaussian peak of $\delta\lambda_{\text{Gauss}} = 0.033\,\text{nm}$ which is the typical experimental value for the setup configuration described above.

Since the detection path beam in the µ-PL setup (see section 3.3.1) is perpendicular to the resonator plane only light which is scattered from the cavity, e.g., through scattering at surface imperfections of the resonator, can reach the spectrometer. Hence, the height of the lasing peaks with respect to the fluorescence background depends on the presence of scattering centers and on their position with respect to

the entrance slit of the spectrometer. To improve the free-space read-out efficiency circular micromirrors which are placed around the cavities were developed during the PhD thesis of Tobias Wienhold in collaboration with our group [166]. The micromirrors redirect the light originating from radiation loss channels, which is emitted in the plane of the cavity, to the spectrometer. With this approach the ratio of the peak height to the fluorescence background could be improved by a factor of eleven in air. In aqueous environment the effect could be even higher due to increased radiation losses. Thus, circular micromirrors are also one method to improve the resolution.

For the experiments conducted in this work only scattered light has been detected and hence the height of the lasing peaks varies for different resonators. Typically the lasing peaks are at least 200 counts higher than the fluorescence background yielding a noise for the determination of the peak position of $\sigma_{\lambda_0} = 0.71\,\mathrm{pm}$. For peak heights of 500 counts above background the noise would even reduce to $\sigma_{\lambda_0} = 0.28\,\mathrm{pm}$ meaning that higher peaks are beneficial for the resolution.

For microdiscs made of PMMA with a radius of 25 µm the temperature dependence of the modes was determined to be $d\lambda_0/dT \approx -29\,\mathrm{pm/K}$ in water [167]. Assuming that temperature can be controlled with a precision of $\Delta T = 0.1\,\mathrm{K}$ this yields a temperature noise of $\sigma_{\mathrm{temp}} = 2.9\,\mathrm{pm}$. So thermal noise exceeds the noise from setup and analysis by a factor of 4 (10) when a peak height of 200 (500) counts above background is assumed. Obviously thermal noise is the main factor limiting the resolution. For the overall resolution R all noise sources have to be taken into account [16]:

$$\sigma = \sqrt{\sigma_{\lambda_0}^2 + \sigma_{\mathrm{temp}}^2}. \tag{5.2}$$

This yields a resolution of $R = 3\sigma = 8.7\,\mathrm{pm}$ or $R = 8.4\,\mathrm{pm}$ for peak heights of 200 counts or 500 counts, respectively.

In order to minimize influences from thermal noise our collaborators at the Institute of Microstructure Technology (IMT, KIT) developed a referencing scheme [167]. One so-called "reference" resonator is embedded in a polymeric glue, inhibiting interactions of the evanescent field with the surrounding. During a sensing experiment the signal from both an actual sensing resonator and a reference resonator is acquired and subtracted. Since the signal resonator is sensitive to the actual change in environment and disturbances from temperature fluctuations and the reference resonator only detects temperature changes this method allows to minimize disturbing thermal influences. Furthermore, also the blue-shift of the lasing peaks originating from bleaching of dye molecules can be corrected with this referencing technique [167].

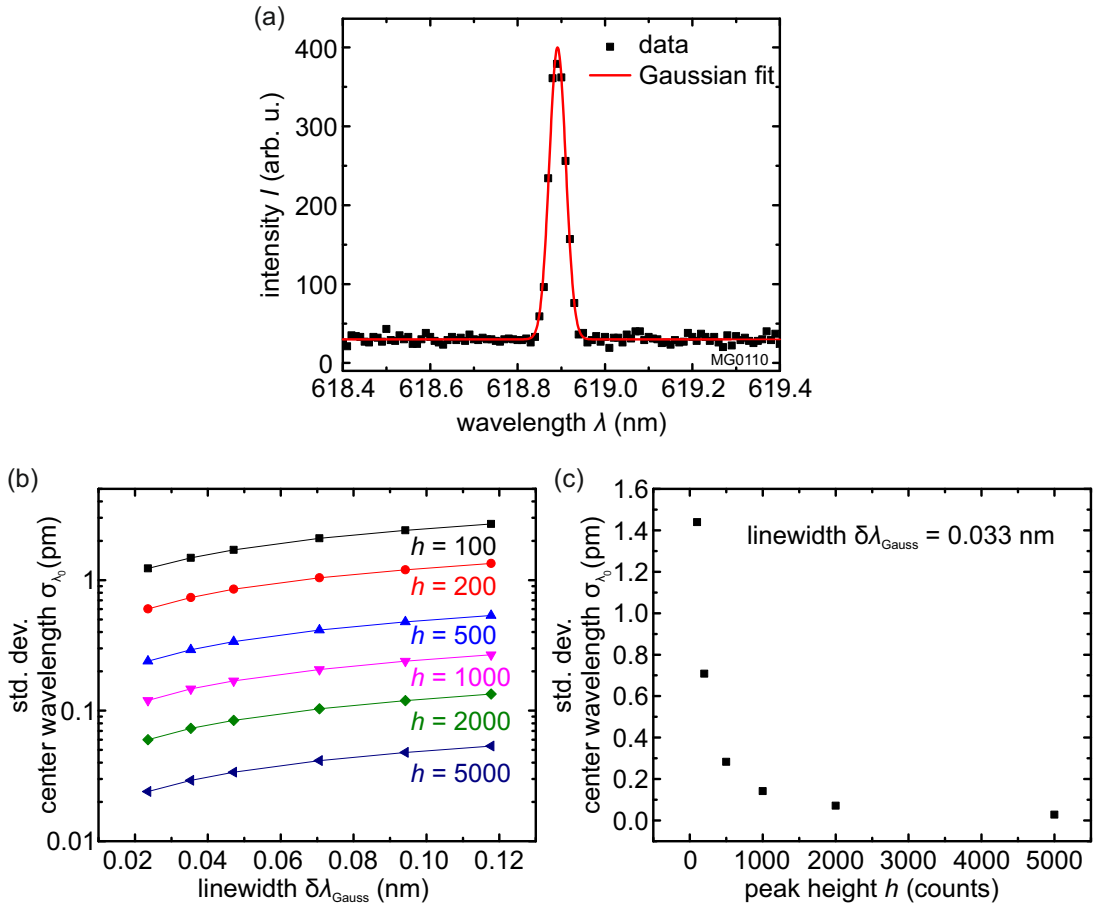

Figure 5.1: Influence of the linewidth $\delta\lambda_{\mathrm{Gauss}}$ and peak height h on the resolution R. (a) Typical lasing peak in the spectrum of the WGM resonators with the Gaussian curve fitted to the data points. (b) The resulting standard deviation of the center wavelength σ_{λ_0} for different peak heights and linewidths of the generated Gaussian peaks. (c) Standard deviation of the center wavelength σ_{λ_0} for the typical linewidth $\delta\lambda_{\mathrm{Gauss}}$ in the conducted experiments and varying peak height h.

Sensitivity of WGM resonators

A particularly important sensitivity is the bulk refractive index sensitivity (BRIS) which has already been briefly introduced in the previous chapter. It describes how the sensor reacts towards changes in the refractive index of the surrounding. The BRIS is proportional to the fraction of light energy of the mode in the surrounding η_{sur} [16]. During this work the BRIS was used to evaluate the sensor performance for the following reasons:

- The shift $\Delta\lambda_0$ caused by attaching molecules is proportional to the BRIS (see section 4.1.1 and [136]), as long as the field at the resonator surface is homogeneous and no local hotspots are formed as it is the case for attached plasmonic particles [139].
- The BRIS is independent of functionalization schemes which are applied to make the resonators sensitive towards certain biomolecules, i.e., the BRIS is reliable and stable over time.
- An important advantage of the WGM lasers, which can be excited and read-out via free-space optics is that the conduction of BRIS measurements is simple.

For BRIS measurements the WGM lasers are placed in a sample chamber which is integrated in the µ-PL setup described in section 3.3.1. Lasing spectra of the WGM resonators are acquired continuously while the sample chamber is filled with water–glycerol mixtures of different refractive indices. Fig. 5.2 depicts the result from a typical BRIS measurement. In Fig. 5.2 (a) the shift of a lasing mode is monitored over time showing a step-like red-shift when a solution with higher refractive index is filled into the chamber. After each step the chamber was filled with water to obtain a baseline. To determine the BRIS the wavelength shifts $\Delta\lambda_0$ are plotted versus the refractive index change of the surrounding Δn_{sur} and the BRIS S_{BRIS} is obtained as the slope of a linear regression which is fitted to the data points.

Detection Limit of WGM Lasers

When transferring the considerations above to the detection limit we can see that it is low for resonators with high quality factors Q (i.e., small linewdith) and modes with high overlap with the surrounding η_{sur}

$$DL = \frac{R}{S} \propto \frac{1}{Q\eta_{\mathrm{sur}}}. \tag{5.3}$$

This equation is valid when thermal noise is neglected and a high resolution is assumed [11]. Since an increase of the field overlap with the surrounding η_{sur} (and

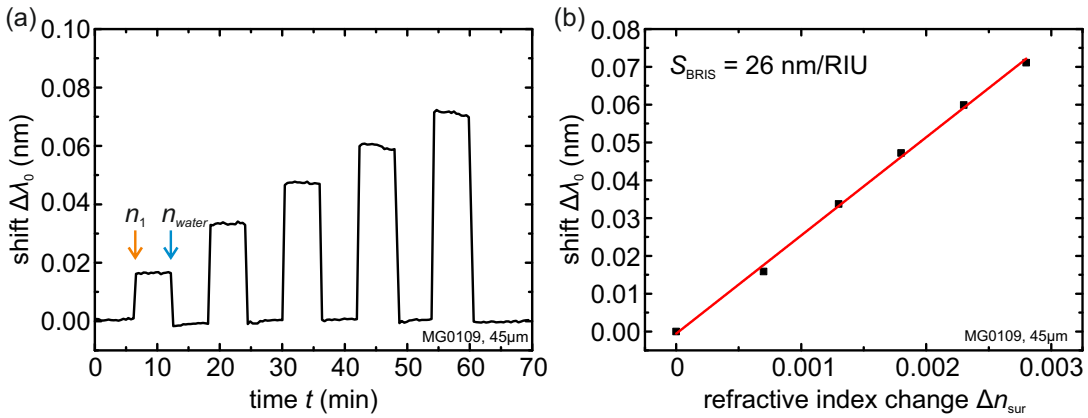

Figure 5.2: Results of a typical BRIS measurement. (a) The lasing modes exhibit an immediate red-shift when the refractive index of the surrounding changes to a higher value (orange arrow). Between the solutions with the different refractive indices water is filled into the sample (blue arrow) chamber to obtain a baseline. (b) When the wavelength shift $\Delta\lambda_0$ is plotted in dependence of the refractive index change Δn_{sur} the slope of the linear regression yields the BRIS S_{BRIS}. Adapted from [168] and [169].

hence an increase in the sensitivity) usually goes along with a decrease of the Q-factor [16], these two quantities cannot be optimized independently, so the product $Q \cdot \eta_{\mathrm{sur}}$ needs to be maximized to yield a low detection limit.

For WGM lasers usually the spectrometer limits the resolution and the actual linewidth of the lasing modes is much narrower. The absolute limit of the linewidth of a laser $\delta\omega_{\mathrm{osz}}$ was deduced by Schawlow and Townes [170]:

$$\delta\omega_{\mathrm{osz}} = \frac{2\hbar(\delta\omega_0)^2}{P} = \frac{2\hbar\omega_0^3}{PQ^2}. \tag{5.4}$$

Here, P denotes the power in the oscillating field and $\delta\omega_0$ the linewidth of the cavity. In high-Q silica toroids Yang *et al.* observed lasing linewidth down to 4 Hz which is close to the Schawlow-Townes limit [171]. The narrow linewidth of the lasing peaks also has an impact on the resolution and the detection limit. While for passive cavities an increased sensitivity would lead to a broader measurable linewidth and thus increased amplitude noise, for WGM lasers the total resolution stays the same as the broadening of the linewidth (corresponding to a decrease of the Q-factor) is not measurable by the system. This circumstance is visualized is Fig. 5.3.

Hence, for WGM lasers which are read out with a spectrometer the detection limit can be improved by enhancing the field overlap of the modes with the surrounding leading to increased sensitivities. This can be realized with different approaches:

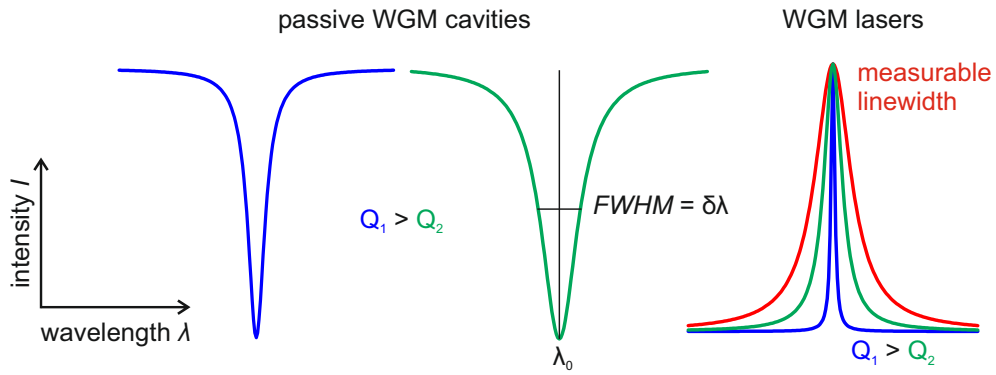

Figure 5.3: Comparison of the linewidth of passive and active resonators for different Q-factors. For active resonators the measurable linewidth is usually limited by the resolution of the spectrometer so a broadening due to a lower Q-factor will not be measurable. Hence, the total resolution will not suffer from lower Q-factors as long as the linewidth of the lasing mode stays below the measurable linewidth.

- **Coupling of resonators:** When two WGM resonators are brought closely together so that the evanescent fields of the modes overlap, so-called supermodes form which extend over both cavities [172]. In analogy to the hydrogen molecule a bonding and an anti-bonding mode develop, the former exhibiting a field enhancement in the coupling gap which leads to an increased sensitivity [173, 174]. In previous work T. Großmann fabricated coupled WGM resonators and measured a BRIS which was enhanced by a factor of three compared to single disc resonators [11].

- **Coating resonators with a high refractive index layer:** When resonators are coated with a material which exhibits a higher refractive index than the cavity itself, the resonant modes can be mainly guided inside this coating as soon as its thickness is large enough. Hence, the maximum of the modes is closer to the rim of the cavity and the evanescent field outside the cavity is enhanced [175]. U. Bog demonstrated that with a high-refractive polymer (poly(p-xylylene)) coating the sensitivity of PMMA microgoblets can be enhanced by 54% [176]. In this work microgoblet resonators were coated with TiO_2, which is expected to yield even higher improvements than the high-refractive polymer due to its higher refractive index.

- **Optimizing the size of the resonators:** The dimensions of the resonator, its radius and its thickness, also influence the field distribution and thus the overlap of the mode with the surrounding. By optimizing the radius and the thickness of the cavity the sensitivity can be enhanced which was shown in the course of this work.

5.2 Resonators with High Refractive Index Coating Layer

In order to increase the sensitivity of WGM cavities the mode overlap with the surrounding η_{sur} needs to be enhanced. One method is the deposition of a high refractive index coating layer on top of the resonator to "pull" the mode further towards the cavity rim. As coating material titanium dioxide (TiO_2) is suitable due to its high refractive index of $n_{TiO_2} \approx 2.3$ at wavelengths around 600 nm. Before goblet-shaped cavities with TiO_2 coating layer were fabricated finite element simulations were performed to make predictions on the sensitivity and the optimum coating thickness. In this section a brief introduction to finite element simulations is given. Then the theoretical and experimental results for TiO_2-coated resonators are presented and compared. The results of this section were obtained during the Master's thesis of Fabian Ruf where further details on the performed simulations are given [164].

5.2.1 Finite Element Simulations of WGMs

In order to calculate the resonance frequency and the field distribution of resonant modes of the WGM cavities simulations based on the finite element method (FEM) were performed. This simulation method is a frequency domain eigensolver that determines solutions of Maxwell's equations on the computational domain for the given geometry and material of the cavity.

By using a time-harmonic ansatz for electromagnetic waves,

$$\mathbf{E}(\mathbf{r}, t) = \mathbf{E}(\mathbf{r})\mathrm{e}^{-i\omega t}, \tag{5.5}$$

Maxwell's equations can be reduced to an eigenvalue problem which connects the time-independent field distribution $\mathbf{E}(\mathbf{r})$ to the corresponding eigenfrequency ω [177]

$$\epsilon^{-1}\nabla \times \mu^{-1}\nabla \times \mathbf{E} - \omega^2\mathbf{E} = 0. \tag{5.6}$$

The finite element method divides the computational domain into small patches, usually triangles in 2D and tetrahedrons in 3D. The approximated electric field is then a superposition of local ansatz functions inside these patches.

A full 3D simulation of resonators with dimensions of hundreds of wavelengths requires high computational resources. To reduce computational effort the rotational symmetry of the resonator is exploited and cylindrical coordinates are used reducing the problem to two dimensions. The geometry of the goblet-shaped resonators is

obtained from a sample which was cut in the middle with a focused ion beam and then imaged with a scanning electron microscope. In Fig. 5.4 the cross section of a TiO_2-coated microgoblet and the derived geometry used for FEM simulations are shown. Furthermore, the division of the computational area into triangles is visualized – this mesh is adaptively refined during the simulation. The left boundary is the rotation axis while for the other boundaries perfectly matched layers (PMLs) are used. The PMLs allow implementation of transparent boundary conditions and avoid artefacts in the simulation which might result from, e.g., back-reflections of energy.

In this work the software JCMSuite from *JCMwave* was used to perform simulations. More details on FEM simulations performed with JCMSuite can be found in [95,164].

5.2.2 Optimization of the Layer Thickness

In order to determine the optimum layer thickness of the TiO_2 coating layer FEM simulations were used to calculate the filling factor of the mode with the surrounding η_{sur} which is proportional to the BRIS [136]. The filling factor is given as the fractional energy of the mode in one material divided by the total energy [178]:

$$\eta_\Omega = \frac{\int_\Omega \epsilon(\mathbf{r})|\mathbf{E}(\mathbf{r})|^2 dV}{\int_{V_{\mathrm{total}}} \epsilon(\mathbf{r})|\mathbf{E}(\mathbf{r})|^2 dV} \tag{5.7}$$

Here, $\epsilon(\mathbf{r})$ denotes the dielectric function. With FEM simulations the filling factors of a $TM_{0,0}$ mode with the resonator material (PMMA), the TiO_2 coating layer, and the surrounding medium (H_2O) were determined for different TiO_2 layer thicknesses. An inhomogeneous coating thickness on top and at the bottom of the cavity originating from the deposition method of the TiO_2 has been considered in the simulations. In Fig. 5.5 the simulation results are depicted for varying thickness of the TiO_2 coating layer. For thin coating layers the mode is mainly localized in the PMMA as can be seen from the filling factors (a) and the energy density distribution (b). For a layer thickness exceeding 35 nm the mode is mainly localized in the TiO_2 coating layer which acts as a potential well for photons escaping the cavity [175]. The maximum filling factor in the surrounding is achieved for a coating thickness of $t \approx 35\,\mathrm{nm}$. At this point the mode has just moved to the TiO_2 layer meaning that the maximum field intensity of the mode is close to the rim of the cavity. This leads to a high evanescent field outside the cavity. For a further increase of the coating

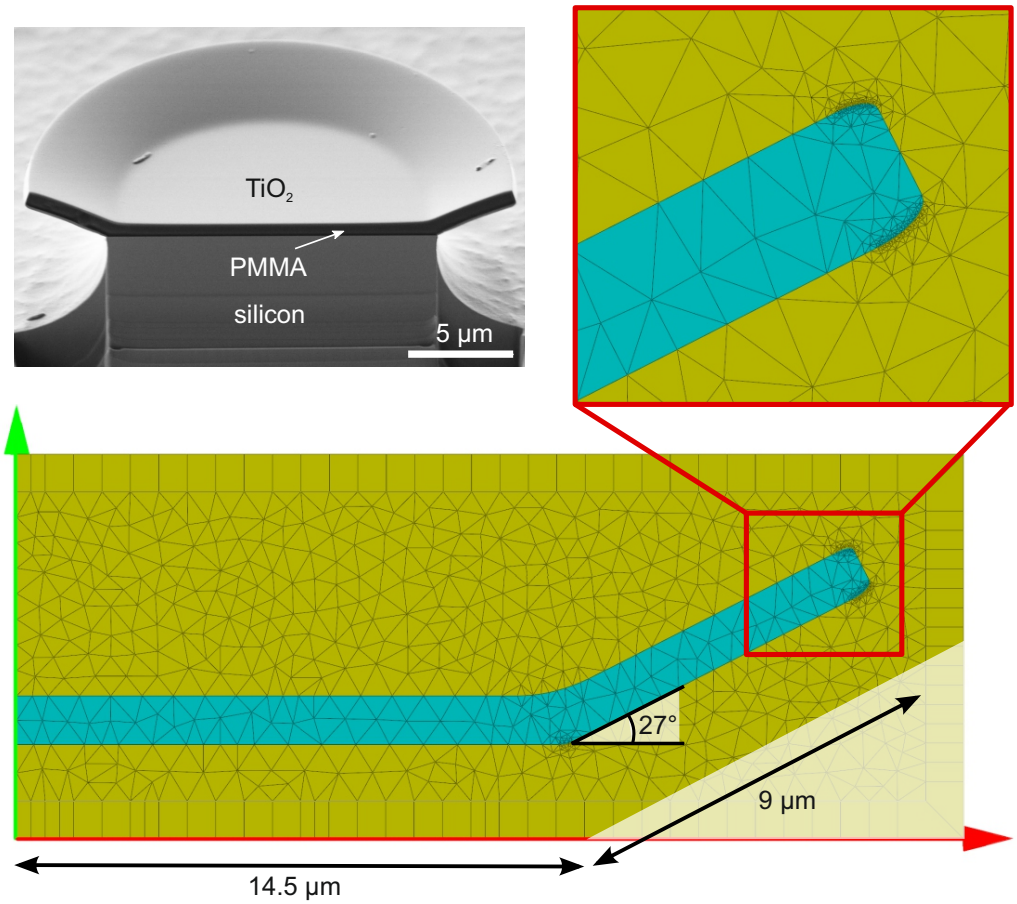

Figure 5.4: Geometry of the resonator used for FEM simulations. The cross section of a TiO_2-coated resonator is obtained from a SEM image after the resonator was cut with a focussed ion beam. The lower part shows the cross section used for FEM simulations. The left boundary is the rotation axis. For the other boundaries perfectly matched layers are used. The inset shows the rim of the goblet and the triangular mesh at the beginning of the simulation. Adapted from [164].

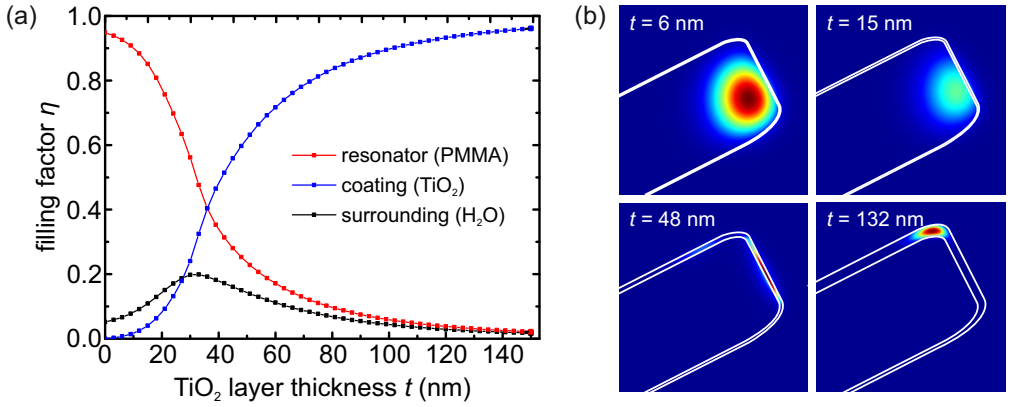

Figure 5.5: (a) Filling factor of a $TM_{0,0}$ mode with the resonator material (PMMA, red), the coating layer (TiO_2, blue) and the surrounding (H_2O, black). For a TiO_2 layer thickness t of approximately 35 nm the overlap with the surrounding reaches its maximum. (b) Energy density distribution for different TiO_2 layer thickness t. The mode is mainly localized in the high refractive coating layer for thickness exceeding 35 nm. Adapted from [164].

layer thickness the distance between the maximum of the energy density and the cavity rim increases again leading to a lower filling factor in the surrounding.

Goblet-shaped microcavities doped with PM597 were fabricated according to the process described in section 4.2. TiO_2 coating layers were deposited using ion beam sputtering deposition. Tilting of the sample holder enables the deposition of TiO_2 also at the bottom of the resonator. The layer thickness and the refractive index of TiO_2 were determined on a flat layer with ellipsometry. The deposition was done by Dr. Christoph Vannahme and Kristian Sørensen at the Technical University of Denmark (DTU).

As the BRIS is the experimentally accessible quantity FEM simulations of the BRIS were performed. The strategy for simulations is the same as in experiments. The resonant wavelength λ_0 is determined for different refractive indices n_{sur} of the surrounding and the wavelength shift $\Delta\lambda_0$ is plotted versus the refractive index change Δn_{sur} – the slope of a linear regression yields the BRIS.

In experiments the BRIS of the same resonators was measured before and after deposition of the TiO_2 coating layer to ensure a better comparability. In Fig. 5.6 (a) both simulation results for the fundamental TE and TM mode and experimental results on the BRIS are shown. Qualitatively the measured values agree well with the predictions from simulations. However, quantitatively higher BRIS values were expected from simulations even for resonators without TiO_2 coating. Deviations are likely due to variations in the geometry of the resonators.

To minimize the influence of the shape of the goblet resonators an enhancement factor comparing the BRIS values without and with TiO_2 coating was calculated. These values show a better agreement between simulations and experiment but still the experimental improvement of the sensitivity by a factor of 2.4 is lower than the one expected from simulations which is 3.5. One reason for the deviation might be the inhomogenity of the TiO_2 layer. The thickness of the TiO_2 layer is measured on a flat substrate so the thickness on top of the goblet resonator might be different. Also the ratio between coating thickness on top and bottom of the resonator might be different as assumed in the simulations. The thickness distribution for simulations was obtained from SEM images of a resonator with a TiO_2 layer of approximately 100 nm which was cut with a focused ion beam. However, for thinner layers the distribution might be different and thickness determination from SEM images was not possible.

For the resonators with a TiO_2 layer of 37 nm measurements on the lasing threshold in air and water were conducted. Lasing thresholds of $380\,\mu J/cm^2$ in air and $455\,\mu J/cm^2$ in water were obtained. The values exceed the thresholds of goblet resonators without TiO_2 layer by a factor of almost 10 and 4, respectively. The increase in threshold arises from the lower mode overlap with the gain medium and probably also from lower Q-factors of the TiO_2-coated resonators. Polymeric resonators where the gain medium was deposited externally also exhibit three times higher thresholds in air than their counterparts where the gain medium is integrated into the polymer matrix [176]. However, the lasing thresholds of the TiO_2-coated resonators are still comparably low – when determining the energy required per resonator one obtains values of $E_{\mathrm{threshold}} = 4.8\,\mathrm{nJ}$ in air and $E_{\mathrm{threshold}} = 5.7\,\mathrm{nJ}$ per pulse in water.

To determine the detection limit besides the BRIS also the resolution of the system needs to be considered. As discussed in section 5.1 the resolution depends on the uncertainty in the determination of the peak position σ_{λ_0} and on thermal fluctuations of the peak position. Since the thermo-optic coefficients of PMMA and TiO_2 are comparable the noise caused by temperature-induced shifts in the peak position should be similar for bare PMMA resonators and for resonators with a TiO_2 coating [179]. From BRIS measurements it is evident that there is no dependence of the measurable linewidth of the lasing peaks on the thickness of the TiO_2 coating. An average measurable linewidth of the Gaussian fit of $\delta\lambda_{\mathrm{Gauss}} = 0.033\,\mathrm{nm}$ was obtained. With the Monte-Carlo simulations described in section 5.1 the noise caused from limited precision to determine the peak position was calculated to be $\sigma_{\mathrm{amp}} = 0.71\,\mathrm{pm}$ ($\sigma_{\mathrm{amp}} = 0.28\,\mathrm{pm}$) for peak heights of $h = 200$ ($h = 500$) counts.. The resulting detection limits are depicted in Fig. 5.7. The lowest detection limit of $DL = 2.1 \times 10^{-5}\,\mathrm{RIU}$ was achieved for a TiO_2 coating thickness of 60 nm and a peak height of $h = 500$. Compared to bare PMMA microgoblet cavities the detection limit was

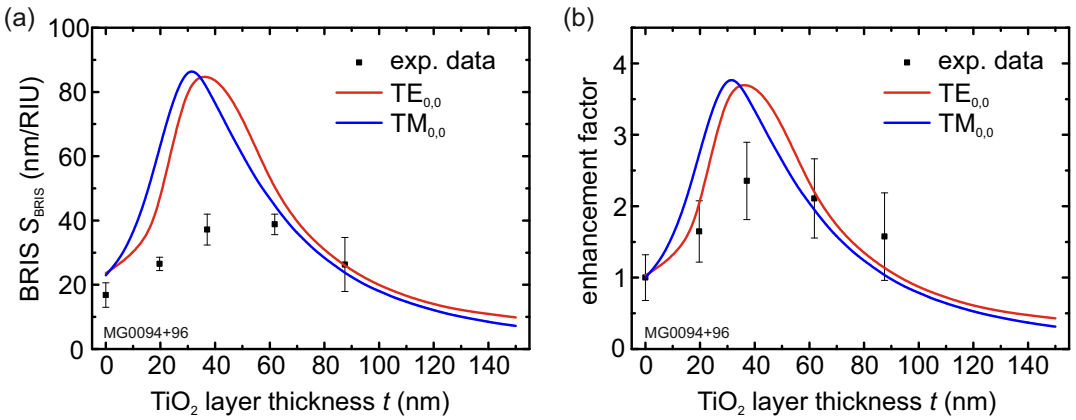

Figure 5.6: Comparison of simulated and measured BRIS values for different TiO_2 layer thicknesses. (a) The experimental BRIS values are not as high as predicted by simulations but the layer thickness yielding the maximum BRIS agrees well. (b) Relative enhancement of the BRIS for different layer thickness. The enhancement factor was calculated from BRIS values of the same cavities before and after deposition of TiO_2. In this way influences from variations in the shape of the goblets are reduced. Adapted from [164].

improved by a factor of 2.3. The absolute detection limit of the WGM lasers is lower than values achieved with surface plasmon resonances ($DL \approx 7 \times 10^{-7}$ [38]) and Mach-Zehnder interferometers ($DL \approx 10^{-7}$ [180]) but comparable to detection limits achieved with photonic crystals ($DL \approx 10^{-5}$ [4]).

5.3 Resonators of Varying Size and Geometry

Another method to increase the overlap of the resonant modes with the surrounding is the variation of the size of the cavity. For resonators of reduced radii or thicknesses an increased BRIS is expected. The fabrication process of dye-doped polymeric microdiscs or -goblets allows to change the radius or the thickness of the cavity simply by changing the lithography pattern or the spin-coating speed, respectively. An advantage of this method is that no additional fabrication step is required.

In this work polymeric discs of different radii and thicknesses were investigated regarding their BRIS, lasing thresholds, and Q-factors. Since in most biosensing experiments liquids are analyzed all measurements were conducted in aqueous environment. The shape of the goblets obtained after the thermal reflow depends on the radius of the pedestal with respect to the radius and the thickness of the PMMA disc. Therefore, to better control the shape of the cavity and to ensure comparabil-

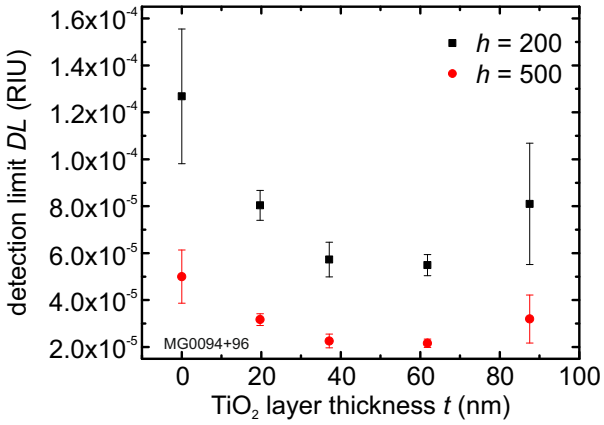

Figure 5.7: Detection limit of resonators coated with TiO_2 for different TiO_2 layer thicknesses. The measurable linewidth of the lasing peaks and thus the resolution remains constant for varying layer thicknesses of TiO_2. The detection limit could be improved by a factor of 2.3 for resonators with a TiO_2 layer of approximately 60 nm.

ity of the different samples the experiments for varying radius and thickness were conducted with disc resonators. Parts of the results presented in this section were achieved in the Master's thesis of Sanaz Rastjoo [168] and are published in [169].

5.3.1 Disc Resonators of Varying Radii

In previous work in our group on polymeric microresonators the standard radius of disc cavities was 25 µm and the thickness was approximately 1 µm. From this starting point the fabrication parameters were modified. In this section the results which were obtained for varying radii are presented.

Fig. 5.8 shows the energy density distribution of resonant modes in two different cavities – one with a radius of $R = 25\,\mu m$ and one with $R = 7.5\,\mu m$ for resonant modes with wavelengths of $\lambda \approx 630\,nm$. The field distribution was obtained from FEM simulations performed with JCMsuite. Obviously the overlap of the resonant mode with the surrounding is increased for smaller cavity radii. Hence, also an increased BRIS is expected.

We fabricated PM597-doped polymeric disc resonators with radii ranging from $R = 5\,\mu m$ to $R = 25\,\mu m$ according to the fabrication procedure described in section 4.2. With SEM images the thickness of the PMMA discs was determined to be $d = 0.9 \pm 0.05\,\mu m$. For all cavities except for the ones with a radius of $R = 5\,\mu m$ lasing in aqueous environment was observed.

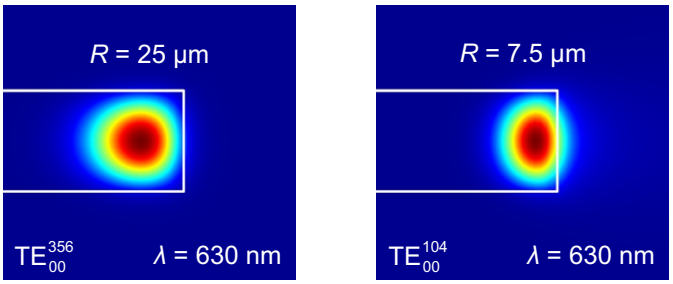

Figure 5.8: Energy density distribution for resonators with a radius of 25 µm and 7.5 µm. It is evident that for a smaller radius of the cavity the overlap of the resonant mode with the surrounding is increased.

BRIS measurements of the different resonators were conducted according to the procedure described in section 5.1. For each radius multiple resonators were investigated. Furthermore, FEM simulations were performed to compare theoretical expectations with experimental results. Since the wavelength of the lasing modes in the experiments decreased from $\lambda \approx 630\,\text{nm}$ for $R = 25\,\mu\text{m}$ to $\lambda \approx 560\,\text{nm}$ (see Fig. 5.9 (b)), simulations were conducted for vacuum wavelengths of 630 nm (green) and 560 nm (blue). In aqueous environment mainly fundamental modes (see e.g. section 3.1.2) are expected to appear in the emission spectrum since they exhibit lower radiation losses than higher-order modes [134]. Hence, simulations were performed for fundamental TE and TM modes.

Fig. 5.9 depicts both the simulation results and the experimental data which are in good agreement. The experimental BRIS values are slightly lower than the predicted ones which could be attributed to the fact that a perfect disc resonator was used for simulations. In reality the resonator exhibits surface imperfections which might lead to a different mode distribution and thus different BRIS values. Since different BRIS values were measured for cavities of the same radius we assume that both fundamental and higher-order modes were present in the emission spectrum. Higher-order modes exhibit a higher overlap with the surrounding medium and hence an increased BRIS compared to fundamental modes. The µ-PL setup only detects scattered light, hence it is not possible to distinguish between TE and TM modes directly. We assume that the data points depicted in red belong to fundamental modes (TE or TM) whereas the black data points belong to higher order modes. By reducing the radius of the cavities the BRIS could be increased from 23 nm/RIU to 60 nm/RIU which corresponds to an enhancement of a factor of 2.6.

The fact that the lasing wavelength decreases with decreasing cavity radius is due to increased radiation losses for smaller cavities in aqueous environment. In the

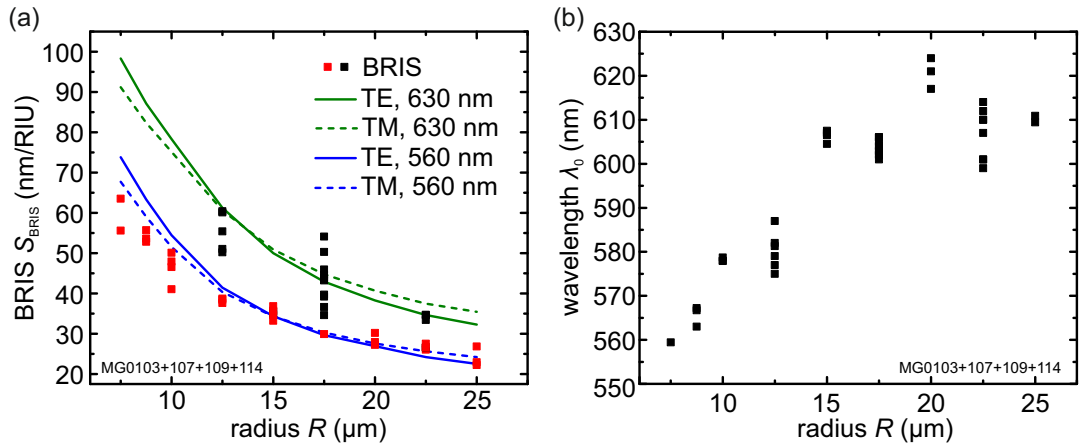

Figure 5.9: (a) BRIS for disc resonators of varying radii. The results from FEM simulations agree well with the measured values. Since the wavelength of the lasing modes decreased with decreasing radius the simulations were performed for wavelengths of $\lambda \approx 560\,\text{nm}$ and $\lambda \approx 630\,\text{nm}$. The data shown in red is assumed to correspond to fundamental modes whereas the data shown in black probably arises from higher-order modes. (b) Lasing wavelengths during the BRIS measurements for different radii. Adapted from [168] and [169].

following the correlation of the lasing wavelength and the Q-factor of the cavity will be discussed. For simulations of the Q-factor absorption losses can be neglected since the absorption of PMMA and water at wavelengths in the visible regime is low [85]. Hence, the imaginary parts of the dielectric functions were set to zero. Scattering losses are difficult to implement into simulations as the rotational symmetry of the cavity is broken and a full 3D simulation would need to be performed. The Q-factor Q_{rad} which only considers radiation losses can be determined from FEM simulations via $Q_{\text{rad}} = \omega_{\text{real}}/2\omega_{\text{imag}}$, where ω_{real} denotes the real part of the eigenfrequency of the mode and ω_{imag} denotes the imaginary part.

Measurements on the passive Q-factors of different cavities were conducted with the tapered-fiber setup described in section 3.3.2. Fig. 5.10 depicts one typical transmission spectrum with a resonant mode (a) and the derived Q-factors in aqueous environment for cavities of different radii as well as the simulation results for Q_{rad} (b). As expected the Q-factor decreases with decreasing radii. For small radii simulation and experiment are in good agreement indicating that radiation losses dominantly limit the Q-factor. For radii exceeding $R = 15\,\mu\text{m}$ the measured Q-factors saturate around values of $Q \approx 8 \times 10^4$, while the values for Q_{rad} from simulations further increase. This indicates that in experiments scattering losses are dominating over radiation losses for cavities with larger radii.

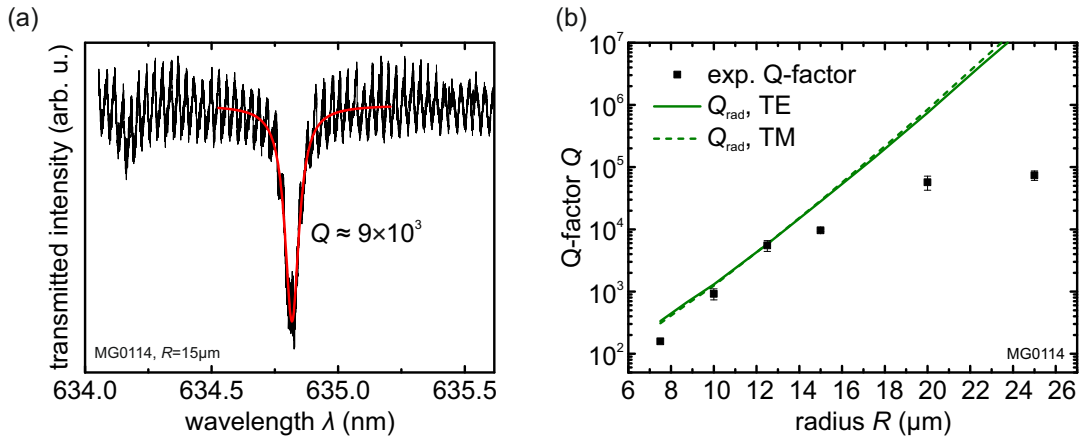

Figure 5.10: Q-factors in aqueous environment for disc resonators of varying radii for wavelength around 635 nm. (a) Typical measurement of the Q-factor showing the transmission spectrum with one resonant mode. A Lorentzian function is fitted to the data to obtain the Q-factor. (b) Simulation results for Q_{rad} and measured Q-factors for different cavity radii. For small radii ($R \approx 7.5 - 15\,\mu\mathrm{m}$) radiation limits the Q-factor, hence experimental data agree well with the simulation results. For larger radii the experimental Q-factor saturates. In this range scattering losses limit the Q-factor. (b) adapted from [169].

The lower Q-factors for smaller radii affect the lasing threshold since the minimum fraction of excited dye molecules required for lasing emission γ depends on the Q-factor (see Eq. 3.16) and the threshold power fluence is proportional to this fraction ($P \propto \gamma$). Fig. 5.11 (a) depicts the fraction of excited molecules required for lasing for different wavelengths and Q-factors. $\gamma(\lambda)$ was calculated according to Eq. 3.16 with the absorption and emission cross sections and the other parameters of PM597 embedded in PMMA given in section 3.2.2. With decreasing Q-factor the fraction of excited dye molecules required for lasing increases and its minimum shifts towards lower wavelengths. For Q-factors below 100 $\gamma(\lambda)$ exceeds unity for all wavelengths meaning that lasing cannot be achieved for the given parameter combination. When considering Q-factors exceeding $Q = 5 \times 10^4$ the value of γ does not change much and approaches zero. This means that the lasing threshold is almost constant for cavities with Q-factors larger than $Q = 5 \times 10^4$.

The blue-shift of the minimum of $\gamma(\lambda)$ with decreasing Q-factor explains that the lasing wavelengths of the polymeric cavities shift to lower wavelengths for smaller Q-factors. In the plot of γ it is not considered that the Q-factor itself is wavelength-dependent. The radiation-limited Q-factor Q_{rad} increases with increasing azimuthal mode number N_Φ meaning that Q_{rad} increases with decreasing wavelength λ. When taking this into account the minimum of $\gamma(\lambda)$ would exhibit an even higher blue-shift than shown in Fig. 5.11 explaining the observed blue-shift of the lasing modes with

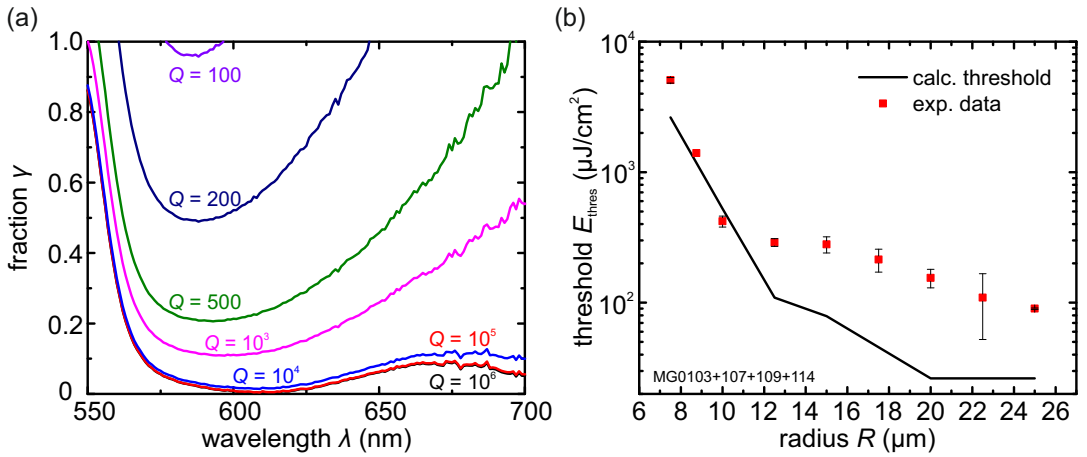

Figure 5.11: (a) Minimum fraction of excited dye molecules required for lasing emission γ for different Q-factors. With decreasing Q-factor the fraction γ increases and its minimum shifts to lower wavelengths. For Q-factors below $Q = 100$ lasing is not possible for the given parameter combination since the fraction γ exceeds unity. (b) Lasing thresholds in aqueous environment for different cavity radii, clearly showing the expected increase due to higher radiation losses for decreasing radius. (b) adapted from [169].

decreasing cavity radius.

Since the lasing threshold power fluence is proportional to γ also an increase of the lasing threshold is expected for cavities of smaller radii. The lasing threshold power fluence can be calculated as follows [117]:

$$P_{\mathrm{th}} = \frac{\gamma h c_0}{\tau \lambda_{\mathrm{P}} \sigma_{\mathrm{abs}}^2(\lambda_{\mathrm{P}}) n_{\mathrm{t}} d}. \tag{5.8}$$

Here, h denotes Planck's constant, c_0 the speed of light in vacuum, τ the fluorescence lifetime of PM597, λ_{P} the pump wavelength, $\sigma_{\mathrm{abs}}^2(\lambda_{\mathrm{P}})$ the squared absorption cross section at the pump wavelength, n_{t} the number density of dye molecules and d the thickness of the cavity disc. Fig. 5.11 (b) depicts the calculated and measured lasing thresholds for cavities of varying radii. For the calculation the Q-factors shown in Fig. 5.10 were used. The calculated lasing thresholds show the same trend as the measured ones and – also quantitatively – the values are comparable since they are in the same order of magnitude. This is convincing especially when considering how many parameters – all exhibiting an uncertainty – enter the calculation of the lasing threshold.

In order to determine whether cavities of smaller radii can improve the detection limit DL first the measurable linewidth of the lasing modes was determined for

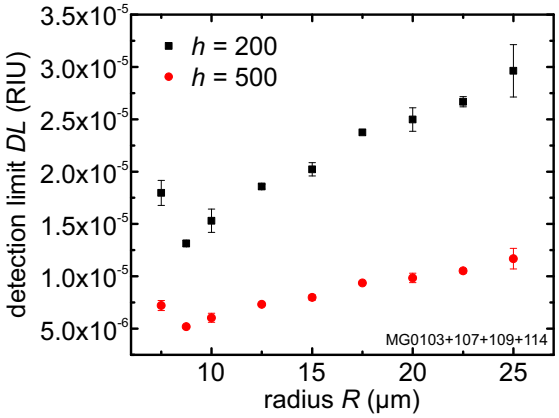

Figure 5.12: Detection limit for disc resonators of varying radii. The detection limit improves with decreasing radius since the BRIS enhances with decreasing resonators while the measurable linewidth of the lasing peaks and thus the resolution remain constant. The only exception are the smallest cavities with a radius of $R = 7.5\,\mu\text{m}$, where the linewidth of the modes increases to $\delta\lambda_{\text{Gauss}} = 0.075\,\text{nm}$.

different radii. Except for the cavities with the smallest radius of $R = 7.5\,\mu\text{m}$ the linewidth of the Gaussian fit remains constant and is limited by the resolution of the spectrometer to $\delta\lambda_{\text{Gauss}} = 0.033\,\text{nm}$. With the Monte Carlo simulations described in section 5.1 the resulting noise in the determination of the peak position σ_{λ_0} and the resolution $R = 3\sigma_{\lambda_0}$ were determined for peak heights of $h = 200$ and $h = 500$ counts above background.

Fig. 5.12 depicts the detection limit which improves from $DL = 1.2 \times 10^{-5}\,\text{RIU}$ to $DL = 5.2 \times 10^{-6}\,\text{RIU}$ with decreasing radius when a peak height of $h = 500$ counts is assumed. Since the measurable linewidth of the lasing modes increases for radii below $R = 8.75\,\mu\text{m}$ a further reduction of the radius does not improve the detection limit further. Thermal noise was neglected when calculating the resolution since it is different for each radii. However, if taken into account it would even enhance the improvement of the detection limit since thermal noise is expected to reduce for smaller cavity radii. Water has a lower thermo-optic coefficient ($\kappa_{\text{water}} = -0.8 \times 10^{-4}$ [181]) than PMMA ($\kappa_{\text{PMMA}} = -1.05 \times 10^{-4}$ [182]), hence, the increased mode overlap with the surrounding should lead to lower shifts of the lasing modes upon changes in temperature.

In summary, it was shown that a decrease of the cavity radius leads to an increased mode overlap with the surrounding resulting in higher BRIS values. Although the smaller radii lead to higher lasing thresholds in aqueous environments the detection limit could be improved by a factor of 2.3 compared to the standard discs.

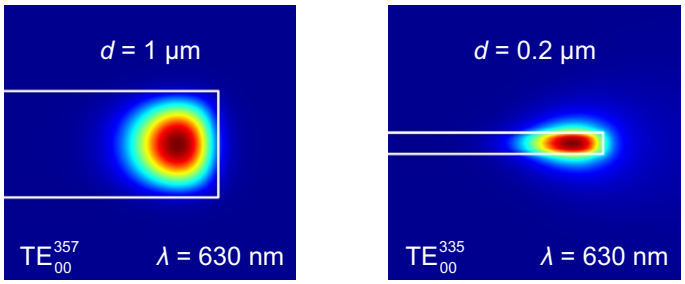

Figure 5.13: Energy density distribution for resonators with a thickness of 1 µm and 0.2 µm. The overlap of the resonant mode with the surrounding is higher for the disc with the lower thickness d. Hence, an enhancement in BRIS is expected for thinner disc resonators.

5.3.2 Disc Resonators of Varying Thicknesses

Another way to increase the overlap of the resonant mode with the surrounding is to reduce the thickness of the resonator discs. The energy density distributions obtained with FEM simulations for resonators with a thickness of $d = 1\,\mu\text{m}$ and of $d = 0.2\,\mu\text{m}$ are depicted in Fig 5.13. Obviously the mode of the thin resonator has an increased overlap with the surrounding than the mode of the thick resonator. Thus, higher sensitivities are expected for resonators of reduced thickness.

We fabricated disc resonators of varying thicknesses by changing the rotation speed during the spin-coating of the PMMA layer. The thickness of the resonators was determined from the cross sections of the cavities. Preparation of the cross sections of the cavities was done with a focussed ion beam (FIB). The results from the FIB cuts agree within a deviation of 10% with the thickness determined from SEM images where the outer rims of the cavities were imaged. Based on these results an uncertainty of the thickness of 10% was assumed for the following experiments.

BRIS measurements for the disc resonators of varying thicknesses were conducted as described in section 5.1. The measurement results as well as the results obtained from FEM simulations are depicted in Fig. 5.14 (a). Since the the lasing wavelengths depend on the thickness of the cavity as visualized in Fig. 5.14 (b) the simulations were conducted for wavelengths of $\lambda \approx 560\,\text{nm}$ and $\lambda \approx 630\,\text{nm}$. The measured BRIS values are in good agreement with the simulated data. The BRIS increases with decreasing cavity thickness and BRIS values as high as $S_{\text{BRIS}} = 156\,\text{nm/RIU}$ are achieved for a resonator with a thickness of $d = 0.2\,\mu\text{m}$. This exceeds the BRIS of the standard cavities by a factor of 6.8.

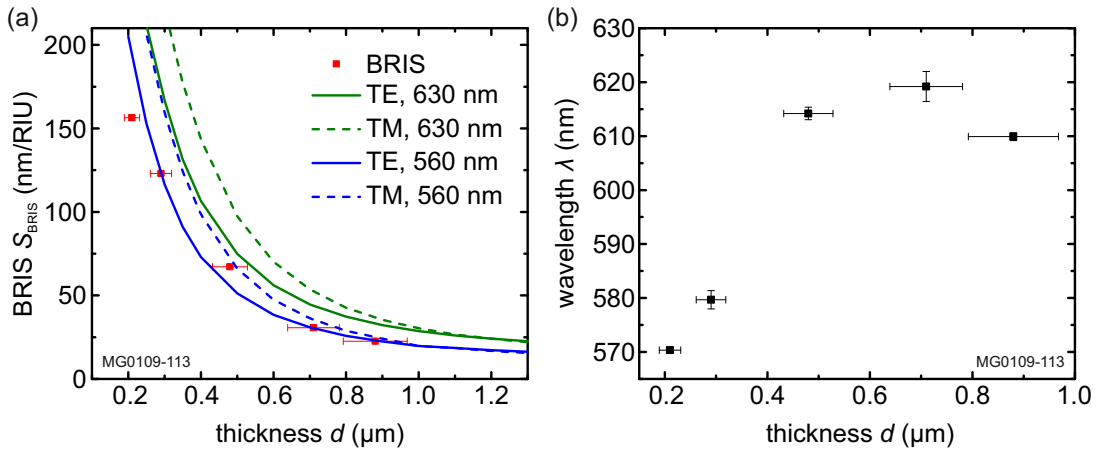

Figure 5.14: (a) BRIS for disc resonators of varying thicknesses. The results obtained from FEM simulations agree well with the measured values. Since the wavelengths of the lasing modes differ for the different samples the simulations were performed for two wavelengths $\lambda \approx 560\,\text{nm}$ and $\lambda \approx 630\,\text{nm}$. (b) Wavelengths of the lasing modes during the BRIS measurements of the resonators of varying thickness. Adapted from [168] and [169].

The lower lasing wavelengths of the resonators of reduced thickness can be explained with lower Q-factors as it was the case for the cavities of smaller radii. Furthermore, a reduction of the resonator thickness goes along with an increase of the lasing threshold as shown in Fig. 5.15 (a). The experimental results on lasing thresholds in aqueous environment and the calculated lasing thresholds determined with Eq. 5.8 are in the same order of magnitude. The increase in threshold is due to the lower Q-factors and due to the reduced thickness of the resonators going along with less absorption of the pump light (compare Eq. 5.8). For the calculations of the lasing thresholds the measured Q-factors shown in Fig. 5.15 (b) were used. For cavities with a thickness below $d = 0.36\,\mu\text{m}$ a measurement of the Q-factor was not possible since no light could be coupled from the tapered fiber into the resonator. This is due to the fact that phase-matching of the mode in the tapered fiber and the mode in the cavity is required for coupling which could not be achieved [183]. For thin resonators a thin tapered fiber is necessary which is then extremely fragile especially in aqueous environment. However, for a cavity thickness of $d = 0.36\,\mu\text{m}$ the measured Q-factor agrees well with the Q-factor from simulations which only considers radiation losses, hence indicating that this is the dominating loss mechanism in experiment. Since radiation losses increase further and are the dominating loss mechanism for thinner cavities we used the Q-factors from simulations to calculate the lasing thresholds of thin cavities. When looking at the Q-factors for cavities with a thickness exceeding $d = 0.5\,\mu\text{m}$ one can see only a slight increase for increasing thickness. In this range scattering losses are the limiting mechanism and the slight increase in Q can be

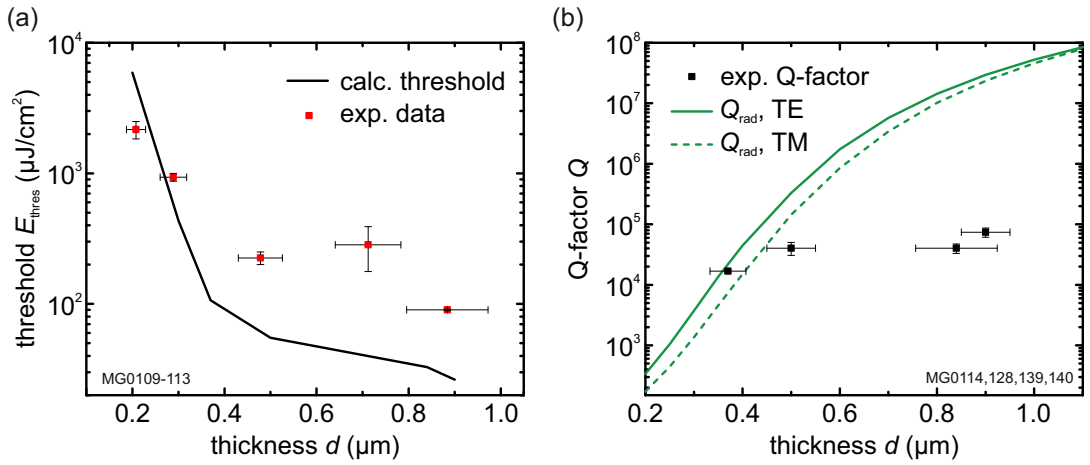

Figure 5.15: (a) Lasing thresholds in aqueous environment for discs of varying thicknesses. Both calculated and measured values increase when the thickness of the cavity is reduced. (b) Measured Q-factors in aqueous environment and simulation results of Q-factors only considering radiation losses. When the cavity thickness exceeds $d = 0.5\,\mu m$ the measured Q-factors saturate since scattering is then the dominating loss mechanism. Resonators thinner than $d = 0.36\,\mu m$ could not be measured but will follow the simulation since their Q-factors are assumed to be radiation-limited. Adapted from [168] and [169].

attributed to the fact that the field intensity at the surface decreases for increasing thickness. Therefore, the influence of surface imperfections reduces with increasing cavity thickness.

The determination of the detection limit for cavities of varying thicknesses was performed in the same way as for resonators of varying radii. The reader is referred to the previous section for further details. The measurable linewidth of the lasing modes remains constant for all investigated resonators, yielding the same resolution of the optical system. Fig. 5.16 depicts the calculated detection limit for peak heights of $h = 500$ and $h = 200$ counts above background. The best achieved detection limit was $DL = 1.8 \times 10^{-6}$ RIU which corresponds to an improvement by a factor 6.8 compared to the value of $DL = 1.2 \times 10^{-5}$ RIU which was achieved for the standard discs.

In conclusion cavities of reduced thicknesses are a good and simple approach to improve the sensitivity of WGM resonators. Just as for cavities of reduced radii the increase in sensitivity is accompanied by an increase in lasing threshold. However, for thin resonators this is partly due to the shorter absorption length and could maybe be compensated by increasing the dye concentration. For all investigated

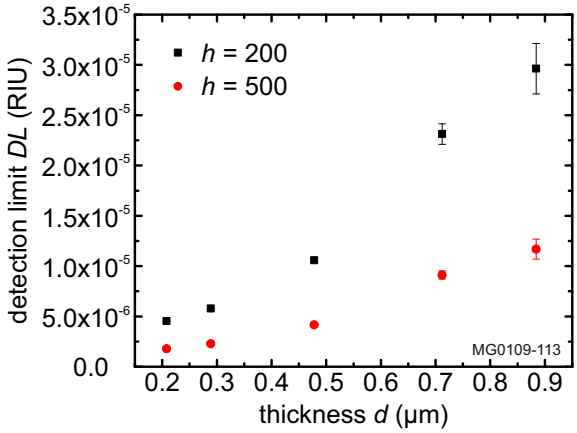

Figure 5.16: Detection limit for resonators of varying thicknesses. With decreasing thickness of the cavity the detection limit improves continuously. For the investigated cavities the detection limit was improved by a factor of 6.8 compared to the value of a standard disc cavity.

cavities of varying thicknesses the measurable linewidth of the lasing modes remains constant leading to an improvement of the detection limit up to a factor of 6.8.

5.3.3 Goblet Resonators of Optimized Size

In the previous sections it was shown that cavities of reduced radii and thicknesses exhibit enhanced sensitivities. However, this improvement goes along with an increase in lasing threshold due to reduced Q-factors. For cavities of reduced radii radiation losses limit the Q-factor. When reducing the thickness first scattering losses seem to increase and the radiation-limited Q-factor regime is reached when the thickness goes below $d \approx 0.4\,\mu m$. While radiation losses cannot be influenced for a given cavity radius and thickness, scattering losses can be reduced when surface imperfections are minimized. As mentioned in section 4.2 for polymeric resonators a thermal reflow step – during which the cavities are heated above the glass transition temperature of PMMA – smoothens the cavity surface and leads to a significant enhancement of the Q-factor [107].

In this work a thermal reflow was applied to disc resonators with a radius of $R = 25\,\mu m$ and a thickness of $d \approx 0.4\,\mu m$. Fig. 5.17 (a) depicts a SEM image of a resulting microgoblet. In order to test whether the goblet resonators show an improved performance compared to the disc resonators the lasing threshold in aqueous environment and the BRIS were measured and compared. The results are shown in Fig. 5.17. Lasing thresholds of $E_{\mathrm{threshold}} = 25\,\mu J/cm^2$ were achieved in aqueous envi-

ronment which is a factor of 3.5 lower than the value of the comparable disc-shaped counterparts.

During the BRIS measurement doublets of lasing modes in a spectral distance of the free spectral range were observed in the emission spectrum as shown in Fig. 5.17 (c). We assume that these are fundamental modes with TE and TM polarization. For both kind of modes the BRIS was determined as $S_{\mathrm{BRIS}} = 48\,\mathrm{nm/RIU}$ and $S_{\mathrm{BRIS}} = 64\,\mathrm{nm/RIU}$, respectively. A comparison to the simulation results shown in Fig. 5.14 (a) confirms the assumption that TE and TM modes are observed. The fact that the simulations were conducted for disc resonators instead of goblets should not have a strong influence since the thickness and the radius are the main quantities which determine the BRIS. The slight reduction in cavity radius ($R = 22.5\,\mu\mathrm{m}$ compared to $R = 25\,\mu\mathrm{m}$) due to the thermal reflow does not have a strong impact on the BRIS so the radius change was neglected. When comparing the measured sensitivities with the simulation results we can conclude that the mode with the higher BRIS is the TM mode. Furthermore, when the values are compared quantitatively one can see that the values correspond to a cavity thickness of approximately $0.65\,\mu\mathrm{m}$. This value is higher than the initial thickness of the disc which indicates that a bead has formed at the rim of the cavity during the thermal reflow.

In summary, the reflow process leads to a reduced lasing threshold while the resulting thin microgoblet still exhibits an enhanced sensitivity compared to the standard disc. When the diameter of the pedestal is controlled precisely it is possible to reproduce the goblet shape and maintain the improved performance.

5.3.4 Comparison of the Different Approaches

In this section the different approaches for the enhancement of the sensitivity are compared. Since an increase in sensitivity usually goes along with the drawback of an increase in lasing threshold the different approaches presented in the previous sections are compared in two manners:

First, only the bare detection limits are compared and no attention is paid to the increase in threshold. Since the lasing thresholds of the disc resonators which served as a starting point are comparably low an increase of the threshold is acceptable as long as the operational lifetime of the lasers is sufficient for sensing experiments. All of the investigated samples (except for the discs with a radius of $R = 7.5\,\mu\mathrm{m}$) showed sufficient operational lifetimes to conduct regular BRIS measurements. Therefore it is expected that also sensing experiments are feasible with increased thresholds.

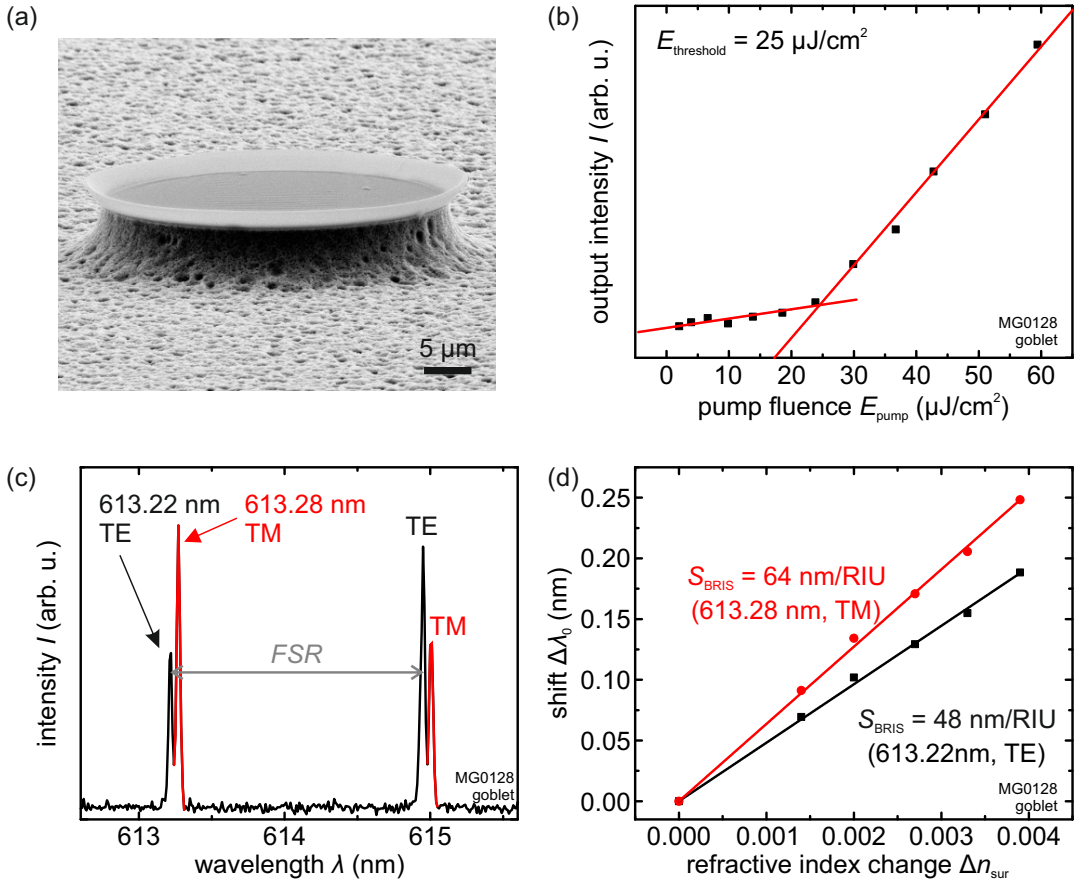

Figure 5.17: (a) SEM image of a goblet made from a disc with a thickness of $d \approx 0.4\,\mu m$. (b) The goblet resonators exhibit lasing thresholds of $E_{\mathrm{threshold}} = 25\,\mu J/cm^2$ in aqueous environment. (c) Part of the lasing spectrum of the thin goblet cavity showing doublets of lasing modes separated by the free spectral range. The two modes are probably fundamental modes with TE and TM polarization. (d) Results on BRIS measurements show that the different modes exhibit different sensitivities.

Second, a new figure of merit is defined as the ratio of the BRIS to the lasing threshold in aqueous environment and the resulting values are compared. Besides these two comparisons also intermediate regimes where, e.g., all cavities with a lasing threshold below a certain value are compared regarding their detection limit, can be thought of. However, the figure of merit depends on the final application and needs to be defined individually.

Besides the approaches presented in this work also a standard goblet which was used previously in our research group and coupled polymeric microdiscs investigated by Tobias Großmann [11] are included in the comparison. For the approaches where a parameter sweep was performed the best result was used for the comparison to ensure clarity.

Fig. 5.18 (a) compares the different resonators regarding the achieved detection limits. Here, a peak height of $h = 500$ counts above background was used to determine the resolution and it was assumed that the measurable linewidth of the lasing modes of the standard goblet and the coupled microdiscs is also $\delta\lambda_{\mathrm{Gauss}} = 0.033\,\mathrm{nm}$. The comparison shows that all approaches, covering the resonators with TiO_2, reducing the radius and the thickness and the coupling of two resonators improve the detection limit compared to the standard goblet. The best result was achieved for disc resonators with a thickness of $d = 0.21\,\mu\mathrm{m}$, which show a detection limit of $DL = 1.8 \times 10^{-6}\,\mathrm{RIU}$ corresponding to an improvement by a factor of 6.8.

The results of the second comparison also considering the lasing threshold are depicted in Fig. 5.18 (b). The performance of the disc cavities of reduced radius and thickness is comparable to the one of the standard goblet, while the TiO_2-coated cavities and the coupled discs suffer from higher lasing thresholds. The goblet of reduced thickness shows the best value for the ratio of BRIS to lasing threshold which exceeds the one of the standard goblet by more than an order of magnitude. This is due to the higher BRIS value of the thin goblet but also due to its low lasing threshold which is even lower than the one of the standard goblet. One reason for this might be that the radius of the standard goblet is smaller than the radius of the thin goblet leading to higher radiation losses and hence an increased lasing threshold. The good performance of the thin goblet shows that the reflow process reduces the surface roughness and that sensitive resonators with low thresholds are feasible.

So far only performance parameters have been compared. Another point is that the approaches where the size of the resonators is changed do not require an additional fabrication step. This is needed for the TiO_2-coated cavities but also for the coupled microdiscs since the coupling gap after fabrication was closed by depositing an additional polymer layer onto the discs by using chemical vapor deposition [184]. The

thermal reflow also represents an additional fabrication step, however, very simple to implement.

In conclusion the use of disc or goblet cavities of reduced thickness is a simple method how the sensitivity can be improved with no or little effort for further fabrication steps. When the thickness is kept larger than approximately half of the wavelength of the emission light the increase in lasing threshold should be in an acceptable range. The thermal reflow step can reduce the surface roughness further improving the properties of the cavities.

5.4 Summary and Conclusions

In this chapter different approaches for the enhancement of the sensitivity of polymeric WGM lasers were presented and compared. First, the focus was set on the standard figures of merit such as the sensitivity, the resolution and the detection limit. It was discussed how these quantities can be determined for WGM lasers and which influences they depend on. Since the resolution for peak shifts of WGM lasers besides thermal noise mainly depends on the spectrometer used for the read-out of the lasing modes the resolution usually remains constant even if the Q-factor of the cavity decreases. In order to improve the detection limit of WGM lasers the best approach is to increase the sensitivity. To do so different approaches were presented in this chapter. Goblet-shaped cavities were coated with TiO_2 serving as a high-refractive index coating layer which pulls the resonant modes towards the rim of the cavity an hence increases the mode overlap with the surrounding medium. The thickness of the TiO_2 coating layer was varied and the different resonators were investigated regarding their BRIS. Results from FEM simulations and experiments for the different thickness of TiO_2 are qualitatively in good agreement and the quantitative deviations can be explained by the varying geometry of the TiO_2 coating layer.

Afterwards a detailed investigation on polymeric cavities of varying dimensions and geometries was presented. Both, radius and thickness of the cavity were reduced in order to increase the sensitivity. The different resonators were characterized regarding their BRIS, their lasing thresholds and their Q-factors in aqueous environment. With decreasing radii or thicknesses of the cavities the BRIS was enhanced while the Q-factor was reduced and an increase in lasing threshold was observed consequently. However, the measurable linewidth of the lasing modes remained constant so the increase in sensitivity leads to an improvement of the detection limit up to a factor of 6.8.

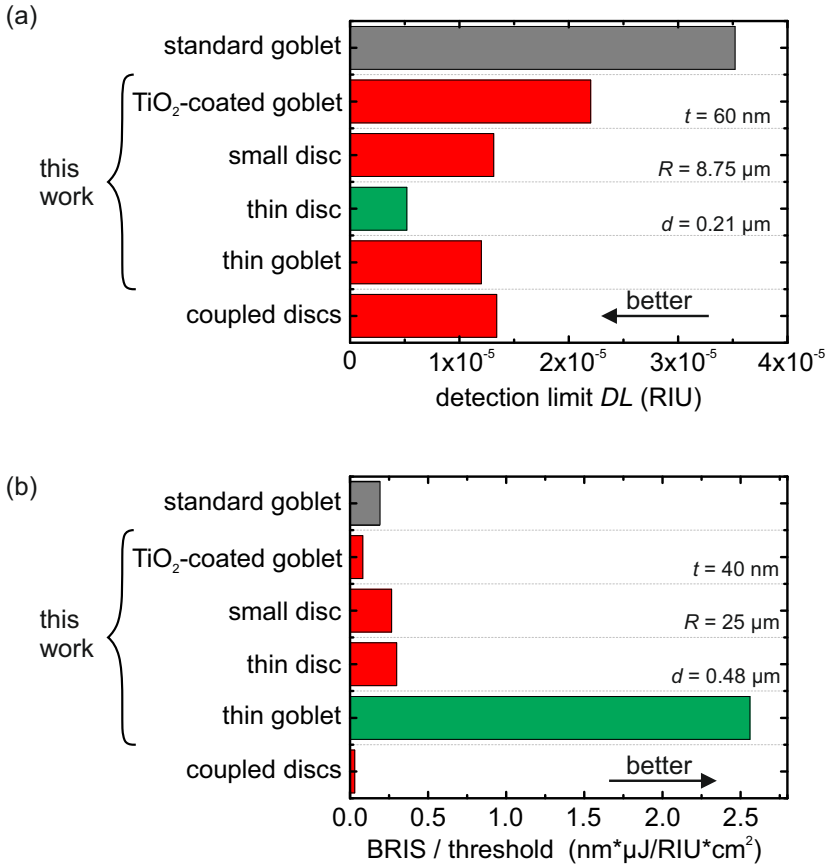

Figure 5.18: Comparison of the different approaches to improve the detection limit by enhancing the sensitivity. (a) The comparison of the achieved detection limits shows that resonators of reduced thicknesses exhibit the best detection limit DL which can be as low as $DL = 1.8 \times 10^{-6}$ RIU. (b) When the ratio of the BRIS to the lasing threshold is used as figure of merit the thin microgoblets show the best performance.

In order to minimize scattering losses and to maintain low lasing thresholds while achieving improved sensitivities goblet resonators of reduced thickness were fabricated. The obtained results confirmed the expectations since the sensitivity could be improved up to a factor of 2.8 while the lasing threshold was even lowered compared to disc resonators.

In the last section of this chapter the different approaches namely TiO_2-coated microgoblets and disc- and goblet-shaped cavities of reduced dimensions were compared quantitatively. In the comparison also former results – the standard goblet and coupled disc cavities – were included. When only the detection limit is considered it turns out that microdiscs of reduced thickness provide the best performance while when also the lasing threshold is taken into account the goblets of reduced thickness achieve the best results.

Chapter 6

Lasing Emission from Random Resonators in Electrospun Dye-Doped Polymer Fiber Networks

This chapter focusses on dye-doped electrospun polymer fiber networks and the origin of their lasing emission. First the principle of elctrospinning and the geometrical structure of the resulting fibers are presented. In the second part the lasing properties of the polymer fiber networks investigated in this work are discussed. In the last part it will be shown that random resonators are responsible for the lasing emission. Furthermore, the theory of directional couplers is introduced and applied to the coupling region of the fiber resonators.

Parts of the presented results were obtained during the Bachelor's thesis of Stefan Schierle [185]. Furthermore, most results were published in [132].

6.1 Electrospun Polymer Fiber Networks

Electrospinning is an established and simple technique for the fabrication of one-dimensional structures which are small in diameter (down to $d < 100\,\mathrm{nm}$) and can be extremely long in length ($l > 1\,\mathrm{km}$) [186]. In the following these structures will simply be referred to as fibers. A tremendous variety of materials including different polymers, ceramics and composites has successfully been used for the fabrication of electrospun fibers [187, 188]. Hence, the fiber properties such as stiffness, weight,

porosity, surface functionality and biocompatibility can be tuned and adapted according to the purpose of the fibers [186, 187]. In the field of optics and photonics electrospun fibers are of high interest since their optical properties such as the refractive index can be tuned. Furthermore, optically active dopants such as dyes or nanoparticles can be incorporated to realize broad-band light-sources or even lasers [189–192].

6.1.1 Principle of Electrospinning

The basic electrospinning setup is simple and consists of three main parts: a high-voltage power supply, a metallic syringe needle and a collector, which is a grounded electrode essentially. In Fig. 6.1 (a) a schematic of an electrospinning setup is shown. The metal needle is attached to a syringe which is filled with the solution (or melt) of the fiber material, which is a polymer is this work. The use of a syringe pump allows control over the flow rate of the polymer solution. A high voltage is applied between the metal needle and the collector. The drop of polymer solution at the nozzle is electrified and the induced charges will distribute homogeneously on the surface. Due to repulsive electrostatic forces between the surface charges and Coulomb forces of the external field the droplet deforms into a conical object which is known as Taylor cone. When the voltage is high enough repulsive electrostatic forces overcome surface tension and a liquid jet is ejected. The jet experiences a stretching and whipping process during which the solvent evaporates and long, thin fibers are formed. Different theories and models based on experimental observations have been developed to describe and understand this rather complex spinning process [193–195]. The charged fiber is attracted by the collector and often deposited in a random orientation. The resulting fiber network is also called a non-woven web. In Fig. 6.1 (b) a photograph of such a fiber network with varying density is depicted.

The polymer fiber networks investigated in this work were fabricated by Dr. Lars Jørgensen and Dr. Ana C. Mendes at the Technical University of Denmark (DTU). PMMA doped with the dyes Rhodamine 6G (Rh6G) or PM597 is used as fiber material and a silicon wafer coated with 200 nm SiO_2 to enable light propagation in the fibers serves as collector. Typical fiber diameters are in the order of 1 micrometer.

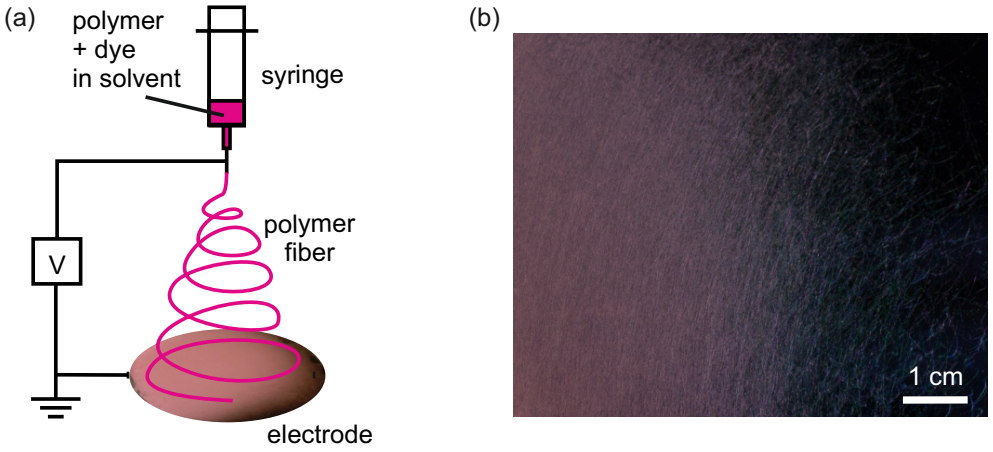

Figure 6.1: (a) Electrospinning setup consisting of a high voltage supply, a syringe with a metal needle and a collector. (b) Image of Rh6G-doped electrospun polymer fiber networks with varying fiber density. (a) adapted from [132].

6.1.2 Structure and Alignment of Electrospun Fibers

The fibers investigated in this work exhibit a smooth surface and a solid interior. The fibers are randomly distributed on the silicon wafer as can be seen in the SEM images shown in Fig. 6.2. The density of the fibers ranges from single layers to dense networks of fibers. Throughout the fiber network random resonators are distributed. They consist of a fiber running in parallel with itself for a certain distance after forming a loop. Examples for such resonators are depicted in Fig 6.2 (c) and (d).

As mentioned before electrospinning is a flexible fabrication technique which allows the use of different materials but also modification of the fiber structure and fiber alignment [187]. Concerning the fiber structure so-called core-shell fibers consisting of two different materials can be fabricated by using coaxial capillaries for electrospinning [196]. Furthermore, by using the same setup fibers with hollow interior can be realized by removing the interior material after fabrication [197, 198]. Besides core-shell structures also fibers consisting of two or multiple components are feasible [199]. The nozzles are arranged side by side and fibers with multiple functionality can be obtained [199]. Furthermore, porous fibers or fibers with a specific surface morphology have been realized [200].

For some applications also the spatial alignment of the fibers is important. In the field of photonics axially aligned fibers have been used as polarizers [201] or as polarized light sources in lab-on-a-chip applications which allow for the separation of excitation and emission light [202]. Different methods based on modifications of the electrospinning collector have been implemented to realize aligned fibers [203].

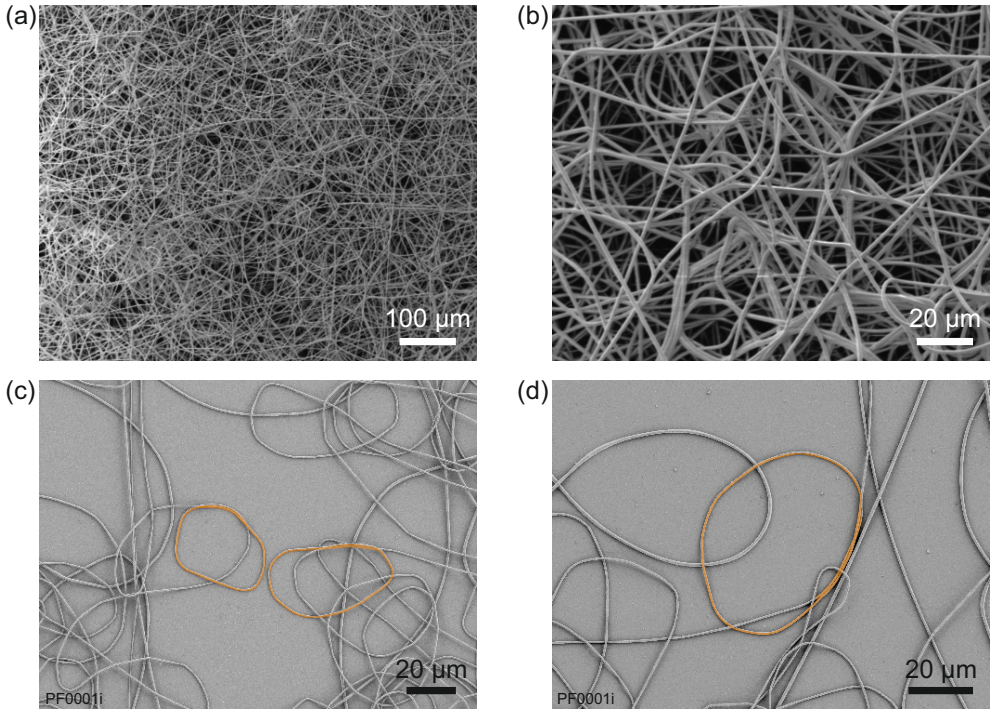

Figure 6.2: SEM images of electrospun polymer fibers. (a) and (b) Region with high fiber density illustrating the random alignment of the fibers. Images were taken at the DTU, Denmark. (c) and (d) Examples for random resonators (marked in orange) within the polymer fiber network. (a) and (b) taken from [132].

For example parallel plates [201] or rotating drums have been used, the latter one even allows the fabrication of complex 3D architectures such as yarns [204] or tubes [205]. In 2006, near-field electrospinning (NFES) was introduced allowing precise deposition of fibers by using short distances between needle tip and collector, thus exploiting the stable linear region of the jet trajectory [206]. By moving the collector within the plane perpendicular to the fiber jet almost arbitrary patterns of fibers can be designed [207].

6.2 Lasing emission: Observations

The photoluminescence (PL) of dye-doped electrospun fiber networks has been investigated with the µ-PL setup described in section 3.3.1. Fibers doped with either Rh6G or PM597 were excited with ns-pulses of the frequency-doubled Nd:YVO_4

laser and the emitted light was spectrally analyzed. Different positions of the samples were investigated.

6.2.1 Typical Photoluminescence Spectra

In Fig. 6.3 typical PL-spectra of Rh6G-((a)-(d)) and of PM597-doped ((e)-(h)) electrospun fibers and corresponding images of the fibers at the same position under laser illumination are depicted. Obviously, the spectra taken at different positions of the sample differ significantly. In spectrum (a) and (e) only bare fluorescence is visible whereas all the other spectra exhibit sharp peaks. At some sample positions spectrally regular spaced comb-like peaks with a clear free spectral range are observed as shown in (d) and (h). At other positions the spectral distribution of the peaks is irregular and the spectral distance between adjacent peaks is random. The density of the fiber network does not determine the emission spectra since for comparable fiber density bare fluorescence (a), peaks with a regular spectral distribution (h) and peaks with a random spectral distance (c) are observed.

As will be shown in the following the sharp peaks originate from random resonators within the fiber network providing the feedback mechanism required for lasing. The different emission spectra presented can be explained as follows: At positions with bare fluorescence no resonator is present while comb-like lasing emission is attributed to a single resonator its length yielding the corresponding free spectral range. Spectra with many irregularly spaced peaks arise, when multiple resonators with different sizes overlap spatially and lasing emission of multiple resonators contributes to the spectrum. Throughout the different sample positions spots with lasing emission are frequent, especially at sample areas with high fiber density. In regions with low fiber density lasing emission is more rare but still easy to find.

6.2.2 Lasing Thresholds

In order to verify that the peaks observed in the emission spectra are due to lasing so-called input-output curves were measured. For increasing excitation energy the output intensity of a peak is monitored. In Fig. 6.4 (a) the integrated intensity of the lasing mode which appears at the lowest energy is plotted versus the excitation energy for a PM597 fiber resonator. A clear change in slope can be observed when the energy overcomes the threshold – a typical characteristic for lasing [208]. The lasing threshold is determined from the intersection of the two linear regressions to be $26.5\,\mu J/cm^2$ per pulse. In the emission spectra taken at different excitation energies

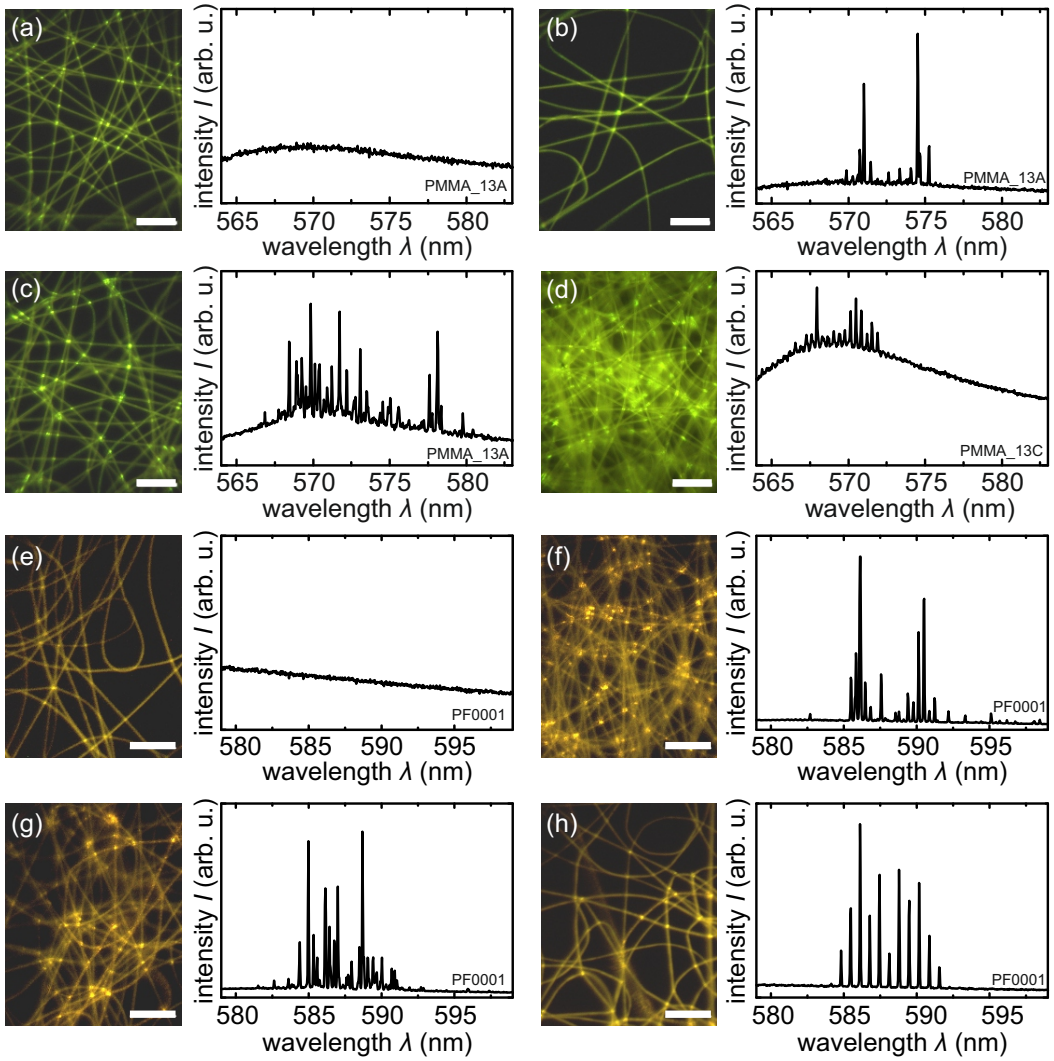

Figure 6.3: Typical photoluminescence spectra of dye-doped electrospun polymer fiber networks. (a) to (d) Rh6G-doped, (e) to (h) PM597-doped. The different characteristics, (a) and (e) bare fluorescence, (d) and (h) comb-like lasing peaks and (b), (c), (f) and (g) spectrally irregular spaced lasing peaks can be explained by resonators randomly distributed in the fiber network. Scale bar is 30 µm. The different colors of the fibers under laser illumination arises from the use of different long-pass filters in the detection beam path. (a) to (d) taken from [132].

emerging peaks demonstrate the onset of lasing (Fig. 6.4 (b)). The input-output curve for fibers doped with Rh6G is shown in Fig. 6.4 (c). Spectra were taken at a sample position where the spectral distance between the lasing peaks is irregular. The lasing thresholds of two different peaks were determined to be 3.1 mJ/cm^2 and 5.1 mJ/cm^2 per pulse. The corresponding spectra at different excitation energies are shown in Fig. 6.4 (d). It is clearly visible that the lasing thresholds for different peaks are distinct. One possible explanation is that the peaks belong to different resonators exhibiting different Q-factors and hence different lasing thresholds.

When the thresholds of the samples with the different dyes are compared it is evident that PM597-doped fibers show thresholds which are lower then those of Rh6G-doped fibers. Since each resonator exhibits a different threshold due to a different Q-factor single threshold measurements will not allow a statement on which dye shows the better performance. However, when the range of the measured thresholds is compared thresholds for Rh6G-doped samples range from 1.3 mJ/cm^2 to 3.3 mJ/cm^2 per pulse whereas for PM597 thresholds between 27 µJ/cm^2 and 875 µJ/cm^2 per pulse have been measured. The lower threshold values of PM597-doped fibers could be due to a higher quantum yield of PM597 when integrated in PMMA. For comparison, in [11] Rh6G and PM597 have been embedded in goblet-shaped whispering gallery mode resonators made of PMMA. For the same resonator geometry and hence comparable Q-factors the lasing thresholds of Rh6G-doped resonators exceeded the ones of PM597-doped resonators by a factor of six which is similar to the observations made in the polymer fiber networks in this work. Camposeo *et al.* observed lasing thresholds of approximately 60 µJ/cm^2 for fiber pieces acting as Fabry-Pérot cavities with Rh6G as gain medium at a comparable concentration as used in this work. The lower threshold energy when compared to the Rh6G-doped fibers investigated in this work is due to the shorter excitation pulses of only 0.6 ns which results in higher peak power fluences.

6.3 Lasing Mechanism of Fiber Resonators

To show that random resonators within the polymer fiber network are the origin of lasing emission the fiber networks were analyzed with spatially resolved spectroscopy. At the beginning of this section the method of spatially resolved spectroscopy is explained. Then examples of random resonators are presented and their emission spectra are analyzed quantitatively. Finally, the theory of directional couplers is introduced which is used to describe the light propagation in the coupling region of the fiber resonators in this work.

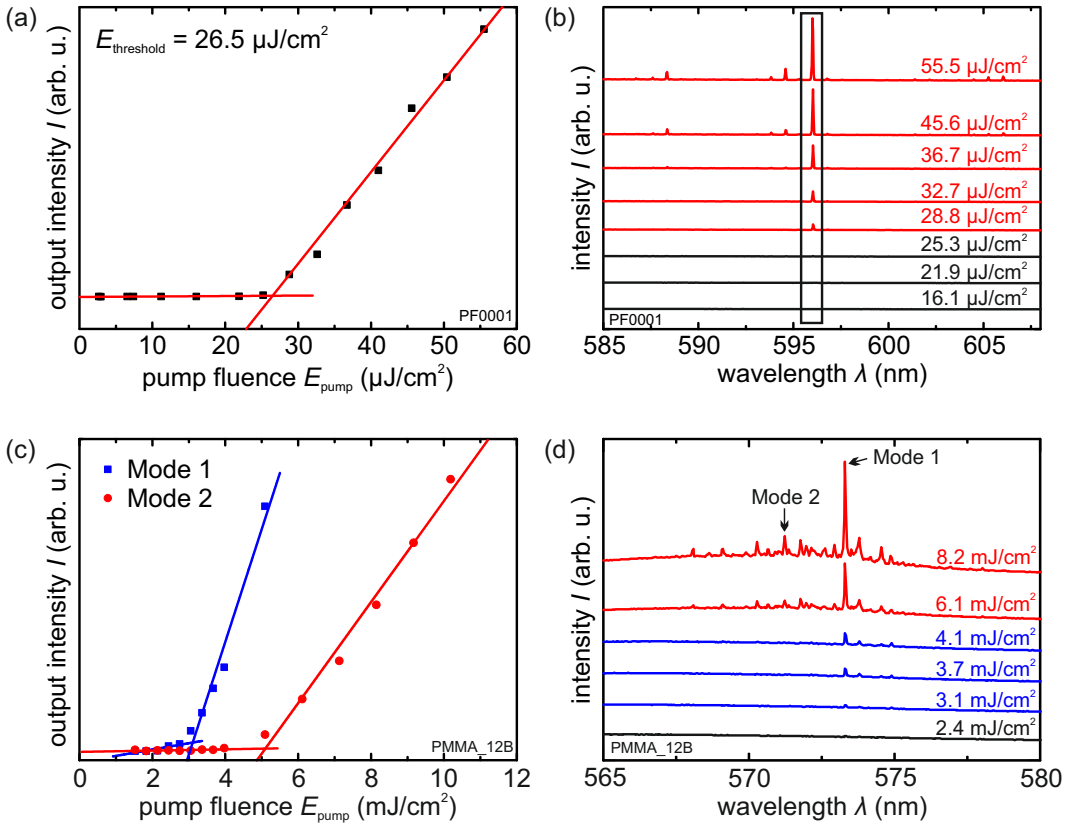

Figure 6.4: Lasing threshold of dye-doped electrospun polymer fibers. (a) Example of an input-output curve for a single resonator in a PM597-doped fiber network. The intersection of the two linear regressions at 26.5 µJ/cm^2 represents the lasing threshold. (b) Corresponding emission spectra taken at different excitation energies clearly showing the lasing mode appearing above threshold energy. (c) and (d) Analogue graphs for Rh6G-doped fiber networks. The lasing threshold is determined for two different modes probably belonging to two different resonators. The emission spectra show the onset of lasing. (c) and (d) taken from [132].

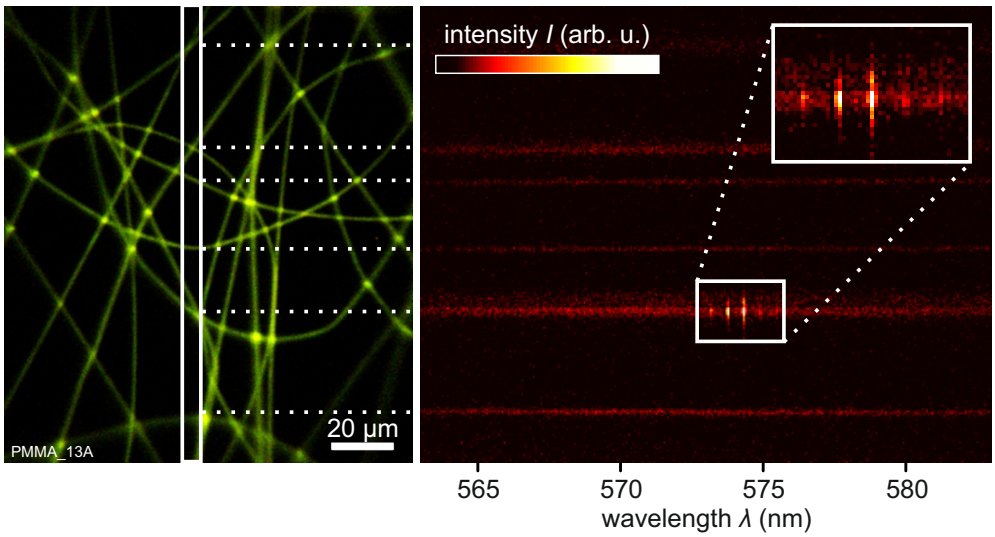

Figure 6.5: Spatially resolved spectroscopy. A photograph of the fiber network and a spatially resolved spectrum are taken at the same sample position. The position of the entrance slit is mapped onto the photograph so that the luminescence in the spectrum can be assigned to the corresponding fiber. Taken from [132].

6.3.1 Spatially Resolved Spectroscopy

The setup used for spatially resolved spectroscopy is the same as the one described in section 3.3.1. In order to get a spatial resolution each pixel of the CCD camera coupled to the spectrometer is read out separately yielding a spectral resolution along the x-axis and additionally spatial resolution along the y-axis. Simultaneously a photograph of the corresponding sample area under laser illumination is recorded. The position of the entrance slit of the spectrometer is mapped onto the photograph. This way the photoluminescence in the spectrum can be assigned to the fiber it originates from. In Fig. 6.5 an example of a photograph and a corresponding spatially resolved spectrum is shown. At sample positions where the fiber density is low one can clearly identify the fiber the lasing emission is originating from. The sample holder with the fiber networks can be moved laterally in x- and y-direction. This allows to track the fibers exhibiting lasing emission and to identify random resonators and their corresponding emission spectra.

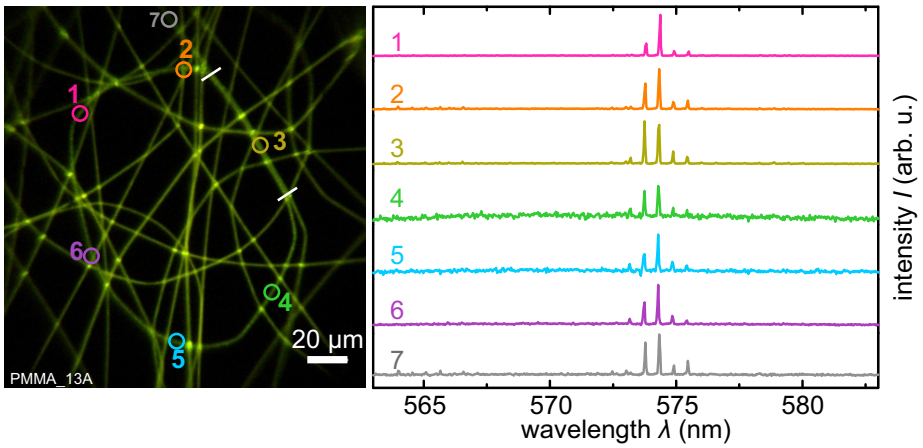

Figure 6.6: Example of a simple random resonator (Res 1) in the polymer fiber network and emission spectra taken at different positions of the resonator. The fiber forms a loop and then overlaps with itself (marked with white bars) where light couples from one part of the fiber to the other and forms a closed optical path. Taken from [132].

6.3.2 Geometry of Random Resonators

In this section it will be shown that random resonators are the origin of the lasing emission in electrospun polymer fiber networks. For this the data recorded with spatially resolved spectroscopy was analyzed qualitatively and quantitatively. In random resonators the light is guided along a fixed optical path in contrast to random lasing where the light spreads through the medium over statistically varying paths. The mechanism of random lasing has been excluded for the polymer fiber networks by performing single-shot experiments [209].

Fig. 6.6 shows an example of a random resonator. Furthermore, spectra along different positions of the resonator are depicted. The fiber forms a closed loop by running in parallel with itself for a certain distance. The light couples from one part of the fiber to the other thus forming a closed optical path. Along the resonator (see Fig. 6.6, position 1-6) and also at adjacent parts of the fiber (position 7) the same comb of lasing modes is observed. The varying intensity of the lasing peaks arises from the fact that only scattered light is collected with the spectrometer and hence, the intensity depends on the presence of scatterers. Fibers which only cross the resonator only show bare fluorescence. At the crossing points no efficient coupling occurs. This is consistent with similar results observed in silica fibers [210].

The formed geometry is different for each resonator. In Fig. 6.7 a more complex resonator structure is depicted but again after several loops the fiber reaches its

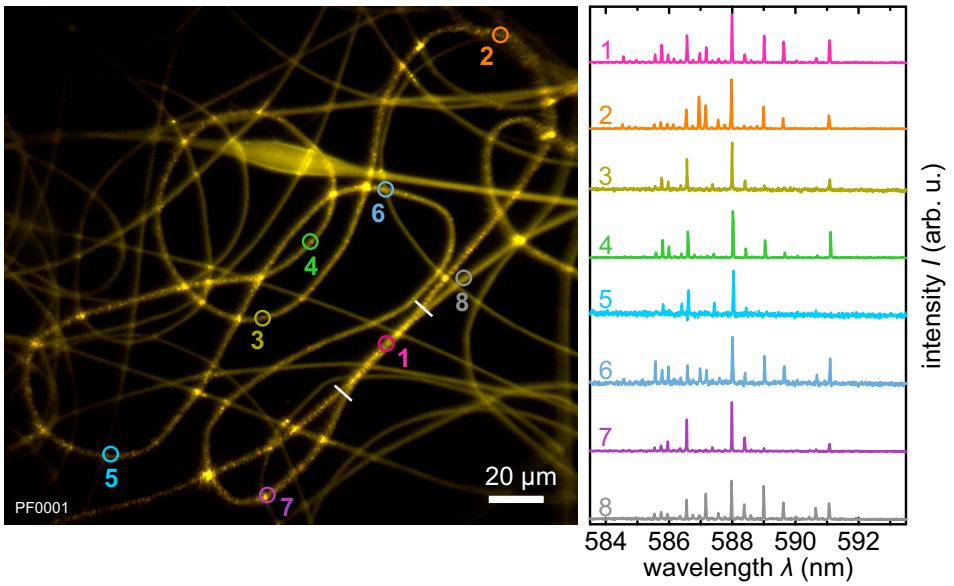

Figure 6.7: Example of a more complex random resonator (Res 2) in the polymer fiber network and emission spectra taken at different positions along the resonator. Still, after forming some loops the fiber runs in parallel with itself and forms a closed optical path.

starting point and runs in parallel with itself. The spectral distance between two adjacent modes is shorter than for Res 1 (compare Fig. 6.6) since the resonator length is larger. As the modes compete for gain some of the modes are suppressed in the emission spectrum. In principle arbitrary resonator geometries are possible as long as a closed optical path is created where light can couple from one part of the fiber to the other in the coupling region.

Depending on the fiber diameter and the coupling length (the length for which the fibers run in parallel) the coupling is more or less efficient. Since the lasing modes are also observed in adjacent fiber parts which do not belong to the resonator the coupling efficiency is below 100% (compare Fig. 6.6, position 7). A more detailed discussion and comparison with simulation results will be given in section 6.3.3. To further prove that the lasing emission originates from the random resonators a quantitative analysis of the spectra was performed. By using the free spectral range FSR, the spectral distance between two adjacent modes the resonator length L_R can be calculated with

$$L_\mathrm{R} = \frac{\lambda_1 \lambda_2}{n_\mathrm{eff} |FSR|}, \tag{6.1}$$

where λ_1 and λ_2 are the wavelengths of the two adjacent modes. The effective refractive index n_eff depends on the diameter of the fiber and is determined using modal

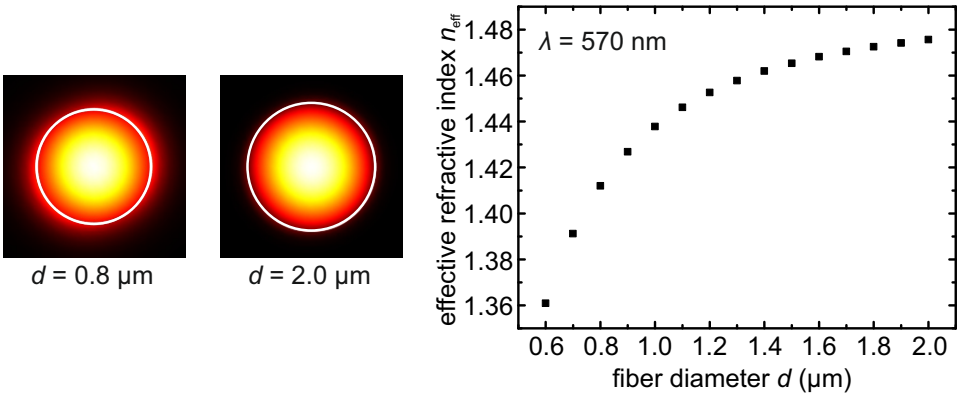

Figure 6.8: Mode profile and effective refractive index n_{eff} of the fundamental mode for varying fiber diameters. For smaller diameters a larger fraction of the mode is localized outside the fiber resulting in a lower effective refractive index. Simulations were carried out with COMSOL for a wavelength of $\lambda = 570\,\text{nm}$. Adapted from [132].

analysis based on the finite element method (FEM) performed with COMSOL. The dispersion of PMMA and the influence of the dye molecules on the refractive index of PMMA is neglected for the spectral region of lasing emission and a constant value of $n_{\text{PMMA}} = 1.49$ is assumed. In Fig. 6.8 the effective refractive index is plotted for different fiber diameters. Furthermore, the normalized electric field in the fibers and their surrounding is shown for fiber diameters of 0.8 µm and 2.0 µm. As the mode overlap with the surrounding decreases for increasing fiber diameter the effective refractive index approaches the refractive index of PMMA.

By using Eq. 6.1 and the simulation results for the effective refractive index n_{eff} the resonator length is calculated for different fiber diameters and compared to the measured resonator length obtained from the photographs. The fiber diameters were estimated from SEM images taken at different areas of the same sample. In table 6.1 the results for the resonators depicted in Fig. 6.6 (Res 1) and Fig. 6.7 (Res 2) are listed. For both resonators the measured resonator length and the calculated one are in good agreement, especially when considering the fact that the photograph of the resonator is a 2D projection of an actual three-dimensional object. These results further prove that the lasing emission originates from the random loop resonators.

Table 6.1: Comparison of calculated resonator lengths using the free spectral range and the measured lengths obtained from photographs of the resonators. Both values are in good agreement, the smaller value for the measured length can be explained by the fact that a 2D projection of the resonator is analyzed leading to an underestimation of the *real* length.

	Diameter range (µm)	Calculated length (µm)	Measured length (µm)
Res 1	0.90 - 1.10	408 - 414	392
Res 2	0.82 - 1.02	1166 - 1186	1060

6.3.3 Simulations of the Coupling Region

In the region where the fiber runs in parallel with itself the propagating mode couples from one part of the fiber to the other. The mode propagation in parallel running fibers can be described by the theory of a directional coupler. For two parallel fibers a symmetric and an anti-symmetric mode are the solutions of Maxwell's equations [211]. In Fig. 6.9 (a) the electric field distribution obtained with FEM simulations of these modes is illustrated. A mode propagating in one of the fibers is described as a superposition of the symmetric and the anti-symmetric mode. As the symmetric and anti-symmetric mode have different effective refractive indices a phase shift between these two modes arises when propagating along the fibers. When the phase shift is π the power has been completely transferred from one fiber to the other. This means that the power of the propagating mode is transferred periodically back and forth between the two fibers in dependence of the traveled distance. The coupling coefficient k describes the portion of transferred power in dependence of the coupling length L_c [211]:

$$k = \sin^2\left(\frac{\pi \Delta n_\mathrm{eff} L_\mathrm{c}}{\lambda}\right) \tag{6.2}$$

Here, Δn_eff is the difference of the effective refractive indices of the symmetric and anti-symmetric mode. In Fig. 6.9 (b) the difference of the effective refractive indices of the symmetric and anti-symmetric mode is plotted for different fiber diameters and TE and TM polarization, respectively.

By exponentially extrapolating the data for the difference in effective refractive index the coupling constant k was calculated for different diameters d and coupling lengths L_c. For the spectral region with lasing emission the coupling constant is almost constant for different wavelength. Simulation results for the coupling coefficient are shown in Fig. 6.9 (c) and (d). For Res 1 a mean fiber diameter of 1 µm was estimated from SEM images taken from that sample. When inserting the measured coupling

length of 73 µm for the TE mode a coupling coefficient of $k = 0.6$ is obtained. The result that not all the power is transferred agrees well with the fact that the lasing modes are also observed in adjacent fiber parts which do not belong to the resonator loop itself (compare Fig. 6.6, position 7). For Res 2 (compare Fig. 6.7) a coupling length of 44 µm is measured and SEM images of the same sample yield a mean fiber diameter of 0.92 µm. Calculating the coupling coefficient for these values yields $k \approx 0.9$. However, as the fiber diameter distribution exhibits a standard deviation of approximately 10% and is not measured directly at the investigated resonators, the real coupling coefficient will probably deviate from the calculated values. For a more accurate quantitative analysis instead of using random resonators one would have to fabricate resonator structures on purpose with known coupling length L_c and diameter d, e.g., with near field electrospinning and investigate those in detail. The simulations presented in this section can serve as design guide in order to obtain resonators with high coupling coefficients. As the quality factor is proportional to the coupling coefficient high-Q resonators with low lasing threshold can be designed [117].

6.4 Summary and Conclusions

Electrospun fibers can be fabricated with a simple technique that allows the use of many different materials hence providing flexibility. Optical properties can be easily tuned by using different gain materials or varying the refractive index. The PL-spectra of PMMA fiber networks doped with RhG6 or PM597 were analyzed and measurements on lasing thresholds were presented. Although the thresholds vary for each resonator, in general fibers doped with PM597 exhibit lower lasing thresholds than those doped with RhG6.

By using spatially resolved spectroscopy random resonators were identified as the origin of lasing emission. For this the emission light was assigned to the corresponding fiber and the fibers with lasing emission were tracked. Fibers arranged in loops and forming closed optical paths by overlapping with itself for a certain distance provide the required feedback for lasing emission. A quantitative analysis of the emission spectra of the random resonators shows good agreement between the measured resonator length and the length calculated from the free spectral range. The coupling of light in two parallel running fibers can be described by the theory of directional couplers. In order to obtain the effective refractive indices required to calculate the coupling coefficient FEM simulations were performed. The coupling coefficient was determined for different coupling lengths and fiber diameters.

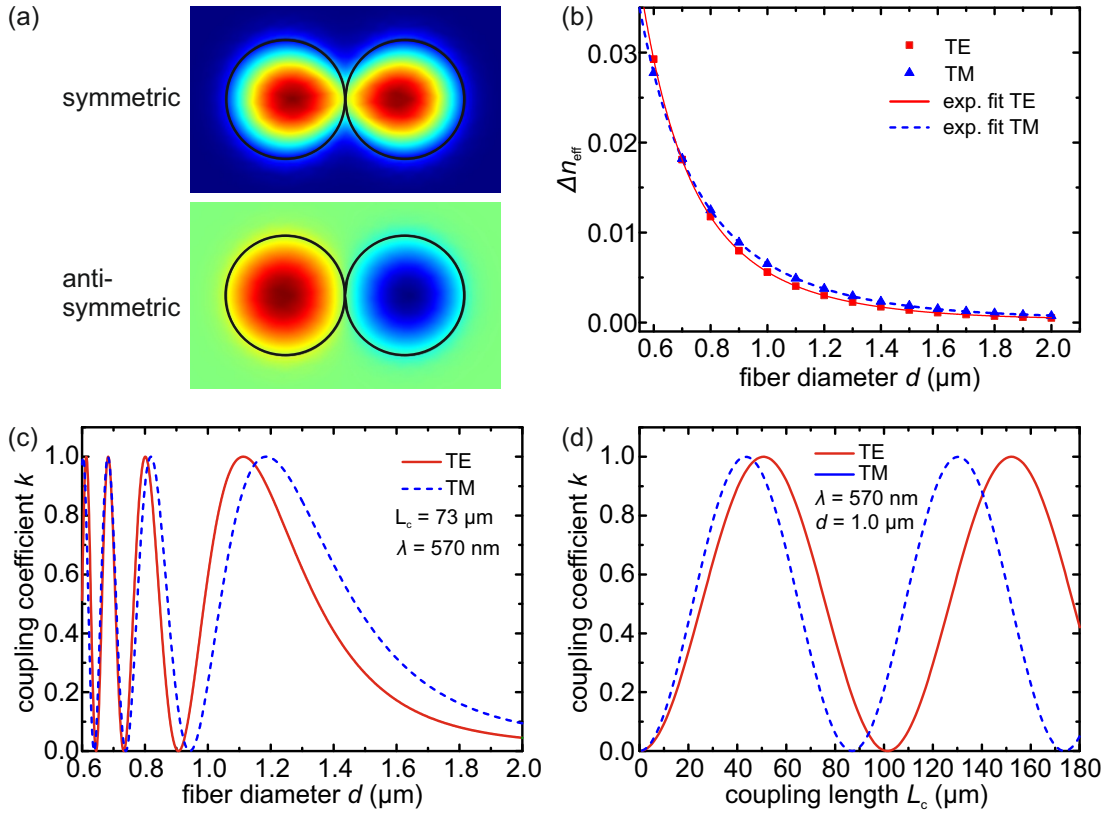

Figure 6.9: Simulation results of the coupling region. (a) Electric field distribution of a symmetric and anti-symmetric mode in parallel fibers with a diameter of $d = 1\,\mu m$. (b) Difference in effective refractive index Δn_{eff} between the symmetric and anti-symmetric mode for varying fiber diameters. (c) and (d) Coupling coefficient k for a constant coupling length L_c and varying fiber diameter d and vice versa. Adapted from [132].

The simulations presented in the last part of this chapter can be used to optimize the fabrication of resonators. Cavities with high coupling coefficient and hence high Q-factors can be fabricated, e.g., by using near-field electrospinning where the geometry of the deposited fibers can be precisely controlled. In the next chapter applications of electrospun fibers and results obtained on sensing will be presented.

Chapter 7

Optical Sensing with Polymer Fiber Networks

Possible fields of applications of electrospun fibers include photonics, sensorics, catalysis or medicine and pharmacy [212]. In these areas the fibers are used as, e.g., broadband or laser light sources [132, 189, 191], scaffolds for tissue engineering [213] or drug release systems [214]. For sensing applications electrospun fibers are promising candidates as they exhibit high surface to volume ratios. In terms of optical sensing usually electrospun light-emitting fibers are used and the luminescence intensity serves as sensor signal to detect target molecules which induce quenching. Successful detection of several metal ions [215], explosive compounds [216] and different biomolecules [217, 218] was demonstrated by incorporating different light-emitting materials in electrospun fibers.

In this work a different approach was chosen and the spectral position of the lasing modes is used as sensor signal as it is also done for the WGM lasers (see chapter 4 and 5). An advantage of this method is that the signal is independent of background light. The dye-doped polymer fiber networks were investigated as sensors for different vapors and as sensors in aqueous environment and for both sensing was demonstrated successfully.

In the first part of this chapter the mechanism of vapor sensing is explained before results on the detection of vapors of water, ethanol, methanol and ethanol–methanol mixtures are presented and discussed. It will be shown that the temporal evolution of the lasing mode shift is different for ethanol and methanol since they exhibit different diffusion coefficients in PMMA. In the second part of this chapter results on the performance of the fiber networks in aqueous environment are presented and their suitability as sensors in water is demonstrated via bulk refractive index sensitivity

measurements. Since PM597-doped fiber networks exhibit lower lasing thresholds than their Rh6G-doped counterparts the sensing measurements were performed with PM597-doped fibers.

7.1 Sensing of Different Vapors

Many polymers exhibit so-called "polymer swelling" when they are exposed to analytes [219]. The expansion of the polymer can be exploited to deform an optical cavity. This and the change of the refractive index of the polymer upon absorption of analyte molecules change the optical path length of the cavity and hence lead to a spectral shift of the resonance. In literature several approaches based on different resonators were successfully implemented. St.-Gelais *et al.* used a deformable Fabry-Pérot interferometer which was filled with the polymer polydimethylsiloxane (PDMS) to detect m-xylene and cyclohexane by tracking the spectral position of the transmission signal [220]. Smith *et al.* coated a photonic crystal with polysterene (PS) to enhance the shift of the resonance when the photonic crystal is exposed to ethanol vapor [221]. Convertino *et al.* fabricated polymer-based distributed Bragg reflectors where swelling of the polymers causes the reflectance spectrum to shift to different wavelengths [222]. Further approaches and examples can be found in [223–225].

In the approach presented in this work the resonators itself are made out of the polymer providing the advantage that fabrication is simple and basically consists of a single step. The fact that a variety of polymers can be used for electrospinning is important when thinking of sensor arrays in which the individual sensors are sensitive towards different analytes. For the dye-doped electrospun polymer fiber networks the vapor sensing principle will be demonstrated through detection of light alcohols and water vapor.

Preliminary measurements on sensing with electrospun fibers have been conducted during the Master's thesis of Minh Tran [226] and the Bachelor's thesis of Pascal Kiefer [227]. The results presented in this section have partly been published in [228] and achieved during the Bachelor's thesis of Felix Friedrich [229].

7.1.1 Mechanism of Vapor Sensing

In this work the spectral position of the lasing peaks is used as sensor signal. Once the polymer fiber networks are exposed to alcohol or water vapor, the polymer expands and the ring resonators change their optical path length $L \cdot n_{\text{eff}}$ leading to

a shift of the resonance wavelength λ_0:

$$L \cdot n_{\text{eff}} = m \cdot \lambda_0. \tag{7.1}$$

The integer m denotes the number of electric field maxima along the ring resonator. As obvious from this resonance condition changes of both the resonator length L and the effective refractive index n_{eff} contribute to the wavelength shift. As discussed in the previous chapter the effective refractive index depends on the refractive index of the PMMA n_{PMMA} and the fiber diameter d (compare Fig. 6.8). In the following the contributions of the different origins to the total shift of the lasing modes will be determined after a brief description on diffusion in polymers is given.

Diffusion in Polymers

The swelling of polymers when exposed to solvent vapors is caused by solvent molecules diffusing into the polymer matrix. In this paragraph a brief introduction to diffusion in glassy polymers is given. First the ideas of Fickian diffusion and Case II transport are introduced and a description including both processes is presented. Afterwards the diffusion of light alcohols into polymers is discussed.

In the simplest case the equilibrium concentration c of a solvent in a polymer matrix is given by Henry's law

$$c = kp, \tag{7.2}$$

where k denotes the solubility or partition coefficient of the solvent–polymer system which states how miscible the substances are and p is the partial pressure of the solvent at the interface.

For describing the kinetics of diffusion different theories have been proposed, with Fickian diffusion and Case II transport being the most prominent ones. Fickian diffusion is described by Fick's second law

$$\partial_t c = \partial_x (D \partial_x c), \tag{7.3}$$

with D being the diffusion coefficient [230], which usually depends on the concentration c. The concentration gradient $\partial_x c$ of the analyte in the polymer decreases over time until in equilibrium the analyte concentration is the same in the complete polymer. Fickian diffusion occurs when the relaxation of stress in the polymer chains which is introduced by the solvent molecules is faster than the movement of the solvent molecules. For short time-scales the kinetics follow $M_t \propto t^{1/2}$, where M_t is the absorbed mass of the solvent at time t.

For Case II transport the solvent molecules diffusing through the polymer form a sharp front that moves at a velocity v. In this case diffusion is fast compared to

relaxation of the polymer chains. The velocity of the front depends on the viscous resistance of the polymer to deform [231]. For a thin polymer film the kinetics of Case II diffusion follows $M_t \propto t$. A clear distinction between Fickian diffusion and Case II transport is not always possible since also intermediate processes occur. Thomas *et al.* defined different regimes based on the diffusion coefficients and the viscosity [231]. Furthermore, Wang *et al.* presented a generalized diffusion equation which describes combinations of Fickian diffusion and Case II transport [232]:

$$\partial_t c = \partial_x (D\partial_x c - vc). \tag{7.4}$$

Again, v is the velocity of the sharp front and is interpreted as stress coefficient. For a film with thickness l which is exposed to solvent vapor from both sides Eq. 7.4 is solved by

$$\frac{M_t}{M_\infty} = 1 - \sum_{n=1}^{\infty} \underbrace{\frac{4n^2\pi^2\left(1-(-1)^n \cosh\left(\frac{vl}{2D}\right)\right)}{\left(\left(\frac{vl}{2D}\right)^2 + (n\pi)^2\right)^2}}_{=:B_\mathrm{n}} \cdot \exp\Bigg(-\underbrace{\left(\frac{n^2\pi^2 D}{l^2} + \frac{v^2}{4D}\right)}_{=:t_n} t\Bigg), \tag{7.5}$$

where M_∞ is the mass increase at equilibrium. For long times t only the first addend in Eq. 7.4 is important and the solution of Eq. 7.4 is given by a simple limited exponential growth function:

$$\frac{M_t}{M_\infty} = 1 - B_1 \mathrm{e}^{-t/\tau} \tag{7.6}$$

The parameters B_1 and τ depend on the diffusion coefficient D, the velocity v and the film thickness l. When entirely Fickian (Case II) diffusion should be described v (D) needs to be set to zero. The ratio of the diffusion coefficient to the velocity determines whether the process is rather Fickian or Case II. The higher the diffusion constant the more Fickian is the process. Since many intermediate processes exist and both the diffusion constant and the velocity depend on concentration and temperature [231] it is not possible to clearly assign either Fickian or Case II diffusion to a specific polymer–solvent combination [233].

Sfirakis *et al.* reported Case II transport for ethanol and methanol vapors in PMMA at room temperature when PMMA was exposed to saturated vapor [234]. In contrast to that Papanu *et al.* observed Fickian-like kinetics for the diffusion of methanol at room temperature when investigating PMMA films with a thickness of 1–2 µm. For ethanol the diffusion kinetics were rather Case II when measured at 40 °C. Papanu *et al.* explain the Fickian diffusion behaviour for methanol with thin-film effects: The initial uptake could be Fickian and the sharp front cannot be established for thin samples [233, 235]. Furthermore, it is known that with Case II diffusion a

Fickian precursor precedes the front which attenuates the sharp concentration gradient [236]. For thin samples, e.g., a thin polymer film, a precursor of few hundreds of nanometers would already expand over the whole sample thus not allowing Case II transport.

Since in the vapor sensing experiments conducted in this work small ethanol and methanol vapor concentrations are used it seems intuitive that stress effects in the polymer are rather small. This and the fact that fibers with diameters of 1 µm or less are used indicate that rather Fickian diffusion occurs in the polymer fiber networks. A clear assignment of the diffusion process requires further investigations but a detailed study of diffusion kinetics is beyond the scope of this work.

Analytical Model to Predict the Shifts of the Lasing Modes

In order to predict the shift of the lasing modes upon exposure of the fiber networks to ethanol or methanol vapor a simple analytical model was developed. The volume change of the PMMA $V \rightarrow V' = \alpha V$, which occurs upon exposure to vapors, is transferred to the cylindric fiber geometry. For the fibers isotropic swelling is assumed. The increase of the length $L \rightarrow L' = \gamma L$ and the diameter $d \rightarrow d' = \gamma d$ of a cylindrical fiber is determined via

$$\alpha V = V' = \pi L'(d'/2)^2 = \pi \cdot \gamma L \cdot (\gamma d/2)^2 = \gamma^3 V. \tag{7.7}$$

Besides expansion of the fibers the analyte molecules diffusing into the polymer also change the refractive index of the PMMA $n_{\mathrm{PMMA}} \rightarrow n'_{\mathrm{PMMA}}$. The effective refractive index n_{eff} which is crucial for the optical path length depends on both the refractive index of the PMMA and the fiber diameter. An increase of the refractive index of PMMA can occur when the solvent molecules fill holes in the polymer matrix. With finite element simulations performed with COMSOL we determined the dependence of the effective refractive index on the fiber diameter and on the refractive index of the PMMA. The former dependence is depicted in Fig. 6.8 and the latter one turned out to be linear.

When changes in length, diameter and refractive index of the PMMA upon exposure to solvent vapors are known, the expected shift of lasing modes can be determined. Starting from the resonance condition given in Eq. 7.1 one obtains:

$$\frac{\Delta\lambda}{\lambda} = \frac{\Delta L}{L} + \frac{\Delta n_{\mathrm{eff}}}{n_{\mathrm{eff}}} = \gamma + \frac{n_{\mathrm{eff}}(\gamma d, n'_{\mathrm{PMMA}})}{n_{\mathrm{eff}}(d, n_{\mathrm{PMMA}})} - 2 \tag{7.8}$$

In order to figure out whether the shift of the lasing modes is caused by changes of the resonator length L or changes of the effective refractive index n_{eff} or both ellipsometry measurements on PMMA films were conducted. PMMA films of approximately

300 nm thickness were spin-coated on silicon wafers and both the refractive index of the PMMA n_{PMMA} and the layer thickness were determined by ellipsometry when the film is exposed to ethanol and methanol vapor. Since the film is fixed to the substrate on one side and the lateral extent of the film exceeds the thickness by orders of magnitude we assume that the complete volume change occurs as thickness change. To adjust the vapor concentration a vapor mixing system was developed during the Bachelor's thesis of Felix Friedrich [229]– a description can be found in appendix A. The ellipsometry measurements were performed and evaluated by Fabrice Laye at the Institute of Functional Interfaces (IFG, KIT).

Predictions on Shifts of the Lasing Modes Based on Ellipsometry Measurements

From ellipsometry measurements information on changes in volume and refractive index of PMMA upon exposure to alcohol vapors is gained. Using Eq. 7.7 and Eq. 7.8 this information is transferred to the fiber geometry and predictions on the shift itself but also on its origin are obtained. When the data from ellipsometry measurements (which were conducted at concentrations of 15000 ppm and 32000 ppm for ethanol and methanol, respectively) were transferred to other concentrations a linear dependence of expansion and change of refractive index on concentration was assumed.

In Fig. 7.1 the predicted shifts of the lasing modes for different ethanol and methanol concentrations is depicted and broken into the different contributions. The bar plots show that the shift of the lasing modes $\Delta\lambda_0$ mainly originates from length changes ΔL (green) and an increase of the refractive index of PMMA which leads to an increase of n_{eff} (blue). The lateral expansion of the fibers which results in an enhanced fiber diameter and hence also in an increased effective refractive index (orange) only plays a minor role. For fiber diameters of between $d = 0.6\,\mu\mathrm{m}$ and $d = 1.2\,\mu\mathrm{m}$ the dependence of the effective refractive index on the refractive index of PMMA is almost the same. This means that the sensitivity is not influenced by slight fluctuations of the fiber diameter due to the fabrication process.

Besides analyzing the different contributions to the peak shift also the sensitivity of the fibers towards ethanol or methanol vapor is predicted. Assuming a fiber diameter of 0.9 µm and a wavelength of 590 nm yields an expected sensitivity of $S_{\mathrm{EtOH}} = 0.33\,\mathrm{pm/ppm}$ for ethanol while for methanol a lower sensitivity of $S_{\mathrm{MeOH}} = 0.23\,\mathrm{pm/ppm}$ is predicted.

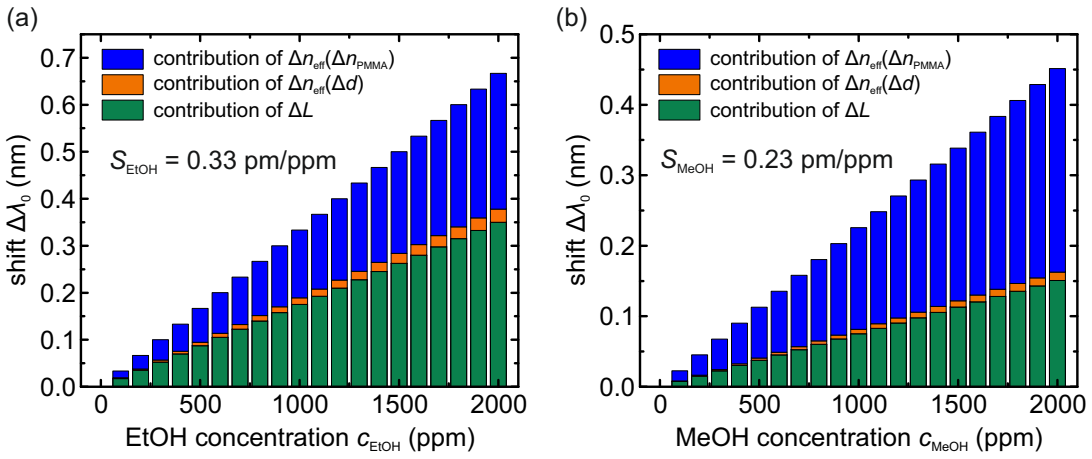

Figure 7.1: Expectations of the lasing peak shifts when polymer fibers are exposed to ethanol (EtOH) and methanol (MeOH) vapor. The totel shift can be decomposed into contributions from changes of the resonator length ΔL (green), contributions from changes of the effective refractive index caused by changes of the fiber diameter (orange) and contributions from changes of the effective refractive index caused by changes of the refractive index of PMMA (blue). A fiber diameter of $d = 0.9\,\mu m$ and a resonance wavelength of $\lambda_0 = 590\,nm$ was assumed for the calculations. Adapted from [228].

7.1.2 Temperature Dependence and Operational Lifetime of Dye-Doped Polymer Fibers

When thinking of possible applications of the dye-doped polymer fiber networks the temperature dependence and the operational lifetime of the lasing modes are important aspects which need to be investigated.

The spectral position of the lasing modes is influenced by temperature changes since the optical path length of a cavity depends on temperature. In the simplest case two factors need to be considered: The temperature dependence of the refractive index of PMMA which is given by the thermo-optic coefficient κ and the expansion of PMMA upon changing temperature which is described by the thermal expansion coefficient α. Both coefficients were determined for PMMA by performing ellipsometry measurements on thin PMMA films, yielding $\kappa = -3.2 \times 10^{-4}\,/K$ and $\alpha = 4.2 \times 10^{-5}\,/K$ for a temperature range from 26 °C to 30 °C. The negative thermo-optic coefficient will cause a blue-shift of the lasing mode with increasing temperature whereas expansion causes a red-shift. The measured thermo-optic coefficient of PMMA is almost a factor of three higher than the value of $\kappa = -1.3 \times 10^{-4}\,/K$ reported in literature [237] and the expansion coefficient also deviates by a factor of almost two. However, in [237] the temperature dependence was investigated from 25 °C

to 100 °C in steps of 20 K, so a stronger temperature dependence for low temperatures would not have been noticed. Furthermore, the PMMA used in literature has a different molecular weight which can also lead to deviations. Compared to silica ($\kappa = 0.55 \times 10^{-6}$ /K [238]) the thermo-optic coefficient of PMMA is more than two orders of magnitude larger, making polymeric resonators more sensitive to temperature changes.

With the following equation the expected shift of the resonant modes upon a change in temperature can be calculated [238]:

$$\Delta\lambda_0 = \lambda_0 \left(\alpha + \frac{dn_{\text{eff}}/dT}{n_{\text{eff}}} \right) \Delta T \tag{7.9}$$

Here, λ_0 denotes the resonance wavelength in the cavity without temperature change ΔT. By performing finite element simulations a linear dependence of the effective refractive index n_{eff} on the refractive index of the PMMA n_{PMMA} was found. With this relation and Eq. 7.9 a spectral shift of -0.11 nm/K for a resonance wavelength of $\lambda = 590$ nm is expected. The calculation was done for fiber diameters between 0.6 µm and 1.3 µm revealing a negligible dependence of the shift on the fiber diameter. Since the thermo-optic coefficient of air is two orders of magnitude smaller than that of PMMA and most of the energy of the resonant modes is guided inside the polymer fibers influences from changes of the refractive index of air were neglected.

The resulting blue-shift of the lasing modes when considering both changes of the refractive index and expansion of the PMMA is due to the large negative thermo-optic coefficient of PMMA. The blue-shift caused by changes of the refractive index of PMMA exceeds the red-shift due to thermal expansion by almost a factor of five.

To investigate the temperature dependence of the lasing modes experimentally, the polymer fiber samples were mounted on a Peltier-element. Its temperature was regulated with a proportional-integral-derivative (PID) controller and a resistive thermometer (PT100) to an accuracy of $\Delta T = 0.1$ K. The temperature dependence of the lasing modes of the polymer fiber networks was monitored for increasing and decreasing temperature and is depicted in Fig. 7.2. The slight deviations between the measurements for increasing and decreasing temperature arise from bleaching of dye molecules and a blue-shift going along with it [239]. When taking the average of the two measurements a temperature dependence of -0.115 nm/K for temperatures between 25 °C and 30 °C is obtained and effects due to bleaching are minimized in that way. For temperatures exceeding 30 °C the temperature dependence of the lasing modes is lower, but normally only slight temperature variations occur during sensing measurements so this temperature regime was not evaluated.

The measured temperature dependence of lasing modes (with $\lambda_0 \approx 590$ nm) of the polymeric fibers agrees well with the expected value of -0.11 nm/K calculated above.

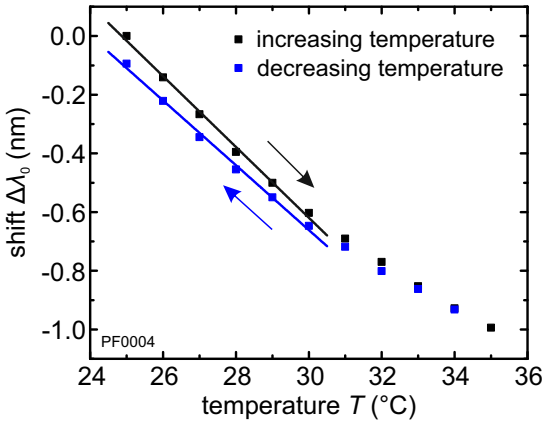

Figure 7.2: Temperature dependence of the spectral position of the lasing modes in air for resonance wavelengths of approximately 590 nm. The blue-shift of the lasing modes upon increasing temperature arises from the negative thermo-optic coefficient. Deviations between the measurements for increasing and decreasing temperature originate from the additional blue-shift due to bleaching of dye molecules [239]. By using the average of both measurements bleaching effects are minimized and a temperature dependence of 0.115 nm/K is obtained. Adapted from [227].

Disturbing influences from temperature during sensing experiments can be reduced by using temperature stabilisation with a Peltier-element which was done in the following experiments.

Another important aspect in terms of application is the operational lifetime of the lasing modes. Photodegradation of dye molecules is one central issue in solid-state dye-lasers (compare section 3.2 and [127, 240]). In order to investigate the operational lifetime of the lasing modes the polymer fiber networks were optically pumped well above lasing threshold with an excitation energy of approximately 440 µJ/cm^2 at a repetition rate of 50 Hz. The emission spectrum as a function of pump pulses is plotted in Fig. 7.3. The slight blue-shift of the lasing modes arises from the bleaching of dye molecules which leads to a decrease of the refractive index [239]. The intensity of the lasing modes decreases during the measurement and some of the lasing modes disappear but some modes are still present after 15×10^4 pump pulses. Assuming a repetition rate of 20 Hz, which is usually used, this yields a measurement time exceeding two hours which is sufficient for most sensing experiments. To further extend the measurement time non-permanent excitation can be used.

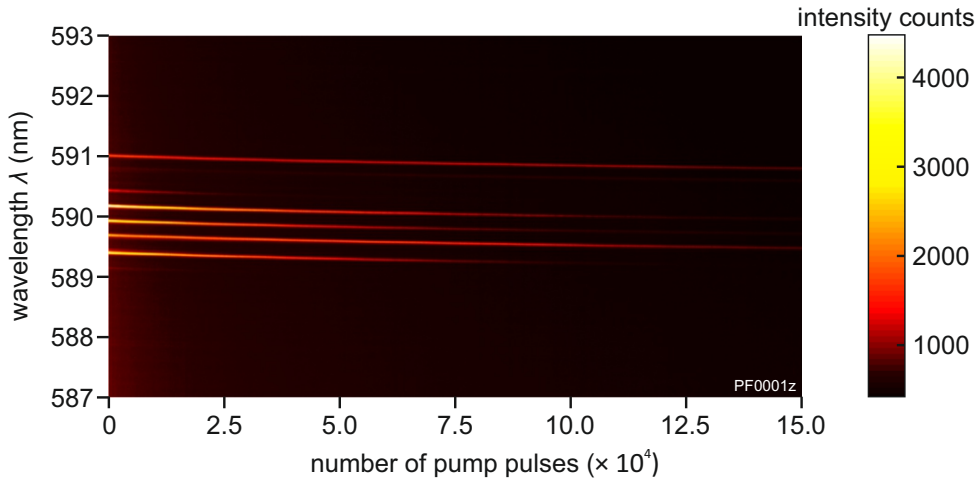

Figure 7.3: Operational lifetime of dye-doped polymer fibers. The fibers were exposed to 15×10^4 excitation pulses at an energy of $440\,\mu J/cm^2$ and a repetition rate of 50 Hz. During the measurement the intensity of the lasing peaks is reduced but some of the modes are present for more than 15×10^4 pulses. The blue-shift of the modes is due to bleaching of dye molecules and the refractive index change going along with it [239].

7.1.3 Detection of Water Vapor

Since PMMA exhibits swelling when placed in aqueous environment it is expected that also changes in the relative humidity of the surrounding lead to expansion of PMMA. The resulting change of the optical path length of the resonators induces shifts of the lasing modes. To assess the dependence of the spectral position of the lasing modes on the relative humidity experimentally one of the gas washing bottles in the vapor mixing system was filled with water. Furthermore, a closed sample chamber with a transparent lid was built which can easily be integrated in the µ-PL-setup.

The spectral position of the lasing modes was tracked over time for different concentrations of water vapor. The peak position was tracked by fitting a Lorentzian function to the data. The resulting measurement curves are depicted in Fig. 7.4 (a). As soon as the fibers are exposed to water vapor the lasing modes exhibit a red-shift which saturates after few minutes. A sum of two exponential functions

$$\Delta\lambda_0(t) = A_1(1 - \exp(-t/\tau_1)) + A_2(1 - \exp(-t/\tau_2)) \tag{7.10}$$

was used to fit the data. A fast time component of $t_1 = 33 \pm 11\,s$ and a slow component of $t_2 = 300 \pm 190\,s$ are obtained. No trend of the response time with respect to the vapor concentration is perceptible. The variation of the response times might arise from different fiber diameters. The necessity of two exponential functions

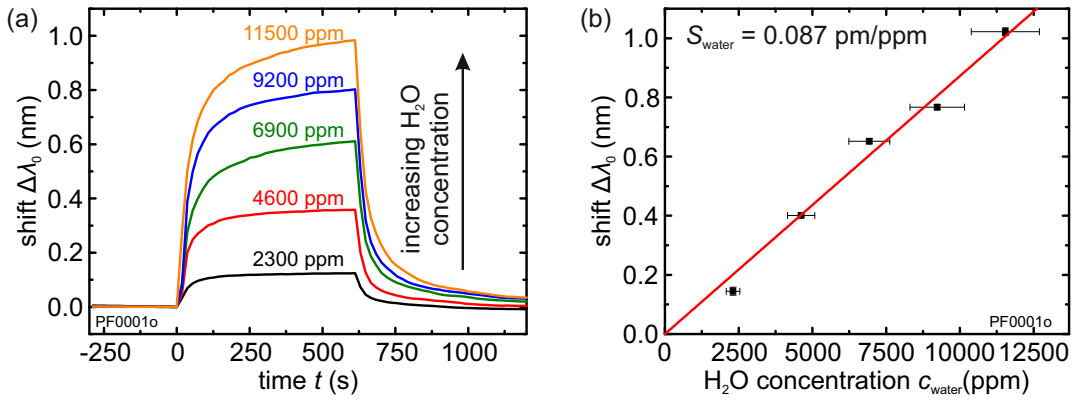

Figure 7.4: Detection of relative humidity changes. (a) The spectral position of the lasing modes is monitored over time for different concentrations. A sum of two exponential functions can be fitted to the data indicating that two process contribute to the swelling. (b) The shift in saturation depends linearly on the water vapor concentration. The fibers show a sensitivity of $S_{\mathrm{water}} = 0.087\,\mathrm{pm/ppm}$. Adapted from [229].

for fitting of the data is a hint that two processes are involved when water penetrates PMMA. In [241], Mathhes considered that besides diffusion of water molecules into the polymer also the formation of water clusters in the polymer matrix might occur. With the given data the two time constants cannot be attributed to the processes, however, this is also beyond the scope of this work.

When the shift in saturation is plotted versus the water vapor concentration as it is done in Fig. 7.4 (b) a linear dependence is obtained for the investigated concentration range. The polymer fiber networks show a sensitivity to water vapor of $S_{\mathrm{water}} = 0.087\,\mathrm{pm/ppm}$.

The fact that the lasing modes of the PMMA fiber networks are sensitive to water vapor on the one hand enables them to be used as humidity sensor but on the other hand has the disadvantage that water vapor can disturb the actual signal. When the humidity changes are known, e.g., when measured with a humidity sensor, the signal can be corrected by the calibration curve shown in Fig. 7.4 when assuming that other diffusion processes are independent of humidity. To avoid disturbing influences from humidity all experiments on sensing have been conducted in a nitrogen atmosphere with the addition of the analyte vapors.

7.1.4 Detection of Light Alcohol Vapors

To investigate the performance of electrospun fiber networks as vapor sensors the light alcohols ethanol and methanol have been chosen as analytes. In the following the results obtained on ethanol and methanol sensing are presented before experimental data on detection of ethanol–methanol mixtures is presented and analyzed.

Detection of Ethanol Vapor
Ethanol sensing experiments were conducted in the same way as the detection of water vapor. By using the vapor mixing system the ethanol concentration was adjusted to the desired values. The total flow was kept at 1.5 L/min for all measurements. To maintain a constant temperature the sample was mounted on a Peltier-element which was regulated with a PID controller and a PT100 thermoresistor.

During the measurement spectra were acquired every nine seconds to reduce the illumination time and bleaching effects of the dye molecules. The spectral position of the lasing modes was determined by fitting a Lorentzian function to the lasing peaks. At the beginning of each measurement the sample was exposed to pure nitrogen resulting in a constant spectral position of the lasing modes. When the fibers are exposed to ethanol vapor they start to swell and the lasing modes exhibit a red-shift consequently. Fig. 7.5 (a) shows two spectra – one before exposure to ethanol (black curve) and one after 117 s of exposure to ethanol (red curve), clearly visualizing the red-shift of the lasing modes. In Fig. 7.5 (b) typical examples of time-resolved measurements at different ethanol concentrations are depicted. As expected, for higher ethanol concentrations larger shifts are observed. For all measurements the shift $\Delta\lambda_0$ approaches saturation after several thousands of seconds (more than 90 minutes). The release of ethanol was not monitored to avoid prolonged measurement times. However, for an exposure of the fibers to ethanol vapor for approximately 30 minutes, the release was monitored and the lasing peaks shift back to their original spectral position, demonstrating reversibility of the process.

According to the kinetics of diffusion a limited exponential growth function should represent the data and enable quantitative analysis. Since the initial shift should be zero the fit function was required to fulfil this condition by setting $\Delta\lambda_0(t = 0) = 0$, yielding:

$$\Delta\lambda_0(t) = A_{\mathrm{EtOH}} \left(1 - \exp\left(-\frac{t}{\tau_{\mathrm{EtOH}}}\right)\right). \tag{7.11}$$

The parameter A_{EtOH} denotes the shift in saturation and t_{EtOH} denotes the time constant which will be referred to as saturation time in the following. Fig. 7.5 (c) depicts the data of a typical measurement and the corresponding fit representing the data. For the investigated concentration range no dependence of the saturation

time on the vapor concentration was observed. On average a saturation time of $\tau_{\mathrm{EtOH}} = 2400 \pm 500\,\mathrm{s}$ was measured. The deviation in the saturation time can result from different fiber diameters since sensing experiments were conducted at different sample positions. The shifts in saturation A_{EtOH} for different concentrations are plotted in Fig. 7.5 (d). Multiple measurements were conducted for each concentration and the average shift was calculated. The uncertainty in the vapor concentration due to the mixing system was estimated to be 15%. The wavelength of the tracked lasing modes was always around 590 nm resulting in a negligible wavelength dependence of the shifts. For concentrations below 800 ppm the shift in saturation A_{EtOH} depends linearly on the concentration; for higher concentrations the shift A_{EtOH} approaches saturation. In the linear regime the sensitivity of the fibers to ethanol is determined to be $S_{\mathrm{EtOH}} = 1.01\,\mathrm{pm/ppm}$. Concerning noise, thermal fluctuations which lead to a shift of -115 pm/K as discussed previously are the major contribution and other noise sources are negligible. With the Peltier-element temperature is controlled to a precision of 0.1 K, which leads to noise of $\sigma_{\mathrm{therm}} = 11.5\,\mathrm{pm}$ and a resolution of $R = 3\sigma_{\mathrm{therm}} = 34.5\,\mathrm{pm}$ resulting in an approximation of the detection limit of

$$DL_{\mathrm{EtOH}} \approx 35\,\mathrm{ppm}. \tag{7.12}$$

This value is comparable to the detection limit of other optical ethanol sensors reported in literature, e.g., Smith *et al.* achieved a response threshold of 50 ppm ethanol [221].

Detection of Methanol Vapor

The methanol (MeOH) sensing experiments were conducted in the same way as the ethanol detection measurements. Fig. 7.6 (a) depicts time-resolved curves for different methanol concentrations. As soon as methanol vapor reaches the polymer fiber networks the lasing modes show a shift to larger wavelengths which saturates within 300 seconds. When the sample chamber is purged with nitrogen the methanol in the polymer fibers is released and the lasing peaks shift back to their original position. Hence, within our measurement accuracy the process of methanol uptake by the fibers is reversible.

As with ethanol a limited exponential growth can be fitted to the data to extract the shift in saturation A_{MeOH} and the saturation time τ_{MeOH} to describe the shift over time: $\Delta\lambda_0(t) = A_{\mathrm{MeOH}}\,(1 - \exp\,(-t/\tau_{\mathrm{MeOH}}))$. For methanol saturation times of $\tau_{\mathrm{MeOH}} = 32 \pm 5\,\mathrm{s}$ are obtained. For the investigated concentration range the shift in saturation A_{MeOH} depends linearly on the concentration as can be seen in Fig. 7.6 (b). A sensitivity of $S_{\mathrm{MeOH}} = 0.26\,\mathrm{pm/ppm}$ is obtained from a linear fit to

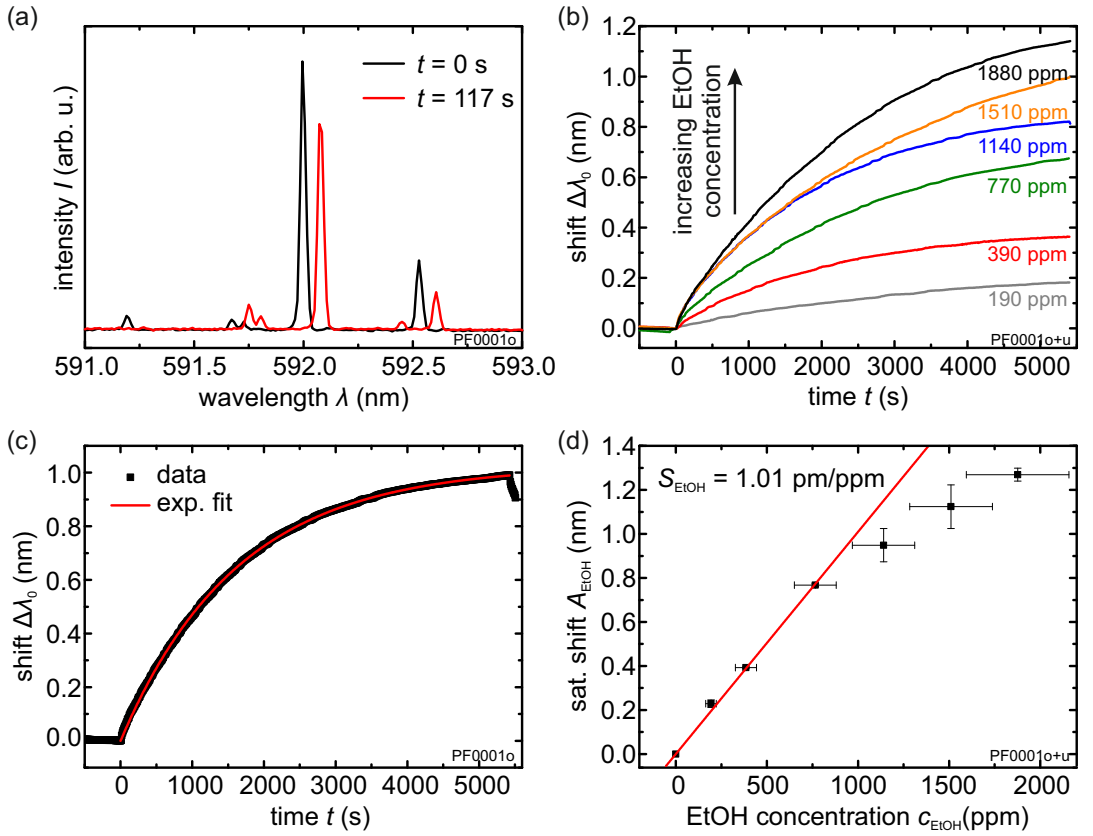

Figure 7.5: Detection of ethanol vapor. The lasing modes in the spectra exhibit a red-shift when the fibers are exposed to ethanol vapor. (a) Spectrum with lasing peaks taken before exposure to ethanol (black) and after the fibers were exposed for 117 s (red). (b) Time-resolved signal for different ethanol concentrations. (c) Time-resolved spectral shift of the lasing peaks. Data points can be fitted with a limited exponential growth, yielding the shift in saturation A_{EtOH} and the saturation time τ_{EtOH}. (d) Average shift in saturation from different measurements and lasing peaks for different ethanol concentrations. For concentrations below 800 ppm a linear correlation is observed, resulting in a sensitivity of $S_{\mathrm{EtOH}} = 1.01\,\mathrm{pm/ppm}$. The uncertainty in the vapor concentration due to the mixing system was estimated to be 15%. Adapted from [228].

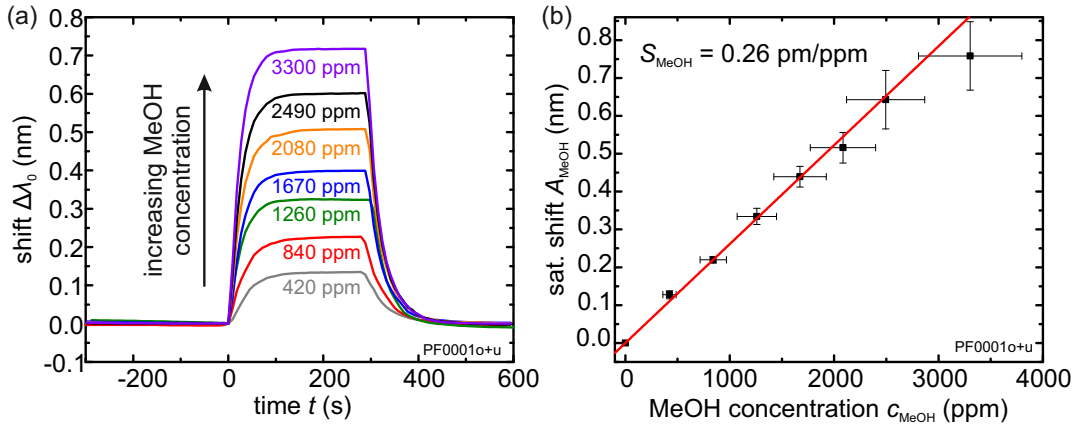

Figure 7.6: Detection of methanol vapor. (a) Time-resolved shift of the lasing modes when the polymer fibers were exposed to different methanol vapor concentrations. As soon as methanol is present in the sample chamber the peaks exhibit a red-shift. When the sample champer is purged with pure nitrogen the lasing modes shift back to their original position demonstrating the reversibility of the swelling process. (b) For the investigated concentration range the shift in saturation A_{MeOH} depends linearly on the methanol vapor concentration and a sensitivity of $S_{\mathrm{MeOH}} = 0.26\,\mathrm{pm/ppm}$ is obtained. Adapted from [228].

the data points which yields a detection limit of

$$DL_{\mathrm{MeOH}} \approx 135\,\mathrm{ppm}. \tag{7.13}$$

Comparison of Ethanol and Methanol Vapor Detectioin

The results for sensing of ethanol and methanol vapor are compared in table 7.1. The sensitivity of the fibers towards ethanol is about a factor of 4 larger than towards methanol. This can be partly attributed to the higher molar volume of ethanol ($V_{\mathrm{m}}^{\mathrm{EtOH}}/V_{\mathrm{m}}^{\mathrm{MeOH}} \approx 1.4$). Furthermore, the solubility parameter δ of ethanol ($\delta_{\mathrm{EtOH}} = 26.0\,(\mathrm{MPa})^{1/2}$) is closer to that of PMMA ($\delta_{\mathrm{PMMA}} = 18.6\,(\mathrm{MPa})^{1/2}$) than the solubility parameter of methanol ($\delta_{\mathrm{MeOH}} = 29.7\,(\mathrm{MPa})^{1/2}$) [242]. The closer the solubility parameters of a solvent and a polymer are, the more soluble is the polymer in the solvent and the other way around [242]. Hence, more ethanol molecules are expected to diffuse into the PMMA matrix than methanol molecules for the same exterior concentration.

For methanol the sensitivity measured with the polymer fiber networks agrees well with the sensitivity prediction based on ellipsometry measurements. For ethanol the measured sensitivity of the fibers is higher than predicted. The main reason for

Table 7.1: Comparison of the results on sensing of ethanol and methanol vapor. The differences in saturation time can be explained by the diffusion coefficients for ethanol and methanol in PMMA.

	Ethanol	Methanol
Saturation time (s)	2400 ± 500	32 ± 5
Diffusion coefficient (cm^2/s) [243]	$\sim 3 \times 10^{-10}$	$\sim 3 \times 10^{-8}$
Predicted sensitivity (pm/ppm)	0.33	0.22
Measured sensitivity (pm/ppm)	1.01	0.26

that is that the shift in saturation A_{EtOH} approaches saturation for higher ethanol concentrations. However, the sensitivity was determined from the linear regime for concentrations below 800 ppm. When considering that the ellipsometry measurements were conducted at a high concentration (15000 ppm) and the results were transferred linearly to lower concentrations it is no surprise that the predicted sensitivity underestimates the measured one. However, the main purpose of the analytical model is not a precise quantitative prediction but to figure out the origin of the shift of the lasing modes. Furthermore, it is possible that the fibers behave differently than bare PMMA films as the polymer chains might be aligned differently. Also the swelling process of the fibers might not be completely isotropic. Still, despite deviations the developed model allows to give a prediction for the order of magnitude of the sensitivity and insights into the origins of the shift.

From table 7.1 it is furthermore evident that the saturation time τ for ethanol is about 75 times longer than for methanol. This difference can be explained when the diffusion coefficients of ethanol and methanol in PMMA are considered. In [243] the diffusion coefficients were determined to be $\sim 3 \times 10^{-10}\,\mathrm{cm}^2/\mathrm{s}$ and $\sim 3 \times 10^{-8}\,\mathrm{cm}^2/\mathrm{s}$ for ethanol and methanol, respectively. Even if the absolute values for the diffusion coefficients in the PMMA fibers might be different the ratio of the coefficients yields an expected ratio of $\tau_{\mathrm{EtOH}}/\tau_{\mathrm{MeOH}} = D_{\mathrm{MeOH}}/D_{\mathrm{EtOH}} = 100$ when Fickian diffusion is assumed. The expected value corresponds well to the experimentally determined ratio of 75.

Differentiation of Ethanol and Methanol Vapors

The saturation times of ethanol and methanol depend on the diffusion coefficient of the solvent and are hence characteristic for the solvent–polymer combination as long as the fiber diameters are comparable. This should enable the identification of alcohols also in mixtures when time-resolved data is analyzed. To figure out whether

the vapor sensor based on electrospun polymer fiber networks is able to distinguish ethanol and methanol, sensing experiments on vapor mixtures were carried out. In Fig. 7.7 a typical time-resolved curve of the shift of the lasing modes $\Delta\lambda_0$ is shown. A sum of two exponentials of the following form is fitted to the data:

$$\Delta\lambda_0(t) = A_1\left(1 - \exp\left(-\frac{t}{\tau_1}\right)\right) + A_2\left(1 - \exp\left(-\frac{t}{\tau_2}\right)\right). \tag{7.14}$$

The fit function contains a slow and a fast component with times τ_1 and τ_2 matching the saturation times of ethanol and methanol. From the corresponding coefficients A_1 and A_2 the shifts in saturation caused by ethanol and methanol can be determined and converted into concentrations via the previously determined sensitivities. Table 7.2 lists the resulting values of three measurements with different concentrations. An allocation of the times τ_1 and τ_2 to the saturation times of ethanol and methanol is possible for all measurements. When comparing the adjusted concentrations with the ones determined from the shift good agreement is found for ethanol, whereas the methanol concentration is overestimated, especially when a higher amount of ethanol is present.

This leads to the assumption that the presence of ethanol increases the methanol uptake by the polymer fibers. Kuhn *et al.* made a similar observation for all-silica decadodecasil crystals, where the presence of water vapor enhanced the absorption of ethanol and methanol [244]. In this case additional calibration would be required to determine also the methanol concentration in mixtures.

In summary, it was shown that dye-doped electrospun fiber networks are suitable as sensors for different vapors. When the time-resolved signal is analyzed distinction between ethanol and methanol and identification of these alcohols is possible. This is significant since especially in the field of gas detection specificity is important but challenging. To further expand and improve the vapor sensing abilities and to reduce disturbances from other external sources such as humidity fluctuations, different polymers, e.g., polysterene (PS), which is insensitive to water vapor, could be used [221].

7.2 Sensing in Aqueous Environment

In the area of biosensing where, e.g., blood or urine samples are analyzed, sensors are usually operated when surrounded by liquids. Sensing with resonators formed by electrospun polymer fibers in aqueous environment works according to the same

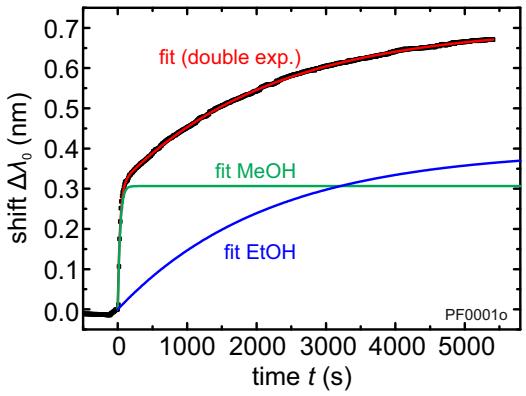

Figure 7.7: Parallel detection of ethanol and methanol vapor. A sum of two limited exponential growth functions represents the data well. The times of the fit function correspond to the saturation times of ethanol and methanol, thus allowing identification of the vapors. Adapted from [228].

Table 7.2: Sensing of ethanol–methanol mixtures. Comparison of expected and measured saturation times and concentrations.

			EtOH	MeOH
	τ_1 (s)	τ_2 (s)	$c_{\text{set}}/c_{\text{meas}}$ (ppm)	$c_{\text{set}}/c_{\text{meas}}$ (ppm)
M1	3160	49	390/360	420/ 440
M2	2170	34	390/390	840/1180
M3	2270	42	770/740	420/ 720

principle as with WGM cavities. The evanescent field of the mode which leaks into the surrounding of the fiber is used to probe the environment. When changes occur, e.g., due to attaching molecules or refractive index changes of the bulk the optical path length of the resonator changes and the resonant modes shift spectrally.

In this section the lasing performance of electrospun polymer fiber networks in aqueous environment was analyzed to figure out whether the fibers can also serve as biosensors. As a proof of principle experiment the bulk refractive index sensitivity of the fibers was measured. Furthermore, the experimental values were compared to simulation data and show good agreement.

7.2.1 Lasing Performance of the Fiber Networks in Aqueous Environment

For application of the polymer fiber networks as sensors in aqueous environment two main criteria need to be fulfilled. In the first place lasing emission must be possible and in the second place the lasing modes need to be stable for a sufficient number of excitation pulses to perform a sensing measurement. The investigations on this topic were performed during the Bachelor's thesis of Max Göhring and the results are presented in the following [245].

For measurements in aqueous environment the electrospun fiber network samples were mounted to a sample chamber which can be filled with liquids. The chamber has a window on the front for optical excitation and read-out. Liquids can be exchanged easily since a tube with a connector for a syringe is connected to the chamber. Fiber networks with dimensions of approximately 1 cm $\times$1 cm on silicon substrates covered with SiO_2 were used. The fiber networks were fixed onto the rims of the substrate with the glue Fixogum (*Marabu*) to ensure that the fibers are not flushed away during rinsing processes. Measurements were conducted with the µ-PL setup presented in section 3.3.1.

Fig. 7.8 shows an input-output curve of the polymer fiber networks in aqueous environment. The lasing threshold determined from the intersection of the two lines fitted to the data is $E_{\text{threshold}} = 5.6\,\text{mJ/cm}^2$. Another measurement of the lasing threshold at a different position yields a similar value of $E_{\text{threshold}} = 5.4\,\text{mJ/cm}^2$. The lasing thresholds are a factor of 6 to 200 higher compared to the values obtained is air. Comparison of single values is again not possible as each of the random resonators is different. However, while in air sample positions with lasing emission were easy to locate this was more difficult in aqueous environment. One explanation is that the lasing thresholds in water exceed the applicable excitation energy per pulse. The coupling coefficient for the same coupling length differs in air and in

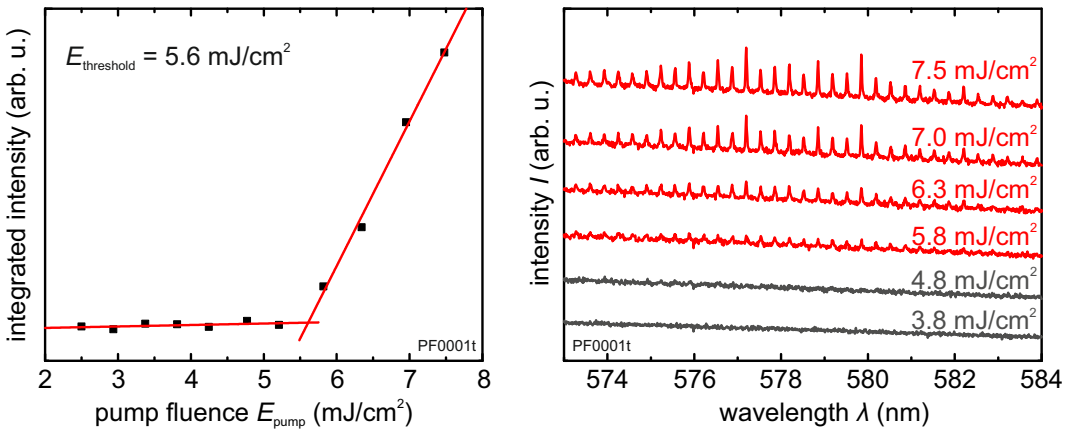

Figure 7.8: Lasing threshold of electrospun polymer fibers in aqueous environment. (a) Input-output curve with the typical kink illustrating the threshold behavior. (b) Emission spectra for increasing excitation energy with emerging lasing peaks as soon as the threshold is overcome. Adapted from [245].

water due to the changing difference in the effective refractive indices of the symmetric and antisymmetric modes (compare section 6.3.3). The modified coupling coefficient can lead to an increase in lasing threshold. Further possible reasons for the enhanced lasing threshold could be higher radiation losses of the resonant modes when the surrounding medium is water leading to a lower Q-factor. Additionally the overlap of the modes with the gain medium is smaller than in air due to a different field distribution. Furthermore, it is possible that some of the random loop resonators are mechanically unstable in water and the parallel running fiber parts forming the coupling region move apart from each other. Despite the comparably high lasing thresholds it is important to note that lasing is achieved even in aqueous environment.

For conduction of sensing experiments the lasing peaks must be present over several thousands of excitation pulses so that their peak position can be tracked over time. To test the stability of the lasing modes in aqueous environment emission spectra were recorded continuously. For an excitation energy clearly above threshold some lasing modes were present for more than 2×10^4 pump pulses. For comparison, in air lasing occurred 7.5 times longer. When a repetition rate of 20 Hz is used for excitation this corresponds to an achievable measurement time of 17 minutes. This time can be elongated when the fibers are not pumped continuously. As short detection times should be targeted anyway when a fast analysis is desired the lifetime of the lasing emission is in principle sufficient for applications.

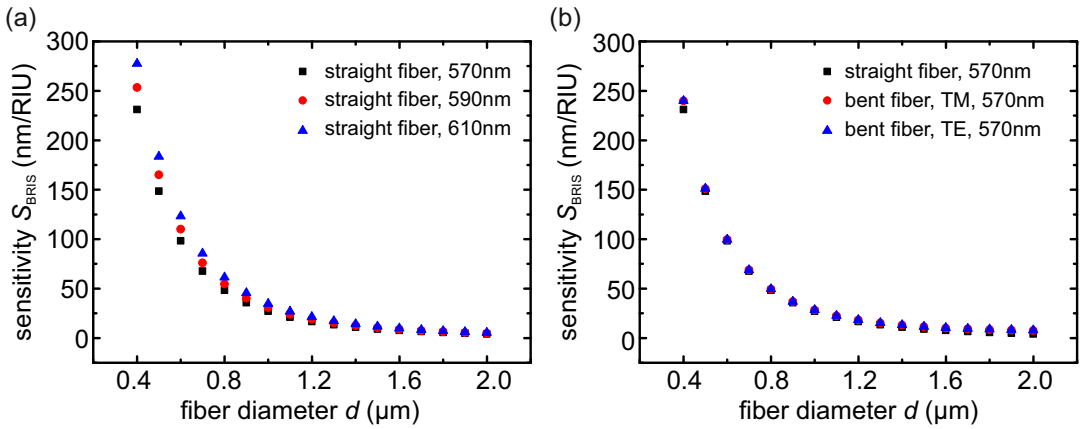

Figure 7.9: Simulation of the BRIS for varying fiber diameters. (a) BRIS values for different resonance wavelengths similar to the ones observed in experiments. (b) Comparison of the BRIS for straight and bent fibers with a bending radius of $R = 50\,\mu m$ showing that the influence of the bending is negligible.

7.2.2 Bulk Refractive Index Sensing

One way to demonstrate that the polymer fibers are suitable as sensors in aqueous environment are measurements of the BRIS (see section 5.1). Before experiments were conducted FEM simulations of the BRIS were performed with COMSOL to estimate the expected values. Influences of the fiber diameter and the bending radius were analyzed. In Fig. 7.9 the simulated BRIS values are plotted for different fiber diameters. Just as for WGM resonators thinner fiber diameters lead to an increased mode overlap with the surrounding and hence an enhanced BRIS. Furthermore, Fig. 7.9 (a) depicts the simulation results for different wavelengths and Fig. 7.9 (b) compares the results for a straight fiber with the results for TE and TM modes in a bent fiber with a bending radius of 50 µm. The simulation results confirm the expectations derived in Eq. 7.8 and show that the BRIS increases for larger wavelengths. The BRIS values of straight and bent fibers are similar justifying the assumption that influences due to bending are negligible.

Measurements of the BRIS were conducted as described in section 5.1. A peristaltic pump was used to exchange the solution with the different refractive indices. The pump ensures that the solution is filled carefully and slowly into the sample chamber to avoid displacement on the fiber network. Fig. 7.10 depicts a typical BRIS measurement with the characteristic steps in the peak position when the refractive index of the surrounding is modified. The slight increase of the baseline is probably caused by an insufficient exchange of the solutions due to the high density of the

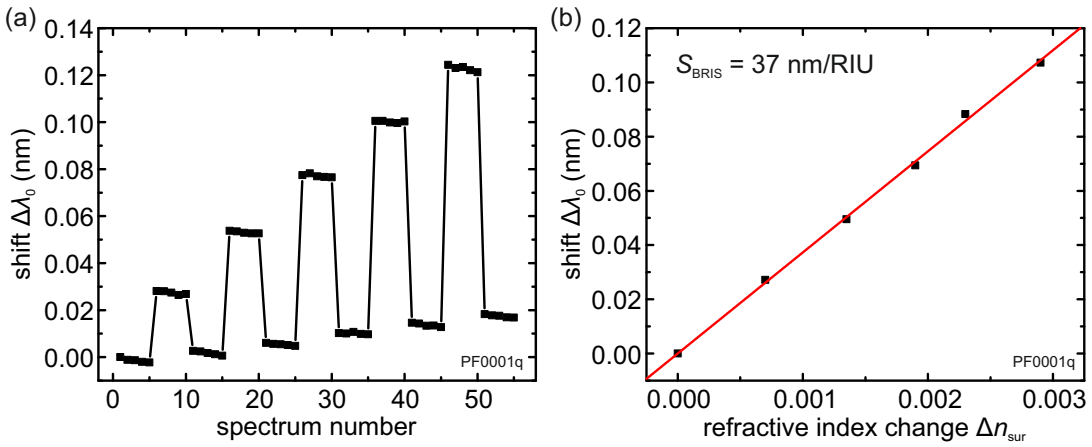

Figure 7.10: BRIS measurement of electrospun polymer fiber networks. The shift of the resonant mode when the fibers are exposed to surroundings with different refractive indices demonstrates that the sensing principle works.

fiber network. The overlying blue-shift arises from bleaching of the dye molecules as discussed previously. When bleaching was strong a correction of the curve was performed by subtracting the baseline. When plotting the shift versus the refractive index change (see Fig. 7.10 (b)) the average value of the step at the left and right side was used to further reduce disturbing influences.

Table 7.3 lists the results of the performed BRIS measurements from multiple random resonators. The differences arise from variations in the fiber diameter. In order to compare the measurements with the expectations from simulations the fiber diameters of the investigated samples were determined with SEM images. Multiple SEM images at different sample positions were taken to obtain the diameter distribution. A Gaussian distribution with a mean value of $d_{\mathrm{mean}} = 0.925\,\mu\mathrm{m}$ and a standard deviation of $\sigma = 0.08\,\mathrm{nm}$ was obtained. When considering fiber diameters of $d = d_{\mathrm{mean}} \pm 2\sigma$ and a resonance wavelength of 590 nm BRIS values from 25 to 61 nm/RIU are expected from simulations. The measurement results are in good agreement with the simulations. The higher measured value of 80 nm/RIU can be explained with a resonator with fiber diameter thinner than the given range. The BRIS values are comparable to the ones of the disc-shaped WGM lasers presented in chapter 5, which is reasonable since the fiber diameters and the thicknesses of the discs are also in the same range.

The experiments presented in this section show that the fibers are in principle also suitable as sensors in aqueous environments. They exhibit lasing emission which is

Table 7.3: Measured BRIS values of electrospun polymer fiber networks for different random resonators.

Sample	BRIS (nm/RIU)
PF0001p	80
PF0001q (M1)	37
PF0001q (M2)	41
PF0002f	32
PF0002h	61

stable long enough to demonstrate their sensing abilities via BRIS measurements. However, the lasing thresholds are increased and random resonators are difficult to find. Therefore, improvements are necessary to obtain more robust sensors. One possibility would be the use of a different resonator geometry, e.g., fiber rods which act as Fabry-Pérot cavities similar to the fibers presented in [191]. To fix the fibers to the substrate polymer glue could be deposited at the ends of the fibers with a micro-deposition setup.

7.3 Summary and Conclusions

In this chapter applications of the polymer fiber networks in optical sensing were discussed. Their suitability as vapor sensors and as sensors in aqueous environment was demonstrated with the spectral position of the lasing modes serving as sensor signal. For vapor sensing the reaction of the fibers when exposed to ethanol and methanol vapor was investigated. Ellipsometry measurements and an analytic model were used to predict the shift of the lasing modes which is mainly caused by a change of the refractive index of PMMA and length changes of the random resonators due to diffusion of vapor molecules into the polymer. The vapor sensing measurements of the alcohols ethanol and methanol revealed that the fibers exhibit different sensitivities towards ethanol and methanol. Furthermore, the saturation times for the two alcohols differ by almost two orders of magnitude. Investigations on ethanol–methanol mixtures show that both alcohols can be identified when the time-resolved peak shift of the lasing emission is analyzed, although quantification is challenging and requires additional calibration. An extension towards other polymers than PMMA as fiber material could allow the discrimination of a variety of different vapors.

Sensing in aqueous environment works via the evanescent field of the resonant modes in the random cavities. In this work lasing in aqueous environment was observed and BRIS measurements were conducted as proof-of-principle measurements. The experimental values were confirmed by FEM simulations. The high lasing thresholds in water could be improved by further developing the fibers, e.g., by changing the resonator geometry to Fabry-Pérot resonators where the fiber end facets serve as mirrors.

In summary the polymer fiber networks are promising as sensors, however the resonator geometry should be optimized so that defined resonator geometries are used instead of relying on random loop cavities.

Chapter 8

Conclusions and Outlook

Polymeric microlasers as well as their applications in optical sensing were in the focus of this work. Polymeric cavities are promising since they allow large-scale fabrication at low costs. Furthermore, the simple optical excitation and read-out of the microlasers via free-space optics enables on-chip integration. Additionally, low detection limits are achievable due to the high Q-factors of the cavities.

Summary and Conclusions of This Work

Two different kind of dye-doped polymeric cavities were investigated regarding their sensing performance in this work: WGM resonators in the shape of goblets and discs fabricated via lithography, and loop cavities in fiber networks fabricated via electrospinning.

The usage of polymers as host material for optical cavities allows for simple integration of different optical emitters. In this work the laser dye Fluorol 7GA was successfully integrated into WGM cavities and lasing emission in both air and aqueous environment at low thresholds was achieved, enabling excitation with a low-cost laser diode. Fluorol 7GA can be used as an alternative to the laser dye PM597 when lasing at different wavelengths is desired or in combination with PM597 to distinguish the signal from individual sensors when implementing multiplexed sensing.

Furthermore, in close collaboration with the IMT an all-polymeric sensor chip including a fluidic chamber based on goblet-shaped microlasers was developed. This represents an important first step towards an application outside a laboratory environment. The sensing ability of the integrated microgoblet lasers was demonstrated with BRIS measurements.

One crucial parameter of a sensor is the detection limit which represents the lowest amount of a change, e.g., a concentration of target molecules or refractive index change which can be reliably detected. The detection limit is given as the ratio of the system resolution to the sensitivity. It was shown that for WGM lasers the detection limit can be improved by enhancing the sensitivity without sacrificing resolution since the measurable linewidth of the lasing modes remains constant even if the Q-factor is reduced. The BRIS was used to quantify the sensitivity since the shift caused by attaching molecules is proportional to the BRIS and the results can be transferred to the detection of biomolecules.

Different strategies to enhance the sensitivity were pursued in this work: Coating the resonators with TiO_2 serving as high-refractive index layer or varying the size and the geometry of the cavities. For the former approach the mode overlap with the surrounding medium is increased since the mode is pulled further to the rim of the cavity. For the latter concept the radius and the thickness of the cavities were reduced to achieve the same effect. It turned out that with all methods an improved sensitivity is achievable. The reduction of the thickness of the cavities shows the greatest improvement regarding the detection limit. When also the lasing performance is considered thin goblet resonators show the best results since they exhibit increased sensitivities while showing low lasing thresholds due to their smooth surface. The method based on the variation of the size of the cavities is simple and does not require additional fabrication steps.

The second part of this thesis focused on dye-doped electrospun polymer fiber networks. Random loop resonators were identified as the source of lasing emission by using spatially resolved spectroscopy. The fiber loops forming the resonators can exhibit arbitrary shapes as long as a coupling region is formed where the fiber runs in parallel with itself for a certain distance. Quantitative analysis of the lasing spectra of different cavities further proved that the lasing emission is due to random resonators since the resonator length calculated from the free spectral range is in good agreement with the measured one. Furthermore, it was shown that the theory of a directional coupler describes the coupling region, where the fiber runs in parallel well itself. The conducted simulations can hence serve as a design guideline to maximize the coupling efficiency between the parallel running fiber to achieve resonators with low lasing thresholds.

In the same way as for the WGM resonators the spectral position of the lasing modes of the fiber loop cavities can serve as signal for sensing. In literature usually the fluorescence intensity of electrospun fibers serves as sensor signal when optical sensing experiments are conducted. In contrast to that, in this work the successful detection of different vapors and sensing in aqueous environment with PM597-doped polymer fiber networks was demonstrated using the shift of the lasing modes as

sensor signal. The principle of vapor sensing is based on the swelling of the polymer once it is exposed to solvent vapors which leads to an increased optical path length of the cavity and hence a detectable shift of the lasing modes. By using ellipsometry measurements and a simple analytical model it was shown that both the length change of the cavity and the change of the refractive index of the PMMA contribute to the shift of the lasing modes. Time-resolved sensing measurements on ethanol and methanol revealed different saturation times for the two alcohols which differ by almost two orders of magnitude. This can be exploited to identify ethanol and methanol even in mixtures of them. Hence, with this method the parallel detection of different vapors is feasible and might be further extended by using different fiber materials. When operating the fiber networks in aquoeus environment the lasing threshold increases but the operational lifetime is still sufficient to conduct sensing experiments. As proof-of-principle, BRIS experiments were conducted showing that the fiber networks are also suitable as biosensors. The measured BRIS values turned out to be in good agreement with expectations from simulations.

In conclusion, the dye-doped polymeric microlasers based on WGM cavities and on fiber loops are suitable as optical sensors which allow simple excitation and read-out.

Future Work

As already mentioned, disturbing influences from thermal noise can be minimized by using a referencing scheme [167]. The current referencing method for polymeric WGM lasers uses two independent cavities where one of them is covered with a polymeric glue inhibiting interactions with the surrounding analyte solution. By using two resonators which are vertically stacked on top of each other the referencing scheme could be improved further. Doping the resonators with dyes emitting at different wavelengths allows to distinguish their emission signals. The upper resonator could be functionalized with receptors by using, e.g., dip-pen nanolithography [246] while the lower one is not modified. This way the lower cavity serves as reference monitoring changes in the environment and unspecific adsorption while the upper one in addition monitors the actual signal change from binding of target molecules. This referencing scheme is compact, simple to read-out and allows correction for disturbing influences from temperature, bulk refractive index changes and unspecific binding.

For the electrospun polymeric fibers fabrication of designed and reproducible cavities is the next step since then the lasing performance, especially in aqueous environment, can be further improved. One possibility is the fabrication of fiber pieces where the end facets act as the mirrors of a Fabry-Pérot cavity or the fabrication of defined

fiber loops by using near field electrospinning.

Furthermore, different polymers can be used for fiber fabrication. By using polystyrene one can get rid of disturbing influences from the presence of water since this material does not swell upon exposure to humidity [221]. In addition, the use of different fiber materials gives the opportunity to perform multiplexed vapor or gas sensing. For each fiber material–vapor combination a characteristic saturation time is expected which allows differentiation of multiple vapors.

When thinking of sensing in aqueous environment the functionalization of the fiber surface would allow specific detection of certain molecules. With electropinning an intrinsic surface modification can be realized by using a suitable fiber material [199]. Thus, no additional treatment of the fibers is required which keeps the fabrication process simple. One could even fabricate fibers with multiple compartments which offer the possibility for referencing or parallel detection of different biomolecules.

Appendix A

Vapor Mixing System

The vapor mixing system consists of three flow controllers and two gas washing bottles. A schematic is depicted in Fig. A.1. The gas washing bottles are filled with the analytes which should be detected – in this case ethanol and methanol. Nitrogen is guided through the bottles to form a saturated vapor of the respective alcohol. The flow controllers, one for nitrogen, one for ethanol and one for methanol are used to adjust the vapor concentration. Valves between the bottle and the sample chamber ensure that no alcohol vapor reaches the sample during baseline acquisition. With the utilized flow meters methanol concentrations between 420 ppm and saturation and ethanol concentrations between 190 ppm and saturation can be set. The concentration in ppm is determined from the gas flows by the following relation:

$$c_{\mathrm{i}} = \frac{p_{\mathrm{i}}}{p_{\mathrm{N_2}}} \frac{J_{\mathrm{i}}}{J_{\mathrm{i}} + J_{\mathrm{N_2}}} \cdot 10^6. \tag{A.1}$$

Here, p_{i} denotes the vapor pressure of the solvents at room temperature which is 59.5 hPa for ethanol and 129 hPa for methanol. As experiments were carried out at ambient pressure $p_{\mathrm{N_2}} = 1013.25$ hPa was used. J_{i} and $J_{\mathrm{N_2}}$ denote the flow rates of ethanol or methanol and nitrogen.

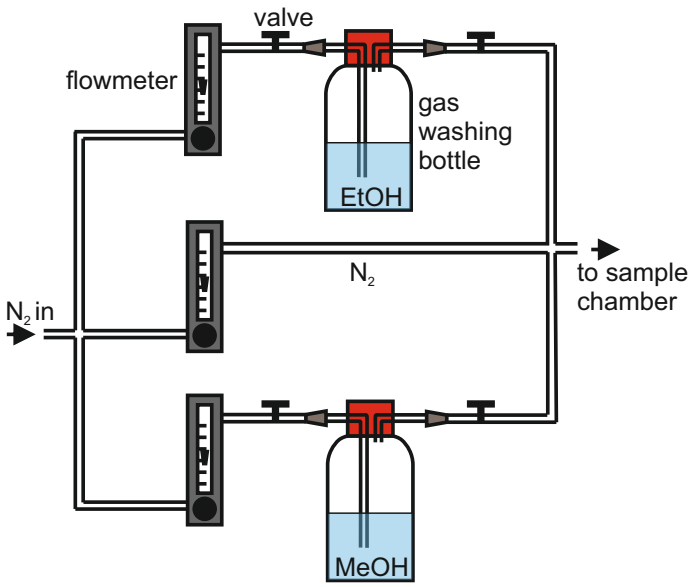

Figure A.1: Schematic of the vapor mixing system. Nitrogen is guided through gas washing bottles filled with methanol or ethanol (or water) to generate a saturated vapor. The desired concentration of the respective vapor can be adjusted by flow controllers. The mixture is then guided to the sample chamber with tubes.

Appendix B

Samples Investigated in This Work

Polymeric WGM Lasers

The sample preparation of the WGM cavities was done at the Institute of Applied Physics (APH) or the Institute of Microstructure Technology (IMT) both at the Karlsruhe Institute of Technology (KIT). In the following an overview on the samples investigated in this work is given. More information on the fabrication process can be found in [11, 107, 157].

Samples in chapter 4:

Table B.1: Fluorol 7GA-doped WGM cavities.

Sample final	Polymer	Dye	Dye concentration	shape
MG0038	PMMA/MA	Fluorol 7GA	40.5 µMol/g polymer	goblet

The cavities with polymeric pedestals and the cavities on PSU substrate were fabricated by Tobias Wienhold from IMT, KIT. Details on fabrication can be found in [165] and [82].

Samples in chapter 5:

Table B.2: WGM cavities with TiO_2 coating layer. The TiO_2 was deposited at the Technical University of Denmark (DTU)

Sample final	Sample without TiO_2	Shape	thickness TiO_2 (nm)
MG0096b	MG0094b	goblet	20
MG0096c	MG0094b	goblet	37
MG0096d	MG0094b	goblet	62
MG0096f	MG0094b	goblet	88

Table B.3: WGM cavities of varying size.

Sample	Spin-coating speed (rpm)	Shape	thickness (SEM) (µm)
MG0103	680	disc	0.90
MG0107	680	disc	0.90
MG0109	680	disc	0.88
MG0110	800	disc	0.71
MG0111	1800	disc	0.48
MG0112	3500	disc	0.29
MG0113	4500	disc	0.21
MG0114	680	disc	0.90
MG0128	4500	disc & goblet	0.37
MG0139	800	disc	0.84
MG0140	1200	disc	0.50

Dye-Doped Polymeric Fiber Networks

The dye-doped polymeric fiber networks where fabricated via electrospinning at the Technical University of Denmark. Details on the electrospinning process can be found in [132].

Table B.4: Dye-doped polymer fiber networks.

Sample	PMMA (350k) in DMF (% wt/v)	Dye	Dye concentration
PMMA_13A	13	Rh6G	0.3 mg/mL
PMMA_12B	12	Rh6G	0.3 mg/mL
PF0001	12	PM597	9.36 mg/g PMMA
PF0004	12	PM597	9.36 mg/g PMMA

List of Publications

Regular Articles

1. **Impact of Protein Modification on the Protein Corona on Nanoparticles and Nanoparticle-Cell Interactions**,
L. Treuel, S. Brandholt, P. Maffre, S. Wiegele, L. Shang, and G. U. Nienhaus, *ACS Nano*, **8**, 503-513 (2014)

2. **Strongly Confining Bare Core CdTe Quantum Dots in Polymeric Microdisk Resonators**,
A. Flatae, T. Grossmann, T. Beck, S. Wiegele, and H. Kalt, *APL Materials* **2**, 012107 (2014)

3. **Random-Cavity Lasing from Electrospun Polymer Fiber Networks**,
S. Krämmer, C. Vannahme, C. L. C. Smith, T. Grossmann, M. Jenne, S. Schierle, L. Jørgensen, I. S. Chronakis, A. Kristensen, and H. Kalt, *Advanced Materials* **26**, 8096-8100 (2014)

4. **Efficient Free-Space Read-Out of WGM Lasers Using Circular Micromirrors**,
T. Wienhold, S. Krämmer, A. Bacher, H. Kalt, C. Koos, S. Köber, and T. Mappes, *Optics Express* **23**, 1025-1034 (2015)

5. **Densely Packed Microgoblet Laser Pairs for Cross-Referenced Biomolecular Detection**,
U. Bog, F.Brinkmann, S. F. Wondimu, T.Wienhold, S. Krämmer, C. Koos, H. Kalt, M. Hirtz, H. Fuchs, S. Köber, and T. Mappes, *Advanced Science* **2**, 1500066 (2015)

6. **Optically Controlled Elastic Microcavities**,
A. M. Flatae, M. Burresi, H. Zeng, S. Nocentini, S. Wiegele, C. Parmeggiani, H. Kalt, and D. Wiersma, *Light: Science & Applications* **4**, e282, (2015)

7. **All-Polymer Photonic Sensing Platform Based on Whispering-Gallery Mode Microgoblet Lasers**,
T. Wienhold, S. Krämmer, S. F. Wondimu, T. Siegle, U. Bog, U. Weinzierl, S. Schmidt, H. Becker, H. Kalt, T. Mappes, S. Köber, and C. Koos, *Lab on a Chip* **15**, 3800-3806 (2015)

8. **Photonic Molecules with a Tunable Inter-Cavity Gap**,
T. Siegle, S. Schierle, S. Krämmer, B. Richter, S. F. Wondimu, P. Schuch, C. Koos and H. Kalt, *Light: Science & Applications*, *accepted* (2016)

9. **High-Q Whispering Gallery Microdisk Resonators Based on Silicon Oxynitride**,
T. Hett, S. Krämmer, U. Hilleringmann, H. Kalt, and A. Zrenner, *Journal of Luminescence*, *accepted* (2016)

10. **Electrospun Polymer Fiber Lasers for Applications in Vapor Sensing**,
S. Krämmer, F. Laye, F. Friedrich, C. Vannahme, C. L. C. Smith, A. C. Mendes, I. S. Chronakis, A. Kristensen, and H. Kalt, *manuscript in preparation*

11. **Size-Optimized Polymeric Whispering Gallery Mode Lasers with Enhanced Sensing Performance**,
S. Krämmer, S. Rastjoo, T. Siegle, S. F. Wondimu, C. Klusmann, and H. Kalt, *manuscript in preparation*

Contributions to International Conferences with Proceedings

1. **Low Threshold Microgoblet Dye Lasers for Biosensing Applications**,
S. Wiegele, T. Grossmann, T. Beck, J. Fischer, T. Wienhold, T. Mappes, and H. Kalt, *CLEO/Europe – EQEC 2013, Conference on Lasers and Electro-Optics – European Quantum Electronics Conference, München, Germany (2013)*, Talk

2. **Polymeric Microresonators for Biosensing Applications**,
S. Wiegele, T. Beck, T. Grossmann, M. Mai, T. Mappes, and H. Kalt, *Nano-Structures for Optics and Photonics, Erice, Italy (2013)*, Talk
NATO Science for Peace and Security Series B: Physics and Biophysics, Springer (2015)

3. **Polymeric Whispering Gallery Mode Resonators for Biosensing Applications**,
S. Wiegele, T. Beck, T. Grossmann, R. Schmager, J. Fischer, M. Mai, T. Wienhold, U. Bog, C. Friedmann, T. Mappes, and H. Kalt, *CLEO 2014: Laser Science to Photonics Applications, San Jose, USA (2014)*, Talk

4. **Opto-Mechanically Tunable Polymeric Microlasers**,
A. Flatae, M. Burresi, H. Zeng, S. Nocentini, S. Wiegele, D. Wiersma, and H. Kalt, *CLEO 2014: Laser Science to Photonics Applications, San Jose, USA (2014)*, Poster Presentation

5. **Electrospun Dye-Doped Fiber Networks: Lasing Emission from Randomly Distributed Cavities**,
S. Krämmer, C. Vannahme, C. L. C. Smith, T. Grossmann, M. Jenne, S. Schierle, L. Jørgensen, N. M. Tran, I. S. Chronakis, A. Kristensen, and H. Kalt, *CLEO 2015: Laser Science to Photonics Applications, San Jose, USA (2015)*, Talk

6. **Free-Space Read-Out of WGM Lasers Using Circular Micromirrors**,
T. Wienhold, S. Krämmer, A. Bacher, H. Kalt, C. Koos, S. Köber, and T. Mappes, *CLEO 2015: Laser Science to Photonics Applications, San Jose, USA (2015)*, Talk

7. **Phospholipid-Functionalized Microgoblet Lasers for Biomolecular Detection**,
U. Bog, F. Brinkmann, S. F. Wondimu, T. Wienhold, S. Krämmer, C. Koos, H. Kalt, S. Köber, T. Mappes, M. Hirtz, and H. Fuchs, *CLEO 2015: Laser Science to Photonics Applications, San Jose, USA (2014)*, Talk

8. **Vertically Stacked AllPolymer Whispering Gallery Mode Lasers for Biosensing Applications**,
S. F. Wondimu, T. Siegle, U. Bog, S. Krämmer, H. Kalt, T. Mappes, S. Köber, T. Wienhold, and C. Koos, *CLEO 2015: Laser Science to Photonics Applications, San Jose, USA (2015)*, Poster Presentation

9. **Coupled Polymeric Whispering Gallery Mode Cavities**,
T. Siegle, S. Krämmer, T. Grossmann, and H. Kalt, *OECS 2015: International Conference on Optics of Excitons in Confined Systems, Jerusalem, Israel (2015)*, Poster Presentation

10. **High-Q Whispering Gallery Microdisk Resonators Based on Silicon Oxynitride**,
T. Hett, S. Krämmer, U. Hilleringmann, H. Kalt, and A. Zrenner, *E-MRS Spring Meeting, Lille, France (2016)*, Talk

11. **Tunable Coupling of Whispering Gallery Mode Resonators on Elastomer Substrates**,
T. Siegle, S. Schierle, S. Krämmer, B. Richter, S. Wondimu, P. Schuch, C. Koos, and H. Kalt, *CLEO 2016: Laser Science to Photonics Applications, San Jose, USA (2016)*, Talk

12. **Soft Lithography of 3D Polymeric Lasers and Cavities**,
O. Bar-On, P. Brenner, T. Siegle, R. Gvishi, S. Krämmer, H. Kalt, U. Lemmer, and J. Scheuer, *CLEO 2016: Laser Science to Photonics Applications, San Jose, USA (2016)*, Talk

13. **Optical Sensors from Electrohydrodynamic Jetted Polymer Fiber Resonators**,
F. Laye, S. Krämmer, A. Castillo, F. Freidrich, C. Vannahme, C. L. C. Smith, A. C. Mendes, I. S. Chronakis, A. Kristensen, J. Lahann, and H. Kalt, *CLEO 2016: Laser Science to Photonics Applications, San Jose, USA (2016)*, Poster Presentation

Contributions to Workshops

1. **Polymeric Microresonators with Efficient Laser Dyes**,
S. Wiegele, T. Grossmann, T. Wienhold, R. Schmager, J. Fischer, T. Siegle, S. Köber, T. Mappes, and H. Kalt, *560. WE-Heraeus-Seminar on Taking Detection to the Limit: Biosensing with Optical Microcavities, Bad Honnef, Germany (2014)*, Poster Presentation

2. **On-Chip Integration of Polymer Microgoblet Lasers**,
T. Wienhold, S. Wiegele, C. Koos, H. Kalt, S. Köber, and T. Mappes, *560. WE-Heraeus-Seminar on Taking Detection to the Limit: Biosensing with Optical Microcavities, Bad Honnef, Germany (2014)*, Poster Presentation

Contributions to DPG Spring Meetings

1. **Microgoblet Lasers for Label-Free Biosensing**,
   J. Fischer, S. Wiegele, T. Grossmann, T. Beck, M. Mai, U. Bog, T. Mappes, and H. Kalt, *DPG spring meeting, Regensburg (2013)*, Poster Presentation

2. **Optical Modes in Photonic Molecules from Whispering-Gallery-Mode Microcavities**,
   T. Siegle, S. Wiegele, C. Klusmann, T. Grossmann, T. Wienhold, U. Bog, S. Köber, and H. Kalt, *DPG spring meeting, Dresden (2014)*, Talk

3. **Quantum Dots and Lanthanides as cw-Emitters in Polymeric Microresonators**,
   C. Klusmann, S. Wiegele, T. Siegle, T. Wienhold, S. Köber, C. Koos, and H. Kalt, *DPG spring meeting, Dresden (2014)*, Poster Presentation

4. **Random-Cavity Lasing from Electrospun Polymer Fiber Networks**,
   S. Krämmer, C. Vannahme, C. L. C. Smith, T. Grossmann, M. Jenne, S. Schierle, M. Tran, L. Jørgensen, I. S. Chronakis, A. Kristensen, and H. Kalt, *DPG spring meeting, Berlin (2015)* Talk

5. **TiO_2 Coated Whispering Gallery Mode (WGM) Resonators for Label-Free Biosensing**,
   F. Ruf, S. Krämmer, C. Vannahme, A. Vigovskaya, L. Fruk, A. Kristensen, and H. Kalt, *DPG spring meeting, Berlin (2015)*, Talk

6. **Electrospun Dye-Doped Polymeric Fiber Networks for Alcohol Vapor Detection**,
   S. Krämmer, F. Laye, C. Vannahme, M. Tran, P. Kiefer, F. Friedrich, C. L. C. Smith, A. C. Mendes, I. S. Chronakis, A. Kristensen, and H. Kalt, *DPG spring meeting, Regensburg (2016)*, Talk

7. **Flexible Formation of Coupled Active Polymeric Whispering Gallery Mode Cavities on an Elastomer Substrate**,
   S. Schierle, T. Siegle, S. Krämmer, B. Richter, S. Wondimu, P. Schuch, C. Koos, and H. Kalt, *DPG spring meeting, Regensburg (2016)*, Talk

8. **Plasmon-Enhanced Biosensing with Polymeric Whispering-Gallery-Mode Resonators**,
   C. Klusmann, S. Krämmer, S. A. Schmid, T. Siegle, C. Rockstuhl, and H. Kalt, *DPG spring meeting, Regensburg (2016)*, Poster Presentation

9. **Effect of Different Excitation and Collection Geometries on the Lasing Threshold of PM597-Doped WGM Micro Disk Cavities**,
   T. Siegle, M. Bonenberger, S. Krämmer, C. Klusmann, and H. Kalt, *DPG spring meeting, Regensburg (2016)*, Poster Presentation

10. **Whispering Gallery Mode Resonators with Varying Diameter and Thickness for Enhanced Sensitivity**,
    S. Rastjoo, S. Krämmer, T. Siegle, C. Klusmann, and H. Kalt, *DPG spring meeting, Regensburg (2016)*, Poster Presentation

11. **Dye-Doped Electrohydrodynamic Co-Jetted Polymeric Fibers for Optical Resonators**,
    F. Laye, S. Krämmer, A. Castillo, J. Lahann, and H. Kalt, *DPG spring meeting, Regensburg (2016)*, Poster Presentation

Bibliography

[1] L. J. Kricka, "Microchips, Microarrays, Biochips and Nanochips: Personal Laboratories for the 21st Century," Clinica Chimica Acta **307**, 219–223 (2001).

[2] P. Yager, T. Edwards, E. Fu, K. Helton, K. Nelson, M. R. Tam, and B. H. Weigl, "Microfluidic Diagnostic Technologies for Global Public Health," Nature **442**, 412–418 (2006).

[3] C. D. Chin and S. K. Sia, "Lab-on-a-Chip Devices for Global Health: Past Studies and Future opportunities," Lab on a Chip **7**, 41–57 (2007).

[4] X. Fan, I. M. White, S. I. Shopova, H. Zhu, J. D. Suter, and Y. Sun, "Sensitive Optical Biosensors for Unlabeled Targets: A Review," Analytica Chimica Acta **620**, 8–26 (2008).

[5] F. Vollmer and L. Yang, "Label-Free Detection with High-Q Microcavities: A Review of Biosensing Mechanisms for Integrated Devices," Nanophotonics **1**, 267–291 (2012).

[6] M. R. Foreman, J. D. Swaim, and F. Vollmer, "Whispering Gallery Mode Sensors," Advances in Optics and Photonics **7**, 168–240 (2015).

[7] M. S. Luchansky and R. C. Bailey, "High-Q Optical Sensors for Chemical and Biological Analysis," Analytical Chemistry **84**, 793–821 (2012).

[8] K. J. Vahala, "Optical Microcavities," Nature **424**, 839–846 (2003).

[9] J. Su, A. F. Goldberg, and B. M. Stoltz, "Label-Free Detection of Single Nanoparticles and Biological Molecules Using Microtoroid Optical Resonators," Light: Science & Applications **5**, e16001 (2016).

[10] V. R. Dantham, S. Holler, C. Barbre, D. Keng, V. Kolchenko, and S. Arnold, "Label-Free Detection of Single Protein Using a Nanoplasmonic-Photonic Hybrid Microcavity," Nano Letters **13**, 3347–3351 (2013).

[11] T. Großmann, "Whispering-Gallery-Mode Lasing in Polymeric Microcavities," Ph.D. Thesis, Karlsruhe Institute of Technology (KIT) (2012).

[12] K. Kalantar-zadeh and B. Fry, eds., *Nanotechnology-Enabled Sensors* (Springer, 2008).

[13] A. Shrivastava and V. Gupta, "Methods for the Determination of Limit of Detection and Limit of Quantitation of the Analytical Methods," Chronicles of Young Scientists **2**, 21–25 (2011).

[14] F. J. Amore, G. V. Cox, D. G. Crosby, F. L. Estes, D. H. Freeman, W. E. Gibbs, G. E. Gordon, L. H. Keith, R. R. Langner, N. I. McClelland, W. F. Phillips, R. B. Pojasek, R. E. Sievers, D. H. Freeman, W. F. Phillips, J. K. Taylor, E. M. Epa, M. R. Monsanto, and D. Macdougall, "Guidelines for Data Acquisition and Data Quality Evaluation in Environmental Chemistry," Analytical Chemistry **52**, 2242–2249 (1980).

[15] S. Chandran and R. S. Singh, "Comparison of Various International Guidelines for Analytical Method Validation," Pharmazie **62**, 4–14 (2007).

[16] I. M. White and X. Fan, "On the Performance Quantification of Resonant Refractive Index Sensors," Optics Express **16**, 1020–1028 (2008).

[17] J. Janata, *Principles of Chemical Sensors* (Springer, 2009).

[18] S. Some, Y. Xu, Y. Kim, Y. Yoon, H. Qin, A. Kulkarni, T. Kim, and H. Lee, "Highly Sensitive and Selective Gas Sensor Using Hydrophilic and Hydrophobic Graphenes," Scientific Reports **3**, 01868 (2013).

[19] L. Xu, Z. Dai, G. Duan, L. Guo, Y. Wang, H. Zhou, Y. Liu, W. Cai, Y. Wang, and T. Li, "Micro/Nano Gas Sensors: A New Strategy Towards In-Situ Wafer-Level Fabrication of High-Performance Gas Sensing Chips," Scientific Reports **5**, 10507 (2015).

[20] W. E. Moerner, "New Directions in Single-Molecule Imaging and Analysis," Proceedings of the National Academy of Sciences of the United States of America **104**, 12596–12602 (2007).

[21] W. G. Cox and V. L. Singer, "Fluorescent DNA Hybridization Probe Preparation Using Amine Modification and Reactive Dye Coupling," BioTechniques **36**, 114–122 (2004).

[22] J. M. Hollas, *Modern Spectroscopy* (John Wiley & Sons, 2004).

[23] A. Nitkowski, L. Chen, and M. Lipson, "Cavity-Enhanced On-Chip Absorption Spectroscopy Using Microring Resonators." Optics Express **16**, 11930–11936 (2008).

[24] W.-C. Lai, S. Chakravarty, X. Wang, C. Lin, and R. T. Chen, "On-Chip Methane Sensing by Near-IR Absorption Signatures in a Photonic Crystal Slot Waveguide," Optics Letters **36**, 984–986 (2011).

[25] D. J. Gardiner and P. R. Graves, eds., *Practical Raman Spectroscopy* (Springer, 1989).

[26] P. Atkins, *Physical Chemistry* (Oxford University Press, 2009).

[27] P. Y. Yu and M. Cardona, *Fundamentals of Semiconductors* (Springer, 1996).

[28] R. F. Begley, A. B. Harvey, and R. L. Byer, "Coherent Anti-Stokes Raman Spectroscopy," Applied Physics Letters **25**, 387–390 (1974).

[29] C. L. Haynes, A. D. McFarland, and R. P. V. Duyne, "Surface-Enhanced Raman Spectroscopy," Analytical Chemistry **77**, 338 A–346 A (2005).

[30] M. Hippler, "Cavity-Enhanced Raman Spectroscopy of Natural Gas with Optical Feedback cw-Diode Lasers," Analytical Chemistry **87**, 7803–7809 (2015).

[31] X. Liu, S. Lebedkin, H. Besser, W. Pfleging, S. Prinz, X. M. Wissmann, P. M. Schwab, I. Nazarenko, M. Guttmann, M. M. Kappes, and U. Lemmer, "Tailored Surface-Enhanced Raman Nanopillar Arrays Fabricated by Laser-Assisted Replication for Biomolecular Semiconductor Lasers," ACS Nano **9**, 260–270 (2015).

[32] J. Homola, S. S. Yee, and G. Gauglitz, "Surface Plasmon Resonance Sensors: Review," Sensors and Actuators B: Chemical **54**, 3–15 (1999).

[33] J. Homola, "Present and Future of Surface Plasmon Resonance Biosensors," Analytical and Bioanalytical Chemistry **377**, 528–539 (2003).

[34] R. B. M. Schasfoort and A. J. Tudos, eds., *Handbook of Surface Plasmon Resonance* (The Royal Society of Chemistry, 2008).

[35] B. Liedberg, C. Nylander, and I. Lundstrom, "Surface Plasmon Resonance for Gas Detection and Biosensing," Sensors and Actuators **4**, 299–304 (1983).

[36] J. Dostálek, J. Homola, and M. Miler, "Rich Information Format Surface Plasmon Resonance Biosensor Based on Array of Diffraction Gratings," Sensors and Actuators B: Chemical **107**, 154–161 (2005).

[37] J. Dostálek, J. Čtyroký, J. Homola, E. Brynda, M. Skalský, P. Nekvindová, J. Špirková, J. Škvor, and J. Schröfel, "Surface Plasmon Resonance Biosensor Based on Integrated Optical Waveguide," Sensors and Actuators B: Chemical **76**, 8–12 (2001).

[38] D. Monzón-Hernández and J. Villatoro, "High-Resolution Refractive Index Sensing by Means of a Multiple-Peak Surface Plasmon Resonance Optical Fiber Sensor," Sensors and Actuators B: Chemical **115**, 227–231 (2006).

[39] H. J. Lee, D. Nedelkov, and R. M. Corn, "Surface Plasmon Resonance Imaging Measurements of Antibody Arrays for the Multiplexed Detection of Low Molecular Weight Protein Biomarkers," Analytical Chemistry **78**, 6504–6510 (2006).

[40] Y. Teramura and H. Iwata, "Label-Free Immunosensing for α-fetoprotein in Human Plasma Using Surface Plasmon Resonance," Analytical Biochemistry **365**, 201–207 (2007).

[41] X. Yao, X. Li, F. Toledo, C. Zurita-Lopez, M. Gutova, J. Momand, and F. Zhou, "Sub-Attomole Oligonucleotide and p53 cDNA Determinations via a High-Resolution Surface Plasmon Resonance Combined with Oligonucleotide-Capped Gold Nanoparticle Signal Amplification," Analytical Biochemistry **354**, 220–228 (2006).

[42] F. Song, F. Zhou, J. Wang, N. Tao, J. Lin, R. L. Vellanoweth, Y. Morquecho, and J. Wheeler-Laidman, "Detection of Oligonucleotide Hybridization at Femtomolar Level and Sequence-Specific Gene Analysis of the *Arabidopsis Thaliana* Leaf Extract with an Ultrasensitive Surface Plasmon Resonance Spectrometer." Nucleic Acids Research **30**, e72 (2002).

[43] J. W. Waswa, C. Debroy, and J. Irudayaraj, "Rapid Detection of Salmonella Enteritidis and Escherichia Coli Using Surface Plasmon Resonance Biosensor," Journal of Food Process Engineering **29**, 373–385 (2006).

[44] C. Nylander, B. Liedberg, and T. Lind, "Gas Detection by Means of Surface Plasmon Resonance," Sensors and Actuators **3**, 79–88 (1983).

[45] S. K. Mishra and B. D. Gupta, "Surface Plasmon Resonance-Based Fiber Optic," Journal of Lightwave Technology **33**, 2770–2776 (2015).

[46] R. Tabassum, S. K. Mishra, and B. D. Gupta, "Surface Plasmon Resonance-Based Fiber Optic Hydrogen Sulphide Gas Sensor Utilizing Cu-ZnO Thin Films," Physical Chemistry Chemical Physics **15**, 11868–11874 (2013).

[47] I. Ament, J. Prasad, A. Henkel, S. Schmachtel, and C. Sönnichsen, "Single Unlabeled Protein Detection on Individual Plasmonic Nanoparticles," Nano Letters **12**, 1092–1095 (2012).

[48] P. Zijlstra, P. M. R. Paulo, and M. Orrit, "Optical Detection of Single Non-Absorbing Molecules Using the Surface Plasmon Resonance of a Gold Nanorod," Nature Nanotechnology **7**, 379–382 (2012).

[49] N. M. M. Pires, T. Dong, U. Hanke, and N. Hoivik, "Recent Developments in Optical Detection Technologies in Lab-on-a-Chip Devices for Biosensing Applications," Sensors **14**, 15458–15479 (2014).

[50] A. F. Coskun, A. E. Cetin, B. C. Galarreta, D. A. Alvarez, H. Altug, and A. Ozcan, "Lensfree Optofluidic Plasmonic Sensor for Real-Time and Label-Free Monitoring of Molecular Binding Events over a Wide Field-of-View," Scientific Reports **4**, 06789 (2014).

[51] O. Krupin, H. Asiri, C. Wang, R. N. Tait, and P. Berini, "Biosensing Using Straight Long-Range Surface Plasmon Waveguides," Optics Express **21**, 698–709 (2013).

[52] Y. Yanase, T. Hiragun, K. Ishii, T. Kawaguchi, T. Yanase, M. Kawai, K. Sakamoto, and M. Hide, "Surface Plasmon Resonance for Cell-Based Clinical Diagnosis," Sensors **14**, 4948–4959 (2014).

[53] J. D. Joannopoulos, S. G. Johnson, J. N. Winn, and R. D. Meade, *Photonic Crystals: Molding the Flow of Light* (Princeton University Press, 2008).

[54] B. Cunningham, P. Li, B. Lin, and J. Pepper, "Colorimetric Resonant Reflection as a Direct Biochemical Assay Technique," Sensors and Actuators B: Chemical **81**, 316–328 (2002).

[55] N. Skivesen, A. Têtu, M. Kristensen, J. Kjems, L. H. Frandsen, and P. I. Borel, "Photonic-Crystal Waveguide Biosensor," Optics Express **15**, 3169–3176 (2007).

[56] L. Rindorf, J. B. Jensen, M. Dufva, L. H. Pedersen, P. E. Høiby, and O. Bang, "Photonic Crystal Fiber Long-Period Gratings for Biochemical Sensing." Optics Express **14**, 8224–8231 (2006).

[57] E. Chow, A. Grot, L. W. Mirkarimi, M. Sigalas, and G. Girolami, "Ultra-compact Biochemical Sensor Built with Two-Dimensional Photonic Crystal Microcavity." Optics Letters **29**, 1093–1095 (2004).

[58] M. R. Lee and P. M. Fauchet, "Nanoscale Microcavity Sensor for Single Particle Detection," Optics Letters **32**, 3284–3286 (2007).

[59] M. R. Lee and P. M. Fauchet, "Two-Dimensional Silicon Photonic Crystal Based Biosensing Platform for Protein Detection," Optics Express **15**, 4530–4535 (2007).

[60] L. L. Chan, B. T. Cunningham, P. Y. Li, and D. Puff, "Self-Referenced Assay Method for Photonic Crystal Biosensors: Application to Small Molecule Analytes," Sensors and Actuators B: Chemical **120**, 392–398 (2007).

[61] N. Li, X. R. Cheng, A. Brahmendra, A. Prashar, T. Endo, C. Guyard, M. Terebiznik, and K. Kerman, "Photonic Crystals on Copolymer Film for Bacteria Detection," Biosensors and Bioelectronics **41**, 354–358 (2013).

[62] H. Shafiee, E. A. Lidstone, M. Jahangir, F. Inci, E. Hanhauser, T. J. Henrich, D. R. Kuritzkes, B. T. Cunningham, and U. Demirci, "Nanostructured Optical Photonic Crystal Biosensor for HIV Viral Load Measurement," Scientific Reports **4**, 04116 (2014).

[63] V. Toccafondo, J. García-Rupérez, M. J. Bañuls, A. Griol, J. G. Castelló, S. Peransi-Llopis, and A. Maquieira, "Single-Strand DNA Detection Using a Planar Photonic-Crystal-Waveguide-Based Sensor," Optics Letters **35**, 3673–3675 (2010).

[64] T. Ritari, J. Tuominen, H. Ludvigsen, J. Petersen, T. Sørensen, T. Hansen, and H. Simonsen, "Gas Sensing Using Air-Guiding Photonic Bandgap Fibers," Optics Express **12**, 4080–4087 (2004).

[65] F. Liang, N. Clarke, P. Patel, M. Loncar, and Q. Quan, "Scalable Photonic Crystal Chips for High Sensitivity Protein Detection," Optics Express **21**, 32306–32312 (2013).

[66] A. L. Washburn and R. C. Bailey, "Photonics-on-a-Chip: Recent Advances in Integrated Waveguides as Enabling Detection Elements for Real-World, Lab-on-a-Chip Biosensing Applications," Analyst **136**, 227–236 (2012).

[67] B. Sepúlveda, J. S. D. Río, M. Moreno, F. J. Blanco, K. Mayora, C. Domínguez, and L. M. Lechuga, "Optical Biosensor Microsystems Based on the Integration of Highly Sensitive Mach–Zehnder Interferometer Devices," Journal of Optics A: Pure and Applied Optics **8**, S561–S566 (2006).

[68] A. Brandenburg, "Differential Refractometry by an Integrated-Optical Young Interferometer," Sensors and Actuators B: Chemical **39**, 266–271 (1997).

[69] P. Dumais, C. L. Callender, J. P. Noad, and C. J. Ledderhof, "Integrated Optical Sensor Using a Liquid-Core Waveguide in a Mach-Zehnder Interferometer," Optics Express **16**, 18164–18172 (2008).

[70] Q. Liu, X. Tu, K. W. Kim, J. S. Kee, Y. Shin, K. Han, Y. J. Yoon, G. Q. Lo, and M. K. Park, "Highly Sensitive Mach-Zehnder Interferometer Biosensor Based on Silicon Nitride Slot Waveguide," Sensors and Actuators B: Chemical **188**, 681–688 (2013).

[71] A. Ymeti, J. Greve, P. V. Lambeck, T. Wink, S. W. F. M. van Hövell, T. A. M. Beumer, R. R. Wijn, R. G. Heideman, V. Subramaniam, and J. S. Kanger, "Fast, Ultrasensitive Virus Detection Using a Young Interferometer Sensor," Nano Letters **7**, 394–397 (2007).

[72] J. Xu, D. Suarez, and D. S. Gottfried, "Detection of Avian Influenza Virus Using an Interferometric Biosensor," Analytical and Bioanalytical Chemistry **389**, 1193–1199 (2007).

[73] N. Fabricius, G. Gauglitz, and J. Ingenhoff, "A Gas Sensor Based on an Integrated Optical Mach-Zehnder Interferometer," Sensors and Actuators B: Chemical **7**, 672–676 (1992).

[74] A. Crespi, Y. Gu, B. Ngamsom, H. J. W. M. Hoekstra, C. Dongre, M. Pollnau, R. Ramponi, H. H. van den Vlekkert, P. Watts, G. Cerullo, and R. Osellame, "Three-Dimensional Mach-Zehnder Interferometer in a Microfluidic Chip for Spatially-Resolved Label-Free Detection," Lab on a Chip **10**, 1167–1173 (2010).

[75] G. H. Cross, A. A. Reeves, S. Brand, J. F. Popplewell, L. L. Peel, M. J. Swann, and N. J. Freeman, "A New Quantitative Optical Biosensor for Protein Characterisation," Biosensors and Bioelectronics **19**, 383–390 (2003).

[76] N. M. Hanumegowda, C. J. Stica, B. C. Patel, I. White, and X. Fan, "Refractometric Sensors Based on Microsphere Resonators," Applied Physics Letters **87**, 1–3 (2005).

[77] F. Vollmer, D. Braun, A. Libchaber, M. Khoshsima, I. Teraoka, and S. Arnold, "Protein Detection by Optical Shift of a Resonant Microcavity," Applied Physics Letters **80**, 4057–4059 (2002).

[78] F. Vollmer, S. Arnold, and D. Keng, "Single Virus Detection from the Reactive Shift of a Whispering-Gallery Mode," Proceedings of the National Academy of Sciences of the United States of America **105**, 20701–20704 (2008).

[79] H.-C. Ren, F. Vollmer, S. Arnold, and A. Libchaber, "High-Q Microsphere Biosensor – Analysis for Adsorption of Rodlike Bacteria," Optics Express **15**, 17410–17423 (2007).

[80] F. Vollmer, S. Arnold, D. Braun, I. Teraoka, and A. Libchaber, "Multiplexed DNA Quantification by Spectroscopic Shift of Two Microsphere Cavities," Biophysical Journal **85**, 1974–1979 (2003).

[81] Y. Sun, J. Liu, G. Frye-Mason, S. Ja, A. K. Thompson, and X. Fan, "Optofluidic Ring Resonator Sensors for Rapid DNT Vapor Detection," The Analyst **134**, 1386–1391 (2009).

[82] T. Wienhold, S. Kraemmer, S. F. Wondimu, T. Siegle, U. Bog, U. Weinzierl, S. Schmidt, H. Becker, H. Kalt, T. Mappes, S. Koeber, and C. Koos, "All-Polymer Photonic Sensing Platform Based on Whispering-Gallery Mode Microgoblet Lasers," Lab on a Chip **15**, 3800–3806 (2015).

[83] U. Bog, F. Brinkmann, S. F. Wondimu, T. Wienhold, S. Kraemmer, C. Koos, H. Kalt, M. Hirtz, H. Fuchs, S. Koeber, and T. Mappes, "Densely Packed Microgoblet Laser Pairs for Cross-Referenced Biomolecular Detection," Advanced Science **2**, 1500066 (2015).

[84] F. Vollmer and S. Arnold, "Whispering-Gallery-Mode Biosensing: Label-Free Detection Down to Single Molecules," Nature Methods **5**, 591–596 (2008).

[85] Y. Takezawa, N. Taketani, S. Tanno, and S. Ohara, "Empirical Estimation Method of Intrinsic Loss Spectra in Transparent Amorphous Polymers for Plastic Optical Fibers," Journal of Applied Polymer Science **46**, 1835–1841 (1992).

[86] J. D. Jackson, *Classical Electrodynamics* (John Wiley & Sons, 1998).

[87] D. Armani, T. J. Kippenberg, S. M. Spillane, and K. J. Vahala, "Ultra-High-Q Toroid Microcavity on a Chip," Nature **421**, 925–928 (2003).

[88] V. B. Braginsky, M. L. Gorodetsky, and V. S. Ilchenko, "Quality-Factor and Nonlinear Properties of Optical Whispering-Gallery Modes," Physics Letters A **137**, 394–397 (1989).

[89] M. Borselli, T. Johnson, and O. Painter, "Beyond the Rayleigh Scattering Limit in High-Q Silicon Microdisks: Theory and Experiment," Optics Express **13**, 1515–1530 (2005).

[90] G. C. Righini, Y. Dumeige, P. Féron, M. Ferrari, G. N. Conti, D. Ristic, and S. Soria, "Whispering Gallery Mode Microresonators: Fundamentals and Applications," Rivista del Nuovo Cimento **34**, 435–488 (2011).

[91] A. Dupuis, N. Guo, B. Gauvreau, A. Hassani, E. Pone, F. Boismenu, and M. Skorobogatiy, "Guiding in the Visible with "Colorful" Solid-Core Bragg Fibers," Optics Letters **32**, 2882–2884 (2008).

[92] S. L. McCall, A. F. J. Levi, R. E. Slusher, S. J. Pearton, and R. A. Logan, "Whispering-Gallery Mode Microdisk Lasers," Applied Physics Letters **60**, 289–291 (1992).

[93] B. R. Johnson, "Theory of Morphology-Dependent Resonances – Shape Resonances and Width Formulas," Journal of the Optical Society of America A **10**, 343–352 (1993).

[94] H.-J. Moon, "Photon Tunneling Behavior in a Coated Cylindrical Microcavity Laser," Journal of the Optical Society of America B **27**, 512–517 (2010).

[95] D. Floess, "Numerische Analyse optischer Flüstergalerieresonatoren zur Biodetektion," Diploma Thesis, Karlsruhe Institute of Technology (KIT) (2011).

[96] M. Borselli, K. Srinivasan, P. E. Barclay, and O. Painter, "Rayleigh Scattering, Mode Coupling, and Optical Loss in Silicon Microdisks," Applied Physics Letters **85**, 3693–3695 (2004).

[97] T. J. Kippenberg, S. M. Spillane, and K. J. Vahala, "Demonstration of Ultra-High-Q Small Mode Volume Toroid Microcavities on a Chip," Applied Physics Letters **85**, 6113–6115 (2004).

[98] P. Michler, A. Kiraz, C. Becher, W. V. Schoenfeld, P. M. Petroff, L. Zhang, E. Hu, and A. Imamoglu, "A Quantum Dot Single-Photon Turnstile Device," Science **290**, 2282–2285 (2000).

[99] K. Djordjev, S.-J. Choi, S.-J. Choi, and P. D. Dapkus, "Microdisk Tunable Resonant Filters and Switches," IEEE Photonics Technology Letters **14**, 828–830 (2002).

[100] V. R. Almeida, C. A. Barrios, R. R. Panepucci, and M. Lipson, "All-Optical Control of Light on a Silicon Chip," Nature **431**, 1081–1084 (2004).

[101] P. Del'Haye, A. Schliesser, O. Arcizet, T. Wilken, R. Holzwarth, and T. J. Kippenberg, "Optical Frequency Comb Generation from a Monolithic Microresonator," Nature **450**, 1214–1217 (2007).

[102] S. M. Spillane, T. J. Kippenberg, K. J. Vahala, K. W. Goh, E. Wilcut, and H. J. Kimble, "Ultrahigh-Q Toroidal Microresonators for Cavity Quantum Electrodynamics," Physical Review A **71**, 013817 (2005).

[103] L. Rayleigh, "The Problem of the Whispering Gallery," Philosophical Magazine Series 6 **20**, 1001–1004 (1910).

[104] D. W. Vernooy, V. S. Ilchenko, H. Mabuchi, E. W. Streed, and H. J. Kimble, "High-Q Measurements of Fused-Silica Microspheres in the Near Infrared," Optics Letters **23**, 247–249 (1998).

[105] A. Schweinsberg, S. Hocdé, N. N. Lepeshkin, R. W. Boyd, C. Chase, and J. E. Fajardo, "An Environmental Sensor Based on an Integrated Optical Whispering Gallery Mode Disk Resonator," Sensors and Actuators B: Chemical **123**, 727–732 (2007).

[106] L. He, Ş. K. Özdemir, J. Zhu, W. Kim, and L. Yang, "Detecting Single Viruses and Nanoparticles Using Whispering Gallery Microlasers," Nature Nanotechnology **6**, 428–432 (2011).

[107] T. Grossmann, M. Hauser, T. Beck, C. Gohn-Kreuz, M. Karl, H. Kalt, C. Vannahme, and T. Mappes, "High-Q Conical Polymeric Microcavities," Applied Physics Letters **96**, 013303 (2010).

[108] A. Yariv, *Optical Electronics* (Saunders College Publications, 1991).

[109] M. Hauser, "Mikroresonatoren aus Glas und Polymeren als optische Flüstergalerien," Ph.D. Thesis, Karlsruhe Institute of Technology (KIT) (2011).

[110] M. L. Gorodetsky, A. A. Savchenkov, and V. S. Ilchenko, "Ultimate Q of Optical Microsphere Resonators," Optics Letters **21**, 453–455 (1996).

[111] W. Bogaerts, P. de Heyn, T. van Vaerenbergh, K. de Vos, S. Kumar Selvaraja, T. Claes, P. Dumon, P. Bienstman, D. van Thourhout, and R. Baets, "Silicon Microring Resonators," Laser and Photonics Reviews **6**, 47–73 (2012).

[112] K. Okamoto, *Fundamentals of Optical Waveguides* (Elsevier Academic Press, 2006).

[113] M. G. Kuzyk, *Polymer Fiber Optics* (CRC Press, Taylor & Francis Group, 2007).

[114] S. Sujecki, *Photonics Modelling and Design* (CRC Press, Taylor & Francis Group, 2015).

[115] J. Niehusmann, A. Vörckel, P. H. Bolivar, T. Wahlbrink, and W. Henschel, "Microring Resonator," Optics Letters **29**, 2861–2863 (2004).

[116] S. Hu, Y. Zhao, K. Qin, S. T. Retterer, I. I. Kravchenko, and S. M. Weiss, "Enhancing the Sensitivity of Label-Free Silicon Photonic Through Increased Probe Molecule Density," ACS Photonics **1**, 590–597 (2014).

[117] F. P. Schäfer, ed., *Dye Lasers* (Springer, 1990).

[118] J. R. Lakowicz, *Principles of Fluorescence Spectroscopy* (Springer, 2006).

[119] O. Svelto, *Principles of Lasers* (Springer, 2010).

[120] J. T. Verdeyen, *Laser Electronics* (Prentice-Hall International, 1995).

[121] M. M. Mazumder, G. Chen, R. K. Chang, and J. B. Gillespie, "Wavelength Shifts of Dye Lasing in Microdroplets: Effect of Absorption Change," Optics Letters **20**, 878–880 (1995).

[122] S. Singh, R. G. Smith, and L. G. Van Uitert, "Stimulated-Emission Cross Section and Fluorescent Quantum Efficiency of Nd^{3+} in Yttrium Aluminum Garnet at Room Temperature," Physical Review B **10**, 2566–2572 (1974).

[123] J. Koetke and G. Huber, "Infrared Excited-State Absorption and Stimulated-Emission Cross Sections of Er^{3+}-Doped Crystals," Applied Physics B **61**, 151–158 (1995).

[124] H.-J. Moon, Y.-T. Chough, J. B. Kim, K. An, J. Yi, and J. Lee, "Cavity-Q-Driven Spectral Shift in a Cylindrical Whispering-Gallery-Mode Microcavity Laser," Applied Physics Letters **76**, 3679–3681 (2000).

[125] F. López Arbeloa, P. Ruiz Ojeda, and I. López Arbeloa, "The Fluorescence Quenching Mechanisms of Rhodamine 6G in Concentrated Ethanolic Solution," Journal of Photochemistry and Photobiology, A: Chemistry **45**, 313–323 (1988).

[126] A. Diaspro, ed., *Nanoscopy and Multidimensional Optical Fluorescence Microscopy* (CRC Press, Taylor & Francis Group, 2010).

[127] C. Grivas and M. Pollnau, "Organic Solid-State Integrated Amplifiers and Lasers," Laser and Photonics Reviews **6**, 419–462 (2012).

[128] L. Cerdán, A. Costela, I. Garça-Moreno, O. García, and R. Sastre, "Waveguides and Quasi-Waveguides Based on Pyrromethene 597-Doped Poly(methyl methacrylate)," Applied Physics B **97**, 73–83 (2009).

[129] T. Susdorf, A. Tyagi, D. del Agua, A. Penzkofer, O. García, R. Sastre, A. Costela, and I. García-Moreno, "Photophysical Characterization of Pyrromethene 597 Laser Dye in Cross-Linked Silicon-Containing Organic Copolymers," Chemical Physics **342**, 201–214 (2007).

[130] A. Costela, I. García-Moreno, and R. Sastre, "Polymeric Solid-State Dye Lasers: Recent Developments," Physical Chemistry Chemical Physics **5**, 4745 (2003).

[131] J. B. Prieto, F. L. Arbeloa, V. M. Martínez, T. A. López, and I. L. Arbeloa, "Photophysical Properties of the Pyrromethene 597 Dye: Solvent Effect," Journal of Physical Chemistry A **108**, 5503–5508 (2004).

[132] S. Krämmer, C. Vannahme, C. L. C. Smith, T. Grossmann, M. Jenne, S. Schierle, L. Jørgensen, I. S. Chronakis, A. Kristensen, and H. Kalt, "Random-Cavity Lasing from Electrospun Polymer Fiber Networks," Advanced Materials **26**, 8096–8100 (2014).

[133] G. Brambilla, F. Xu, and X. Feng, "Fabrication of Optical Fibre Nanowires and their Optical and Mechanical Characterisation," Electronics Letters **42**, 517–518 (2006).

[134] T. Beck, "Polymer-Mikroresonatoren hoher Güte als optische Sensoren," Ph.D. Thesis, Karlsruhe Institute of Technology (KIT) (2013).

[135] S. Arnold, M. Khoshsima, I. Teraoka, S. Holler, and F. Vollmer, "Shift of Whispering-Gallery Modes in Microspheres by Protein Adsorption," Optics Letters **28**, 272–274 (2003).

[136] H. Zhu, I. M. White, J. D. Suter, P. S. Dale, and X. Fan, "Analysis of Biomolecule Detection with Optofluidic Ring Resonator Sensors," Optics Express **15**, 9139–9146 (2007).

[137] R. W. Boyd and J. E. Heebner, "Sensitive Disk Resonator Photonic Biosensor," Applied Optics **40**, 5742–5747 (2001).

[138] W. Lee, Y. Sun, H. Li, K. Reddy, M. Sumetsky, and X. Fan, "A Quasi-Droplet Optofluidic Ring Resonator Laser Using a Micro-Bubble," Applied Physics Letters **99**, 1–4 (2011).

[139] V. R. Dantham, S. Holler, V. Kolchenko, Z. Wan, and S. Arnold, "Taking Whispering Gallery-Mode Single Virus Detection and Sizing to the Limit," Applied Physics Letters **101**, 043704 (2012).

[140] J. Park, Ş. K. Özdemir, F. Monifi, T. Chadha, S. H. Huang, P. Biswas, and L. Yang, "Titanium Dioxide Whispering Gallery Microcavities," Advanced Optical Materials **2**, 711–717 (2014).

[141] X. Lu, J. Y. Lee, P. X. Feng, and Q. Lin, "High Q Silicon Carbide Microdisk Resonator," Applied Physics Letters **104**, 181103 (2014).

[142] M. A. Foster, J. S. Levy, O. Kuzucu, S. Kasturi, M. Lipson, and A. L. Gaeta, "Silicon-Based Monolithic Optical Frequency Comb Source," Optics Express **19**, 14233–14239 (2011).

[143] R. Madugani, Y. Yang, J. M. Ward, J. D. Riordan, S. Coppola, V. Vespini, S. Grilli, A. Finizio, P. Ferraro, and S. Nic Chormaic, "Terahertz Tuning of Whispering Gallery Modes in a PDMS Stand-Alone, Stretchable Microsphere," Optics Letters **37**, 4762–4764 (2012).

[144] R. Zeltner, F. Sedlmeir, G. Leuchs, and H. G. L. Schwefel, "Crystalline MgF_2 Whispering Gallery Mode Resonators for Enhanced Bulk Index Sensitivity," European Physical Journal: Special Topics **223**, 1989–1994 (2014).

[145] R. W. P. Drever, J. L. Hall, F. V. Kowalski, J. Hough, G. M. Ford, A. J. Munley, and H. Ward, "Laser Phase and Frequency Stabilization Using an Optical Resonator," Applied Physics B **31**, 97–105 (1983).

[146] E. D. Black, "An Introduction to Pound–Drever–Hall Laser Frequency Stabilization," American Journal of Physics **69**, 79–87 (2001).

[147] J. D. Swaim, J. Knittel, and W. P. Bowen, "Detection of Nanoparticles with a Frequency Locked Whispering Gallery Mode Microresonator," Applied Physics Letters **102**, 183106 (2013).

[148] J. Su, "Label-Free Single Exosome Detection Using Frequency-Locked Microtoroid Optical Resonators," ACS Photonics **2**, 1241–1245 (2015).

[149] D. S. Weiss, V. Sandoghdar, J. Hare, V. Lefèvre-Seguin, J. M. Raimond, and S. Haroche, "Splitting of High-Q Mie Modes Induced by Light Backscattering in Silica Microspheres," Optics Letters **20**, 1835–1837 (1995).

[150] S. Arnold, R. Ramjit, D. Keng, V. Kolchenko, and I. Teraoka, "MicroParticle Photophysics Illuminates Viral Bio-Sensing," Faraday Discussions **137**, 65–83 (2008).

[151] J. Zhu, Ş. K. Özdemir, Y.-F. Xiao, L. Li, L. He, D.-R. Chen, and L. Yang, "On-chip Single Nanoparticle Detection and Sizing by Mode Splitting in an Ultrahigh-Q Microresonator," Nature Photonics **4**, 46–50 (2010).

[152] L. Shao, X. F. Jiang, X. C. Yu, B. B. Li, W. R. Clements, F. Vollmer, W. Wang, Y. F. Xiao, and Q. Gong, "Detection of Single Nanoparticles and Lentiviruses Using Microcavity Resonance Broadening," Advanced Materials **25**, 5616–5620 (2013).

[153] L. He, Ş. K. Özdemir, J. Zhu, and L. Yang, "Ultrasensitive Detection of Mode Splitting in Active Optical Microcavities," Physical Review A **82**, 1–4 (2010).

[154] S. I. Shopova, C. W. Blackledge, and A. T. Rosenberger, "Enhanced Evanescent Coupling to Whispering-Gallery Modes Due to Gold Nanorods Grown on the Microresonator Surface," Applied Physics B **93**, 183–187 (2008).

[155] S. I. Shopova, R. Rajmangal, S. Holler, and S. Arnold, "Plasmonic Enhancement of a Whispering-Gallery-Mode Biosensor for Single Nanoparticle Detection," Applied Physics Letters **98**, 243104 (2011).

[156] M. D. Baaske, M. R. Foreman, and F. Vollmer, "Single-Molecule Nucleic Acid Interactions Monitored on a Label-Free Microcavity Biosensor Platform," Nature Nanotechnology **9**, 933–939 (2014).

[157] T. Siegle, "Optische Moden in aktiven Flüstergalerie-Mikroresonatoren," Diploma Thesis, Karlsruhe Institute of Technology (KIT) (2014).

[158] A. L. Martin, D. K. Armani, L. Yang, and K. J. Vahala, "Replica-Molded High-Q Polymer Microresonators," Optics Letters **29**, 533–535 (2004).

[159] M. Lambropoulos, "Fluorol 7GA: An Efficient Yellow-Green Dye for Flashlamp-Pumped Lasers," Optics Communications **15**, 35–37 (1975).

[160] M. L. Lesiecki and J. M. Drake, "Use of the Thermal Lens Technique to Measure the Luminescent Quantum Yields of Dyes in PMMA for Luminescent Solar Concentrators," Applied Optics **21**, 557–560 (1982).

[161] T. G. Pavlopoulos and D. J. Golich, "Triplet Extinction Coefficients of Some Laser Dyes I," Journal of Applied Physics **64**, 521–527 (1988).

[162] J. Fischer, "Polymere Flüstergalerielaser für die Biosensorik," Diploma Thesis, Karlsruhe Institute of Technology (KIT) (2013).

[163] R. Schmager, "Lasing Threshold of Fluorol Doped Microgoblets," Bachelor's Thesis, Karlsruhe Institute of Technology (KIT) (2013).

[164] F. Ruf, "TiO_2 Coated Whispering-Gallery-Mode Resonators for Sensing: Simulations and Experiments," Master's Thesis, Karlsruhe Institute of Technology (KIT) (2015).

[165] T. Wienhold, "Integrated Dye Lasers for All-Polymer Photonic Lab-on-a-Chip Systems," Ph.D. Thesis, Karlsruhe Institute of Technology (KIT) (2016).

[166] T. Wienhold, S. Kraemmer, A. Bacher, H. Kalt, C. Koos, S. Koeber, and T. Mappes, "Efficient Free-Space Read-Out of WGM Lasers Using Circular Micromirrors," Optics Express **23**, 11451–11456 (2015).

[167] M. Hippler, "Exosome Detecion with Referenced Whispering-gallery Mode Lasers," Master's Thesis, Karlsruhe Institute of Technology (KIT) (2016).

[168] S. S. Rastjoo, "Sensitivity Enhancement of Polymeric Whispering-Gallery Microsensors," Master's Thesis, Karlsruhe Institute of Technology (KIT) (2016).

[169] S. Krämmer, S. Rastjoo, T. Siegle, S. F. Wondimu, C. Klusmann, and H. Kalt, "Size-Optimized Polymeric Whispering Gallery Mode Lasers with Enhanced Sensing Performance," *manuscript in preparation* .

[170] A. L. Schawlow and C. H. Townes, "Infrared and Optical Masers," Physical Review **112**, 1940–1949 (1958).

[171] L. Yang, T. Lu, T. Carmon, B. Min, and K. J. Vahala, "A 4-Hz Fundamental Linewidth On-Chip Microlaser," in "Conference on Quantum Electronics and Laser Science Conference on Lasers and Electro-Optics, CLEO/QELS, San Jose, USA," (2007).

[172] M. Bayer, T. Gutbrod, J. Reithmaier, A. Forchel, T. Reinecke, P. Knipp, A. Dremin, and V. Kulakovskii, "Optical Modes in Photonic Molecules," Physical Review Letters **81**, 2582–2585 (1998).

[173] Y. P. Rakovich, J. F. Donegan, M. Gerlach, A. L. Bradley, T. M. Connolly, J. J. Boland, N. Gaponik, and A. Rogach, "Fine Structure of Coupled Optical Modes in Photonic Molecules," Physical Review A **70**, 051801 (2004).

[174] S. V. Boriskina, "Spectrally Engineered Photonic Molecules as Optical Sensors with Enhanced Sensitivity: A Proposal and Numerical Analysis," Journal of the Optical Society of America B **23**, 1565–1573 (2006).

[175] O. Gaathon, J. Culic-Viskota, M. Mihnev, I. Teraoka, and S. Arnold, "Enhancing the Sensitivity Limit of the Whispering Gallery Mode Biosensor Through Sub-Wavelength Confinement of Light," Conference on Quantum Electronics and Laser Science Conference on Lasers and Electro-Optics, CLEO/QELS, San Jose, USA (2007).

[176] U. Bog, "Optische Flüstergaleriemoden-Resonatoren für die Biosensorik," Ph.D. Thesis, Karlsruhe Institute of Technology (KIT) (2015).

[177] J. Pomplun, S. Burger, L. Zschiedrich, and F. Schmidt, "Adaptive Finite Element Method for Simulation of Optical Nano Structures," Physica Status Solidi B **244**, 3419–3434 (2007).

[178] M. Oxborrow, "Traceable 2-D Finite-Element Simulation of the Whispering-Gallery Modes of Axisymmetric Electromagnetic Resonators," IEEE Transactions on Microwave Theory and Techniques **55**, 1209–1218 (2007).

[179] G. Gülsen and M. Naci Inci, "Thermal Optical Properties of TiO_2 Films," Optical Materials **18**, 373–381 (2002).

[180] R. G. Heideman and P. V. Lambeck, "Remote Opto-Chemical Sensing with Extreme Sensitivity: Design, Fabrication and Performance of a Pigtailed Integrated Optical Phase-Modulated Mach–Zehnder Interferometer System," Sensors and Actuators B: Chemical **61**, 100–127 (1999).

[181] D. Solimini, "Loss Measurement of Organic Materials at 6328 Å," Journal of Applied Physics **37**, 3314–3315 (1966).

[182] R. M. Waxler, D. Horowitz, and A. Feldman, "Optical and Physical Parameters of Plexiglas 55 and Lexan," Applied Optics **18**, 101–104 (1979).

[183] S. M. Spillane, T. J. Kippenberg, O. J. Painter, and K. J. Vahala, "Ideality in a Fiber-Taper-Coupled Microresonator System for Application," Physical Review Letters **91**, 043902 (2003).

[184] T. Grossmann, T. Wienhold, U. Bog, T. Beck, C. Friedmann, H. Kalt, and T. Mappes, "Polymeric Photonic Molecule Super-Mode Lasers on Silicon," Light: Science & Applications **2**, e82 (2013).

[185] S. Schierle, "Ursprung der Laseremission in Farbstoff dotierten Polymerfasern," Bachelor's Thesis, Karlsruhe Institute of Technology (KIT) (2013).

[186] A. Frenot and I. S. Chronakis, "Polymer Nanofibers Assembled by Electrospinning," Current Opinion in Colloid and Interface Science **8**, 64–75 (2003).

[187] D. Li and Y. Xia, "Electrospinning of Nanofibers: Reinventing the Wheel?" Advanced Materials **16**, 1151–1170 (2004).

[188] N. Bhardwaj and S. C. Kundu, "Electrospinning: A Fascinating Fiber Fabrication Technique," Biotechnology Advances **28**, 325–347 (2010).

[189] J. M. Moran-Mirabal, J. D. Slinker, J. A. DeFranco, S. S. Verbridge, R. Ilic, S. Flores-Torres, H. Abruña, G. G. Malliaras, and H. G. Craighead, "Electrospun Light-Emitting Nanofibers," Nano Letters **7**, 458–463 (2007).

[190] H. Yu, H. Song, G. Pan, L. Fan, S. Li, X. Bai, S. Lu, and H. Zhao, "Preparation and Luminescent Properties of Polymer Fibers Containing Y_2O_3:Eu Nanoparticles by Electrospinning," Journal of Nanoscience and Nanotechnology **8**, 6017–6022 (2008).

[191] A. Camposeo, F. Di Benedetto, R. Stabile, A. R. Neves, R. Cingolani, and D. Pisignano, "Laser Emission from Electrospun Polymer Nanofibers," Small **5**, 562–566 (2009).

[192] D. Di Camillo, V. Fasano, F. Ruggieri, S. Santucci, L. Lozzi, A. Camposeo, and D. Pisignano, "Near-Field Electrospinning of Light-Emitting Conjugated Polymer Nanofibers," Nanoscale **5**, 11637–11642 (2013).

[193] D. H. Reneker, A. L. Yarin, H. Fong, and S. Koombhongse, "Bending Instability of Electrically Charged Liquid Jets of Polymer Solutions in Electrospinning," Journal of Applied Physics **87**, 4531–4547 (2000).

[194] M. M. Hohman, M. Shin, G. Rutledge, and M. P. Brenner, "Electrospinning and Electrically Forced Jets. I. Stability Theory," Physics of Fluids **13**, 2221–2236 (2001).

[195] C. P. Carroll and Y. L. Joo, "Electrospinning of Viscoelastic Boger Fluids: Modeling and Experiments," Physics of Fluids **18** (2006).

[196] Z. Sun, E. Zussman, A. L. Yarin, J. H. Wendorff, and A. Greiner, "Compound Core-Shell Polymer Nanofibers by Co-Electrospinning," Advanced Materials **15**, 1929–1932 (2003).

[197] D. Li and Y. Xia, "Direct Fabrication of Composite and Ceramic Hollow Nanofibers by Electrospinning," Nano Letters **4**, 933–938 (2004).

[198] I. G. Loscertales, A. Barrero, M. Márquez, R. Spretz, R. Velarde-Ortiz, and G. Larsen, "Electrically Forced Coaxial Nanojets for One-Step Hollow Nanofiber Design," Journal of the American Chemical Society **126**, 5376–5377 (2004).

[199] J. Lahann, "Recent Progress in Nano-Biotechnology: Compartmentalized Micro- and Nanoparticles via Electrohydrodynamic Co-Jetting," Small **7**, 1149–1156 (2011).

[200] M. Bogntizki, T. Frese, M. Steinhart, A. Greiner, J. H. Wendorff, A. Schaper, and M. Hellwig, "Preparation of Fibers with Nanoscaled Morphologies – Electrospinning of Polymer Blends," Polymer Engineering and Science **41**, 982–989 (2001).

[201] D. Li, Y. Wang, and Y. Xia, "Electrospinning of Polymeric and Ceramic Nanofibers as Uniaxially Aligned Arrays," Nano Letters **3**, 1167–1171 (2003).

[202] S. Pagliara, A. Camposeo, A. Polini, R. Cingolani, and D. Pisignano, "Electrospun Light-Emitting Nanofibers as Excitation Source in Microfluidic Devices," Lab on a Chip **9**, 2851–2856 (2009).

[203] L. Persano, A. Camposeo, C. Tekmen, and D. Pisignano, "Industrial Upscaling of Electrospinning and Applications of Polymer Nanofibers: A Review," Macromolecular Materials and Engineering **298**, 504–520 (2013).

[204] X. Wang, K. Zhang, M. Zhu, H. Yu, Z. Zhou, Y. Chen, and B. S. Hsiao, "Continuous Polymer Nanofiber Yarns Prepared by Self-Bundling Electrospinning Method," Polymer **49**, 2755–2761 (2008).

[205] J. Stitzel, J. Liu, S. J. Lee, M. Komura, J. Berry, S. Soker, G. Lim, M. Van Dyke, R. Czerw, J. J. Yoo, and A. Atala, "Controlled Fabrication of a Biological Vascular Substitute," Biomaterials **27**, 1088–1094 (2006).

[206] D. Sun, C. Chang, S. Li, and L. Lin, "Near-Field Electrospinning," Nano Letters **6**, 839–842 (2006).

[207] C. Chang, K. Limkrailassiri, and L. Lin, "Continuous Near-Field Electrospinning for Large Area Deposition of Orderly Nanofiber Patterns," Applied Physics Letters **93**, 2–5 (2008).

[208] I. D. W. Samuel, E. B. Namdas, and G. A. Turnbull, "How to Recognize Lasing," Nature Photonics **3**, 546–549 (2009).

[209] M. Lietz, "Urpsrung der Laseremission in farbstoffdotierten Polymerfasern: Zufallsresonatoren oder Zufallslaser?" Bachelor's Thesis, Karlsruhe Institute of Technology (KIT) (2014).

[210] L. Tong, J. Lou, R. R. Gattass, S. He, X. Chen, L. Liu, and E. Mazur, "Assembly of Silica Nanowires on Silica Aerogels for Microphotonic Devices," Nano Letters **5**, 259–262 (2005).

[211] A. Ghatak and K. Thyagarajan, *Introduction to Fiber Optics* (Cambridge University Press, 1998).

[212] R. Dersch, M. Steinhart, U. Boudriot, A. Greiner, and J. H. Wendorff, "Nanoprocessing of Polymers: Applications in Medicine, Sensors, Catalysis, Photonics," Polymers for Advanced Technologies **16**, 276–282 (2005).

[213] S. Agarwal, J. H. Wendorff, and A. Greiner, "Progress in the Field of Electrospinning for Tissue Engineering Applications," Advanced Materials **21**, 3343–3351 (2009).

[214] E.-R. Kenawy, G. L. Bowlin, K. Mansfield, J. Layman, G. Simpson, E. H. Sanders, and G. E. Wnek, "Release of Tetracycline Hydrochloride from Electrospun Poly(ethylene-co-vinylacetate), Poly(lactic acid), and a Blend," Journal of Controlled Release **81**, 57–64 (2002).

[215] P. Anzenbacher, F. Li, and M. A. Palacios, "Toward Wearable Sensors: Fluorescent Attoreactor Mats as Optically Encoded Cross-Reactive Sensor Arrays," Angewandte Chemie – International Edition **51**, 2345–2348 (2012).

[216] Y. Long, H. Chen, Y. Yang, H. Wang, Y. Yang, N. Li, K. Li, J. Pei, and F. Liu, "Electrospun Nanofibrous Film Doped with a Conjugated Polymer for DNT Fluorescence Sensor," Macromolecules **42**, 6501–6509 (2009).

[217] C. Zhou, Y. Shi, X. Ding, M. Li, J. Luo, Z. Lu, and D. Xiao, "Development of a Fast and Sensitive Glucose Biosensor Using Iridium Complex-Doped Electrospun Optical Fibrous Membrane," Analytical Chemistry **85**, 1171–1176 (2013).

[218] B. W. Davis, N. Niamnont, C. D. Hare, M. Sukwattanasinitt, and Q. Cheng, "Nanofibers Doped with Dendritic Fluorophores for Protein Detection," ACS Applied Materials and Interfaces **2**, 1798–1803 (2010).

[219] J. N. Lee, C. Park, and G. M. Whitesides, "Solvent Compatibility of Poly(dimethylsiloxane)-Based Microfluidic Devices," Analytical Chemistry **75**, 6544–6554 (2003).

[220] R. St-Gelais, G. MacKey, J. Saunders, J. Zhou, A. Leblanc-Hotte, A. Poulin, J. A. Barnes, H. P. Loock, R. S. Brown, and Y. A. Peter, "Gas Sensing Using Polymer-Functionalized Deformable Fabry-Perot Interferometers," Sensors and Actuators B: Chemical **182**, 45–52 (2013).

[221] C. L. C. Smith, J. U. Lind, C. H. Nielsen, M. B. Christiansen, T. Buss, N. B. Larsen, and A. Kristensen, "Enhanced Transduction of Photonic Crystal Dye Lasers for Gas Sensing via Swelling Polymer Film," Optics Letters **36**, 1392–1394 (2011).

[222] B. A. Convertino, A. Capobianchi, A. Valentini, and E. N. M. Cirillo, "A New Approach to Organic Solvent Detection: High-Reflectivity Bragg Reflectors Based on a Gold Nanoparticle/Teflon-like Composite Material," Advanced Materials **15**, 1103–1105 (2003).

[223] G. Gauglitz, A. Brecht, G. Kraus, and W. Nahm, "Chemical and Biochemical Sensors Based on Interferometry at Thin (Multi-)Layers," Sensors and Actuators B: Chemical **11**, 21–27 (1993).

[224] Y. Kang, J. J. Walish, T. Gorishnyy, and E. L. Thomas, "Broad-Wavelength-Range Chemically Tunable Block-Copolymer Photonic Gels," Nature Materials **6**, 957–960 (2007).

[225] K. Reddy, Y. Guo, J. Liu, W. Lee, M. K. K. Oo, and X. Fan, "Rapid, Sensitive, and Multiplexed On-Chip Optical Sensors for Micro-Gas Chromatography," Lab on a Chip **12**, 901–905 (2012).

[226] N. M. Tran, "Electrospun Polymer Fiber Networks for Sensing Applications," Master's Thesis, Karlsruhe Institute of Technology (KIT) (2014).

[227] P. Kiefer, "Dye Doped Polymer Fibers as Ethanol Sensors," Bachelor's Thesis, Karlsruhe Institute of Technology (KIT) (2015).

[228] S. Krämmer, F. Laye, F. Friedrich, C. Vannahme, C. L. C. Smith, A. C. Mendes, I. S. Chronakis, K. Anders, and H. Kalt, "Electrospun Polymer Fiber Lasers for Applications in Vapor Sensing," *manuscript in preparation* .

[229] F. Friedrich, "Optical Sensing of Light Alcohols with Electrospun Polymer Fiber Networks," Bachelor's Thesis, Karlsruhe Institute of Technology (KIT) (2016).

[230] W. R. Vieth, *Diffusion in and Through Polymers: Principles and Applications* (Hanser, 1991).

[231] N. L. Thomas and A. H. Windle, "A Theory of Case II Diffusion," Polymer **23**, 529–542 (1981).

[232] T. T. Wang and T. K. Kwei, "Diffusion in Glassy Polymers. Reexamination of Vapor Sorption Data," Macromolecules **6**, 919–921 (1973).

[233] J. S. Papanu, D. W. Hess, D. S. Soane (Soong), and A. T. Bell, "Swelling of Poly(methyl methacrylate) Thin Films in Low Molecular Weight Alcohols," Journal of Applied Polymer Science **39**, 803–823 (1990).

[234] A. Sfirakis and C. E. Rogers, "Sorption and Diffusion of Alcohols in Amorphous Polymers," Polymer Engineering and Science **21**, 542–547 (1981).

[235] H. B. Hopfenberg, "The Effect of Thin Film Thickness and Sample History on the Parameters Describing Transport in Glassy Polymers," Journal of Membrane Science **3**, 215–230 (1978).

[236] A. Peterlin, "Diffusion in a Network with Discontinous Swelling," Polymer Letters **3**, 1083–1087 (1965).

[237] Z. Zhang, P. Zhao, P. Lin, and F. Sun, "Thermo-Optic Coefficients of Polymers for Optical Waveguide Applications," Polymer **47**, 4893–4896 (2006).

[238] H. S. Choi, A. M. Armani, H. S. Choi, and A. M. Armani, "Thermal Nonlinear Effects in Hybrid Optical Microresonators," Applied Physics Letters **97**, 223306 (2010).

[239] G. Gupta, W. H. Steier, Y. Liao, J. Luo, L. R. Dalton, and A. K. Jen, "Modeling Photobleaching of Optical Chromophores: Light-Intensity Effects in Precise Trimming of Integrated Polymer Devices," Journal of Physical Chemistry C **112**, 8051–8060 (2008).

[240] M. Ahmad, T. A. King, D. K. Ko, B. Heon Cha, and J. Lee, "Photostability of Lasers Based on Pyrromethene 567 in Liquid and Solid-State Host Media," Optics Communications **203**, 327–334 (2002).

[241] A. Matthes, "Zur Theorie des Quellvorgangs an Gelen," Kolloid Zeitschrift **108**, 79–94 (1944).

[242] W. Zeng, Y. Du, Y. Xue, and H. L. Frisch, *Physical Properties of Polymers Handbook* (Springer, 2007), chap. Solubility Parameters, pp. 289–303.

[243] G. I. Sarser and N. G. Kalinin, "Diffusion of Liquid Media in Stressed and Unstressed PMMA," Soviet Materials Science **9**, 610–611 (1975).

[244] J. Kuhn, J. M. Castillo Sanchez, J. Gascon, S. Calero, D. Dubbeldam, T. J. H. Vlugt, F. Kapteijn, and J. Gross, "Adsorption and Diffusion of Water, Methanol and Ethanol in All-Silica DD3R: Experiments and Simulations," The Journal of Physical Chemistry C **114**, 6877–6878 (2010).

[245] M. Göhring, "Sensitivity of Dye-Doped Polymer Fiber Networks," Bachelor's Thesis, Karlsruhe Institute of Technology (KIT) (2016).

[246] U. Bog, T. Laue, T. Grossmann, T. Beck, T. Wienhold, B. Richter, M. Hirtz, H. Fuchs, H. Kalt, and T. Mappes, "On-Chip Microlasers for Biomolecular Detection via Highly Localized Deposition of a Multifunctional Phospholipid Ink," Lab on a Chip **13**, 2701–2707 (2013).

Closing Words

Finally, I would like to thank all the people who have supported me in the pursuit of this work:

- Prof. Dr. Heinz Kalt for giving me the opportunity to work on this exciting research project and for giving me the freedom to realize my own ideas. Furthermore, for having an open door throughout the whole time and his support concerning participation in conferences.
- Priv.-Doz. Dr.-Ing. Timo Mappes for agreeing to act as co-examiner, his interest in my work and for the insights into research outside university.
- My friend and colleague Tobias Siegle for inspiring discussions about all kind of possible projects and the successful teamwork during the whole time. It was a great pleasure to work with you!
- My friends and colleagues Tobias Siegle, Mario Lang and Andreas Merz for their helpfulness on technical problems, the enjoyable atmosphere, the discussions about all kind of physical questions (also apart from optics) and the great time in general!
- My WGM-office colleagues Carolin Klusmann and Tobias Siegle for the friendly atmosphere and the fruitful conversations on WGM cavities.
- My diploma, master and bachelor students Tobias Siegle, Carolin Klusmann, Fabian Ruf, Minh Tran, Sanaz Rastjoo, Stefan Schierle, Raphael Schmager, Martin Lietz, Pascal Kiefer, Felix Friedrich, Max Göhring and Julian Skolaut for their active participation in the research on dye-doped polymeric mircolasers and the shared time in the lab. You essentially contributed to this research project and helped a lot to promote it.
- All members of our workgroup for the friendly and cheerful atmosphere and the great time also outside university.

- Dr. Tobias Wienhold and Sentayehu Wondimu for the successful collaboration, the fruitful discussions, the support with samples, and the throughout friendly atmosphere. I enjoyed working with you!
- Dr. Uwe Bog for his cooperativeness and the insights into all kind of functionalization techniques.
- Silvia Diewald and Stefan Kühn for the throughout fast sample preparation via e-beam lithography, the discussions on photoresists and the advice on obtaining good SEM images.
- Patrice Brenner for the preparation of the FIB cuts.
- Fabrice Laye for fruitful the discussions about polymer fiber networks, the nice collaboration and for the conduction of the ellipsometry measurements.
- Dr. Christoph Vannahme and Dr. Cameron L. C. Smith for their continuous support of the project on the electrospun polymer fiber networks and their interest in my work.
- Dr. Lars Jørgensen, Dr. Ana C. Mendes and Prof. Dr. I. S. Chronakis for the fabrication of the dye-doped polymer fiber networks.
- Kristian Sørensen and Dr. Christoph Vannahme for the deposition of the TiO_2 coating layer.
- The electronics and mechanics workshop for their competent support and the fast realization of every kind of special lab equipment.
- Heinz Leonhard for the technical drawings.
- Our secretaries Ursula Mösle, Claudia Alaya, Monika Brenkmann and Renate Helfen for help and support in all kinds of administrative concerns.
- The Carl Zeiss Foundation, the Karlsruhe School of Optics and Photonics (KSOP) and the German Academic Exchange Service (DAAD) for financial support.
- All people who proof read this thesis and helped to eliminate errors.
- My family and my parents for their support during my whole life and for always having confidence in me. Without you this work could not have been completed.
- My husband Christoph for his faith in me, his continuous encouragement and his everlasting support and love. I love you!